THESIS

# MODELING SENSIBLE HEAT FLUX FOR VEGETATED SURFACES THROUGH AN OPTIMIZED SURFACE AERODYNAMIC TEMPERATURE APPROACH

Submitted by

Edson Costa Filho

Department of Civil and Environmental Engineering

In partial fulfillment of the requirements

For the Degree of Master of Science

Colorado State University

Fort Collins, Colorado

Summer 2019

Master's Committee:

Advisor: Jose L. Chavez

Karan Venayagamoorthy
Jay M. Ham

# ABSTRACT

## MODELING SENSIBLE HEAT FLUX FOR VEGETATED SURFACES THROUGH AN OPTIMIZED SURFACE AERODYNAMIC TEMPERATURE APPROACH

Agricultural water management advancements rely on improved methods to accurately determine crop water use. Crop evapotranspiration modeling based on the surface energy balance depends on the accurate estimation of all incoming and outgoing heat fluxes at the surface level. This thesis particularly goal is to improve sensible heat flux estimates for row crops through an optimized aerodynamic surface temperature ($T_o$) approach based on remote sensing and weather data. Empirical linear and non-linear $T_o$ models were developed based on percent cover, surface temperature, air temperature, and a new variable named turbulent mixing row resistance using data collected at the USDA-ARS Research Farm located in Greeley (CO). The experiment took place in two sub-surface drip irrigation corn fields with different irrigation water management practices in 2017-2018. Sensible heat flux were measured using LAS, eddy covariance, aerodynamic profile, and Bowen ratio methods. Remote sensing data were measured on-site using a radiometer. The fields were considered a point in space. Data from Aimes (IA) and Rocky Ford (CO) were used to assess proposed model performances under different locations and in comparison to published $T_o$ models. The results have indicated that the optimized linear $T_o$ models performed better than the non-linear and published models approaches, indicating that the introduction of percent cover and the new variable has provided reliable results under different data sets. The linear proposed $T_o$ approaches improved sensible heat flux estimation, on average, in 33 $\%$ and 28 $\%$ for the deficit and fully irrigated field at LIRF in comparison to the sensible heat based on published $T_o$ models. Sensible heat flux modeling results were better for the modeling approaches considering the empirical linear $T_o$ model than the non-linear approaches for all three data set tested.

# ACKNOWLEDGEMENTS

I would like to thank God for all the opportunities that I have to pursue a career in academia. I would like to thank my family that has been supportive in many different ways so that I may thrive academically and personally in life. Also, I want to be thankful for my academic advisor Dr. Jose Chavez for trusting me with such a important research and helping me out throughout the degree not only with meaningful feedback, but also using his professional networking to open up opportunities and advances for the project and my personal development. To all those people that helped me out during the field work campaign of 2018, as well as those that participated on the campaign of 2017, I express my sincere gratitude for their efforts in providing their time to help this project to be made true.

# DEDICATION

*I would like to dedicate this thesis to my Lord Jesus, family, and scientific community.*

TABLE OF CONTENTS

LIST OF TABLES

LIST OF FIGURES

# Chapter 1

# Introduction

Evapotranspiration (ET) represents one of the major key factors that regulate the functionality of the hydrologic cycle in the lower atmosphere (Amatya et al., 2016). Alongside precipitation, ET rates are significant to map and characterize the hydrological processes around the globe that are highly dependent on specific environmental factors that are complex to integrate in a unique and precise model.

Estimating ET accurately has a direct impact in many activities that rely on that variable as source of data to improve water management decision analysis in the irrigation and food production industry. According to Hoekstra and Chapagain (2006), the irrigation water used for the purpose of expanding crop production is about 6,390 $Gm^3$/year. That indicates irrigation as one of the major water user on a global scale.

ET estimation plays an important role on providing information for irrigation management decision because of the interconnection between the amount of water consumed by the crops and the quantitative flux of water vapor released by the plants and soil. Gowda et al. (2007) indicate that the importance of accurately estimating evapotranspiration fluxes resides on the fact that better management comes from precise data acquisition and processing, specially on areas in which the crop production is increasing by a rate that the water resources available may not be sufficient to provide the crop water requirements needed for high quality yield. The need to better estimate ET comes from the increased concern about the sustainability of the water resources. Grigg (2005) indicates that crop water use is interconnected with both evapotranspiration and plant growth. That means a more precise approach to estimate ET fluxes will provide the conditions to better allocate water for irrigation purposes and serve as input data to watershed and hydrological modeling.

Regional ET modeling has been developed as an alternative method to provide better understanding of the patterns that drive the fluxes of water into the atmosphere due to plants transpiration and soil-water evaporation. One method of acquiring data for large scale modeling is through mapping evapotranspiration using remote sensing (RS) techniques and temperature-based methods. Schmugge et al. (2002) defines remote sensing as the application of technical procedures to obtain data through measurements of emitted radiation from the land surface. Another way to describe remote sensing is by defining it as the process of acquiring data from a target without intervening on the area of interest (Schultz and Engman, 2000).

The application of remote sensing data into ET modeling is often related to the concept of energy balance budget method (EBBM), as indicated by Chavez et al. (2009). The EBBM is a method to compute latent heat flux (LE) as a residual of the difference between the available energy, given as the state of energy at the surface level that might cause for water evaporation or heating up the atmosphere, and sensible heat flux through the assessment of heat transfers that are driving the main physical processes within the atmospheric boundary layer (ABL). However, its applicability relies on the capacity of accurately estimating net radiation, surface heat and sensible heat fluxes. It is accepted that the challenges of modeling evapotranspiration through the surface energy balance budget method are due to the fact that there are uncertainties when modeling surface heat fluxes based on bulk aerodynamic and temperature gradient approaches that take into consideration the interaction between the canopy and the air flowing above it, such as sensible heat flux (H). That difficulty comes from the challenges of estimating the so called aerodynamic surface temperature ($T_o$), which is needed to estimate H, since it might not be measured on site. (Chehbouni et al., 1995; Chehbouni et al., 1996; Gowda et al., 2007).

Thus, the improvements of evapotranspiration estimation through the EBBM method are directly related to the advancements on precisely estimating H. Modeling sensible heat flux using the bulk aerodynamic resistance approach is always subject for improvement to provide better es-

timates of sensible heat flux accounting for the different conditions of the surface (homogeneous or heterogeneous surface types, dense or sparse canopy architecture) and, consequently, evapotranspiration on a regional scale analysis through remote sensing techniques. The main goal of this research is to provide an optimized model for $T_o$ that accounts for different growth stages of canopy biomass and micro-climate conditions change over time that might be incorporated into the modeling process of sensible heat flux.

# Chapter 2

# Literature Review

According to Gowda et al. (2007), the application of remote sensing techniques to provide ground surface data for ET modeling purposes has been introduced after 1970. The first publications were developed based on the use of images obtained from aircraft flights over areas of interest. The introduction of special equipment capable of measuring surface temperature from thermal spectrum only started after 1980, when satellites were providing images to acquire RS data that would served as input to the EBBM method for estimating surface heat fluxes and ET. That method is based on the simplification of the energy budget that partitions net radiation ($R_n$) into three main heat fluxes that are responsible to heat up the atmosphere (sensible heat flux or H), the soil (soil heat flux or G), and to evaporate water (latent heat flux or LE). The estimates of sensible heat flux on the EBBM method were initially proposed to be based on the gradient between the surface temperature ($T_s$) and air temperature ($T_a$). The surface temperature would be estimated from RS techniques and presented as radiometric surface temperature. However, adjustments were needed to be done since the assumption that surface temperature might be equivalent, in magnitude, to the aerodynamic temperature is not valid for most case scenarios in which heterogeneous vegetated surface conditions are predominant. Liou and Kar (2014) make an observation that simple ET models provide reasonable results when applied over areas with the same vegetation phenology, but the unstable conditions of the atmosphere and the fact that homogeneous areas occupy small areas spatially distributed on a regional scale increase the errors when simple models are applied under those conditions.

A precise EBBM to model ET using remote sensing data needs to rely on the capacity to provide accurate estimates of each component of the model. Rosenberg et al. (1983) were responsible to introduce the aerodynamic temperature as a concept to account for the temperature gradient to derive the physical process of heat transfer to the atmosphere. The definition of $T_o$ might be

given as the temperature that theoretically could be measured at a specific height in the canopy zone where the fluxes for evaporating water and heating the air become active regarding the plants characteristics (Chehbouni et al., 1996). Boulet et al. (2012) offer a more simplistic definition by claiming the aerodynamic surface temperature to be the representation of the average degree of kinetic energy that is located at the so called aerodynamic level within the canopy fully grown.

Many researchers have been arguing about the differences between the aerodynamic and radiometric surface temperature magnitudes over different scenarios. According to Chavez et al. (2005), the approximation between those two temperatures has been accepted in some studies as part of less complex models. Choudhury et al. (1986) developed a study in which there is evidence that those temperatures are reasonably the same in magnitude for scenarios when the surfaces are nearly homogeneous. In terms of radiometric temperature instead of surface temperature, Choudhury et al. (1986) indicate that the numerical fluctuations are evident when the stability or instability conditions of the lower atmospheric zone are predominant. Studies have been done to relate radiometric temperature and aerodynamic temperature to simplify the estimation of H. For homogeneous surfaces or even isothermal areas, Wenbin et al. (2004) concludes that all three temperatures (aerodynamic, surface, and radiometric temperature) are numerically equivalent. That is not valid for heterogeneous surfaces because there is a degree of effects related to the lack of information on the influence of the molecular mean kinetic energy of surfaces that are not constituted by the same plant type under similar biomass development.

Since $T_o$ may not be measured in the field due to the challenges to address the aerodynamic height at which the sensible heat flux is originated, many researchers have tried to provide alternative methods to overcome that modeling issue when estimating evapotranspiration using the EBBM approach. Menenti and Choudhury (1993) were responsible to introduce the algorithm called surface energy balance index (SEBI) in which the main concept is to determine ET based on the identification of high and low reflectance areas in the satellite images that may provide the

gradient of identifying the crop water stress index (CWSI) parameter. Those pixels are often called "dry" and "wet" pixels because the characterization of a dry surface might be due to a maximum temperature and assumed low evapotranspiration rate, and a wet surface indicates watering conditions that will provide minimum temperature conditions to influence the assessment of ET using SEBI approach.

Another method of estimating surface heat fluxes using remote sensing data was developed by Bastiaanssen et al. (1998) and it was called surface energy balance algorithm for land (SEBAL). That algorithm is based on the idea of replacing the temperature gradient $T_o - T_a$ with a derivative term that accounts for the difference between the pixels that indicate the highest and lowest radiometric temperature which are often called, respectively, the "hot" and "cold" pixels of a given satellite image. Carrasco-Benevides et al. (2017) indicate that the SEBAL algorithm's accuracy might be strictly related to the sensibility of the user in terms of identifying the "hot" and "cold" pixels from the images processing analysis.

Roerink et al. (2000) presented an algorithm called simplified surface energy balance index (S-SEBI) that uses only data from RS images to estimate the surface heat fluxes rates and provides a spectral analysis for each pixel and integrate the 'hot' and 'cold' temperatures spatial variability for the images units.

Following the concepts of the SEBI method, Su (2002) introduced the surface energy balance system (SEBS) method for estimating surface heat fluxes using remote sensing data from satellite images and data from microclimate observations. Liou and Kar (2014) show that a remarkable different between SEBI and SEBS algorithms rely on the fact that SEBS applies estimates of sensible heat fluxes for the dry and wet conditions based on the atmospheric boundary layer of the system, instead of the atmospheric surface layer as reference for data measurement.

A more recent approach for estimating ET heat flux using the remote sensing data was developed by Allen et al. (2007) and called Mapping Evapotranspiration with Internalized Calibration (METRIC). The basic concept of METRIC is intrinsically related to the SEBAL algorithm introduced by Bastiaanseen et al. (2000), although there are some modifications for the calibration and validation of the ET estimates through ET data measured in situ instead of using only the evaporative fraction. In METRIC, the sensible heat flux is a function of the temperature gradient that exists between two different points located close to the ground surface, wind properties, and the roughness of the surface.

Alongside those methods to model ET without using $T_o$ when calculating the sensible heat flux on the EBBM, there are other methods that are applied considering the fluxes of the soil and vegetation as a two layer system instead of applying the estimation as a one major control volume. Those methods are called two-source methods. The introduction of an algorithm to consider the effects of soil and vegetation separately was done by Norman et al. (1995). The model basically consists on assuming the surface heat fluxes from the EBMM to be related to both soil and vegetation as independent heat sources that are interconnected through the heat transfer processes. The models of those heat fluxes are based on the capacity to obtain and use data from RS image processing analysis, such as brightness temperature from a certain view angle, leaf area index (LAI), and data from agricultural weather stations and canopy characteristics like wind speed, air temperature, net radiation, and canopy height. To overcome the complexity of estimating or measuring $T_o$, Norman et al. (1995) proposed the replacement of $T_o$ for the radiometric surface temperature, which might be calculated by having as input the fractional vegetation cover ($f_c$), the surface emissivity ($\epsilon_s$) and the temperature of the atmosphere regarding the sky conditions. Besides that, the aerodynamic resistance is adjusted based on the effective radiometric-convective resistance to acknowledge the fact that $T_s$ is being considered on the modeling process instead of $T_o$.

The methods so far mentioned attempt to eliminate the need of estimating the aerodynamic surface temperature. Chavez et al. (2005) provided an alternative method to include an estimation of $T_o$ in the sensible heat flux modeling. The approach to estimate $T_o$ into the algorithm to calculate ET from remote sensing data is often referred as the aerodynamic temperature method. That algorithm consists on using the EBBM approach to estimate ET as a residual term when knowing estimated values for $R_n$, H, and G. The difference from previous models is that the aerodynamic temperature approach attempts to use an empirical $T_o$ model approach to account for the fact that there is a direct connection between H and $T_o$ due to the processes of transferring energy from a given surface, as indicated by Chehbouni et al. (1996). The model to estimate $T_o$ is based on the measurements of sensible heat flux on site, as well as through a statistical multiple linear regression analysis with micro-meteorological parameters (wind speed, $T_a$, etc.) and remote sensing data (LAI, $T_s$, NDVI, etc).

## 2.1 Hypothesis and Objectives

The accuracy of modeling sensible heat flux is highly dependent on the accuracy of the temperature gradient between $T_o$ and $T_a$. The algorithms for ET based on remote sensing, when it comes to providing an alternative way to estimate H without dealing directly with the air temperature gradient, often do not represent their models with enough empirical and statistical evidence to validate their approximations. The issue caused by not having an understanding about what that gradient of temperature means when crop biomass and wind patterns change is critical to the validation of approaches to overcome the challenges of estimating $T_o$.

This research hypothesis claims that the aerodynamic temperature origination height is not constant during the growing season and it is affected by the wind direction in respect to crop distribution, wind speed patterns above the canopy, and biomass growth conditions that are modified due to plants biological processes induced mainly by water availability, soil texture, pores size and

arrangement of grains, salinity levels, organic matter concentration, soil water deficit, and micro-climate conditions expressed by the changes in air temperature, vapor pressure deficit, and wind speed.

The objectives of this research rely on the following goals:

(a) $T_o$ modeling regarding changes in biomass growth and wind patterns above the surface;

(b) Sensible heat flux modeling through the optimized $T_o$ models for different biomass conditions to provide estimates of $T_o$ to be applied on the bulk aerodynamic resistance model for H;

(c) Comparison between the optimized models for $T_o$ with other existing models to assess the progress of the research findings;

(d) An attempt to introduce a variable into the $T_o$ modeling processing to account for the influence of the wind direction relatively to the row crop orientation on the occurrence of $T_o$;

(e) Evaluation of remote sensing based models for canopy roughness length in the modeling of sensible heat as another measure to improve H estimation, and assess the influence of the crop row orientation on the estimation of $T_o$.

# Chapter 3

# Methodology

## 3.1 Experiment site description

The experiment was implemented on two 182 m x 107 m fields at the USDA-ARS Limited Irrigation Research Facility (LIRF) located nearby Greeley (CO) at approximated coordinates of latitude $40^o$ 26' 46.5" (N 40.44625), longitude $104^o$ 38' 13.5" (W 104.63708), and elevation of 1432 meters (figure 3.1). Two different irrigation water management practices were applied throughout the summer seasons of 2017 and 2018. Deficit irrigated treatment plot refers to the field in which the crop was allowed to undergo water stress conditions. Fully irrigated plot refers to the field without stress conditions due to satisfactory soil water content availability within the root zone profile. Both plots were corn fields irrigated based on subsurface drip system. The drip irrigation emitters were 30.5 cm apart from each other and buried 23 cm deep. The corn rows were 76 cm apart. Irrigation scheduling followed the standard approach based on the calculation of reference alfalfa ET (ASCE, 2005) obtained from the Colorado Mesonet Agricultural Weather Station Network (CoAgMet) and crop coefficients to obtain a representation of actual ET for the fields. The corn crop coefficients were regional coefficients as indicated by Garcia et al. (2013). The stress coefficient for determination of actual ET for the deficit irrigated field followed the FAO-56 standard approach based on the relationship among total available water (TAW), readily available water (RAW) and soil water deficit ($D_r$). The fields received different irrigation treatments in 2017 and 2018. Field 1 was the deficit irrigated plot in 2017 and the fully irrigated in 2018. Field 2 was the opposite treatment of Field 1 for each year of measurements. Tables 3.1 and 3.2 show, respectively, the dates and amount of irrigation water applied on the deficit and fully irrigated treatment plots in 2017 and 2018. Figure 3.2 and 3.3 show, respectively, the layout of of the sensors on both fields during the years of 2017 and 2018.

**Table 3.1:** Dates of irrigation water application on the deficit irrigated field at LIRF in 2017 and 2018.

| Year 2017 | | | Year 2018 | | |
|---|---|---|---|---|---|
| Date | DOY | Amount (mm) | Date | DOY | Amount (mm) |
| 7/1/2017 | 182 | 83.53 | 7/16/2018 | 197 | 92.46 |
| 9/19/2017 | 262 | 34.69 | 8/13/2018 | 225 | 107.19 |

**Table 3.2:** Dates of irrigation water application on the fully irrigated field at LIRF in 2017 and 2018.

| Year 2017 | | | Year 2018 | | |
|---|---|---|---|---|---|
| Date | DOY | Amount (mm) | Date | DOY | Amount (mm) |
| 7/11/2017 | 192 | 16.10 | 6/12/2018 | 163 | 50.70 |
| 7/18/2017 | 199 | 63.05 | 7/2/2018 | 183 | 50.70 |
| 7/25/2017 | 206 | 48.94 | 7/9/2018 | 190 | 48.26 |
| 8/8/2017 | 220 | 40.57 | 7/23/2018 | 204 | 78.74 |
| 8/22/2017 | 234 | 52.78 | 8/10/2018 | 222 | 88.90 |
| 8/29/2017 | 241 | 35.14 | 8/26/2018 | 238 | 76.20 |
| 9/12/2017 | 255 | 79.65 | 9/10/2018 | 253 | 22.86 |
| 9/19/2017 | 262 | 31.40 | 9/14/2018 | 257 | 58.42 |

The climate condition during summer season at Greeley is similar to arid regions located in low-latitude semiarid. Koppen climate classification for that area is BSk, which stands for tropical and subtropical desert climates. Average air temperature during the warmest month (July) is 22 °C, and average rainfall water depth during the wettest month (May) is 63 mm.


**Figure 3.1:** Top view of the fields at LIRF.

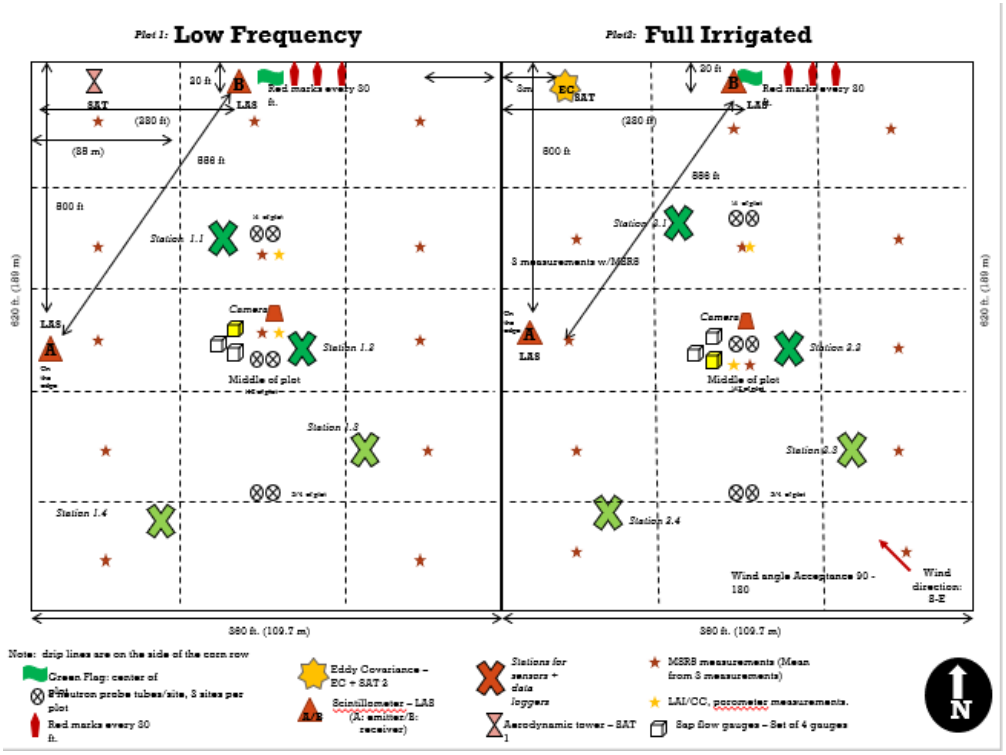


**Figure 3.2:** Layout of the sensors at LIRF in 2017. Provided by Maria Cristina Capurro.

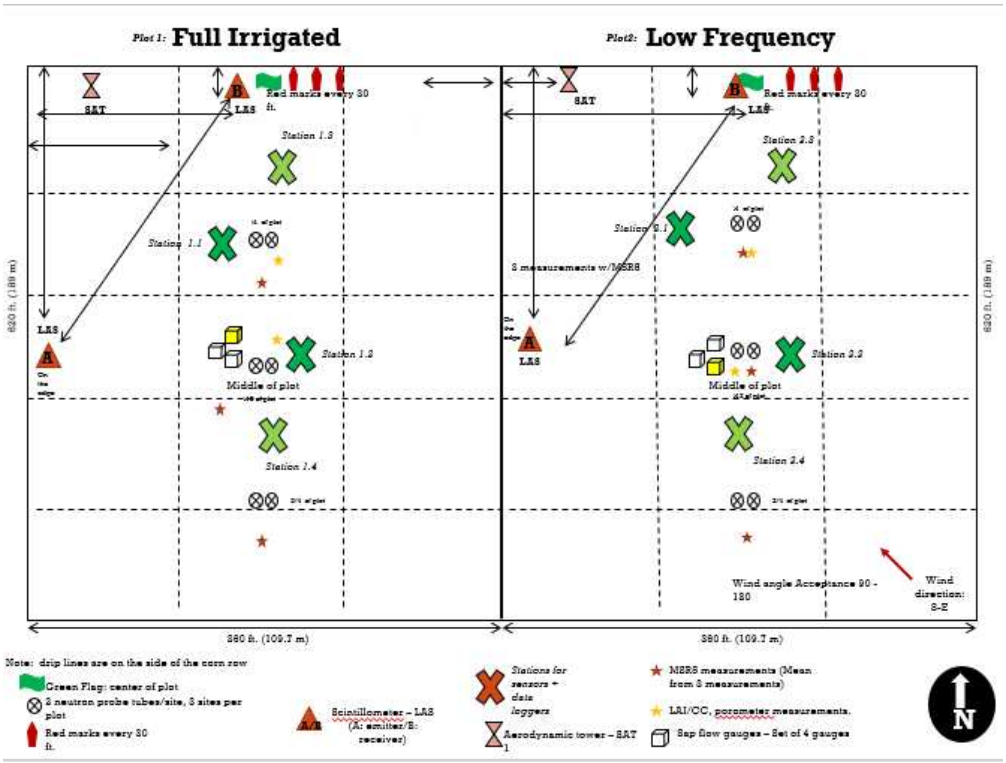


**Figure 3.3:** Layout of the sensors at LIRF in 2018. Provided by Maria Cristina Capurro.

Relative humidity and air temperature probe sensors alongside anemometers were installed as part of the aerodynamic flux towers to measure weather data (relative humidity, air temperature, and wind speed) on site for both modeling $T_o$, H, and indirectly measuring sensible heat flux using the Bowen ratio and aerodynamic profile method. Large aperture scintillometers (LAS) were used to obtain measurements of H. Total of 120 sensors (60 sensors per field) were installed to collect data measuring all components of the EBBM. Measured data includes, but not limited to, surface temperature, net radiation, soil water content at different depths, soil heat flux, soil temperature, and multispectral canopy reflectance). Air temperature, relative humidity, and wind speed were measured for each field at a height of 3.3 m above ground surface during the growing season of 2017 and 2018. Table 3.3 shows the summary of the sensors installed for measuring all data needed for the development and assessment of $T_o$ and H models.

**Table 3.3:** Summary of the sensors for measuring data to derive and assess $T_o$ and H models at LIRF.

| Sensor type | Model type | Manufacturer Name | Manufacturer Location |
|---|---|---|---|
| Multispectral radiometer | MSR5 | Cropscan, Inc | Rochester, MN, USA |
| Soil water content | 5TE | Decagon Devices, Inc | Pullman, WA, USA |
| Temperature probe | T107 | Campbell Scientific, Inc | Logan, UT, USA |
| Soil heat flux plate | HFT3-L | Campbell Scientific, Inc | Logan, UT, USA |
| Net radiometer | CNR01 | Kipp and Zonen | Delft, The Netherlands |
| Net radiometer | NR-Lite | Kipp and Zonen | Delft, The Netherlands |
| Infrared thermometer (IRT) | SI-111 | Apogee Instruments | Logan, UT, USA |
| Air temperature and relative humidity | HMP45C | Vaisala | Vantaa, Finland |
| Large Aperture Scintillometers | XLAS | Kipp and Zonen | Delft, The Netherlands |
| Wind speed cup anemometer | 03101-L | Campbell Scientific, Inc | Logan, UT, USA |
| Eddy covariance 3D sonic anemometer | CSAT3 | Campbell Scientific, Inc | Logan, UT, USA |
| Eddy covariance open path krypton hygrometer | KH20 | Campbell Scientific, Inc | Logan, UT, USA |
| Eddy covariance barometric pressure sensor | CS106 | Campbell Scientific, Inc | Logan, UT, USA |
| Eddy covariance fine wire thermocouple | FW03 | Campbell Scientific, Inc | Logan, UT, USA |

## 3.2 Sensible Heat Flux Modeling

The modeling of sensible heat flux was done based on the bulk aerodynamic resistance approach indicated by equation 3.1:

$$H = \rho_a \cdot Cp_a \cdot \left( \frac{T_o - T_a}{r_{ah}} \right) \tag{3.1}$$

where $\rho_a$ is the air density ($Kg/m^3$); $Cp_a$ is the specific heat of the air ($\approx$ 1005 J/Kg/K); and $r_{ah}$ is the aerodynamic resistance (s/m).

Remote sensing variables were introduced into the modeling process for sensible heat flux. The calculation of zero-displacement height (d) and roughness length for momentum ($z_{om}$) were done as indicated by Choudhury and Monteith (1988) model based on crop height and leaf area index (LAI) and following the recommendations of Tian et al. (2011). That is due to the fact that

the standard approach in which d and $z_{om}$ are functions of only crop height may not be valid for field conditions where surface heterogeneity or soil-water stressed conditions of the canopy are often identified throughout the growing season (Campbell and Norman, 1998). Shaw and Pereira (1982) have shown that there is a relationship between plant biomass and zero-displacement height that indicates the potential of adjusting the estimations of canopy roughness length as a function of biomass changes. Different publications have proposed the approach for a given representative biomass range that would fit into most agricultural crops (Shaw and Pereira, 1998; Maki, 1975). However, the differences into biomass development from different crops and even within different species of the same vegetation type belong to a set of factors that influence directly the heat and water vapor exchange between soil, plants, and atmosphere.

Equations 3.2 and 3.3 indicate, respectively, the expressions for calculating $z_{om}$ and d.

$$z_{om} = \begin{cases} z'_o + 0.28 \cdot h_c \cdot \sqrt{X}, \;\; if \;\; 0 \leq X \leq 0.2 \\ \\ 0.3 \cdot h_c \cdot \left(\dfrac{1-d}{h_c}\right), \;\; if \;\; 0.2 < X \leq 2 \end{cases} \tag{3.2}$$

$$d = h_c \cdot \left[ ln(1 + X^{1/6}) + 0.03 \cdot ln(1 + X^6) \right] \tag{3.3}$$

where $X = 0.20 \cdot LAI$; $z_o$' is the roughness length of the soil surface and assumed to be 0.01 m; $h_c$ is the crop height (m).

## 3.3 Determination of Remote Sensing Vegetation Indexes for Modeling $T_o$ and H Based on LIRF Data

### 3.3.1 Normalized Difference Vegetation index (NDVI)

NDVI is used to characterize the presence of vegetation on remote sensing imagery analysis and it is calculated as given by equation 3.4:

$$NDVI = \frac{NIR - RED}{NIR + RED} \tag{3.4}$$

where NIR and RED are, respectively, the near infrared and red surface reflectance data from the visible spectrum.

NIR and RED reflectance data were obtained through on site using the radiometer MSR5. Measurements took place once a week, in 2017, and twice a week in 2018 at north, center, and south locations on both fields and averaged for a given day of measurement. Interpolation models were developed to associate NDVI as a function of the Day of the Year (DOY) to provide estimates for the days without ground-based measurements. The biological processes of plant growth take place on a continuous, but seasonal pace that allows the assumption that the vegetation parameters do not change significantly during a given day. Table 3.4 shows the dates in which the measurements of reflectance were done in 2017 and 2018.

**Table 3.4:** Dates of MSR5 measurements on both fields in 2017 and 2018.

| Year 2017 | | Year 2018 | | | |
|---|---|---|---|---|---|
| Date | DOY | Date | DOY | Date | DOY |
| 7/3/2017 | 184 | 7/6/2018 | 187 | 8/24/2018 | 236 |
| 7/11/2017 | 192 | 7/13/2018 | 194 | 8/28/2018 | 240 |
| 7/20/2017 | 201 | 7/20/2018 | 201 | 8/31/2018 | 243 |
| 7/24/2017 | 205 | 7/24/2018 | 205 | 9/4/2018 | 247 |
| 7/27/2017 | 208 | 7/27/2018 | 208 | 9/7/2018 | 250 |
| 8/14/2017 | 226 | 7/31/2018 | 212 | 9/11/2018 | 254 |
| 8/24/2017 | 236 | 8/7/2018 | 219 | 9/14/2018 | 257 |
| 9/1/2017 | 244 | 8/10/2018 | 222 | 9/18/2018 | 261 |
| 9/12/2017 | 255 | 8/14/2018 | 226 | 9/21/2018 | 264 |
| 9/19/2017 | 262 | 8/17/2018 | 229 | 9/25/2018 | 268 |
| 9/26/2017 | 269 | 8/21/2018 | 233 | | |

For both fields, NDVI values were initially calculated using equation 3.4. Then, a non-linear regression analysis procedure was performed using the MATLAB Curve Fitting Toolbox to obtain the best curve fitting that would relate NDVI and DOY. The assumption that remote sensing based indexes are constant within a day was done to approximate the $T_o$ and H modeling scenarios to the conditions in which airborne or satellite imagery are used as a representation of the field conditions for estimation of instantaneous surface heat fluxes that are applied for obtaining daily rates of evapotranspiration for vegetated surfaces. The equations 3.5 ($R^2 = 0.98$) and 3.6 ($R^2 = 0.94$), respectively, are the results of the curve fitting method for deficit and fully irrigated fields in 2017. For 2018 data, equations 3.7 ($R^2 = 0.89$) and 3.8 ($R^2 = 0.93$) indicate the interpolated equations for, respectively, deficit and fully irrigated treatments.

$$NDVI_{17d} = 0.5489 + 0.272 \cdot cos(0.0568 \cdot DOY) - 0.1213 \cdot sin(0.05068 \cdot DOY) \tag{3.5}$$

$$NDVI_{17f} = 3.051 \cdot exp(-0.00485 \cdot DOY) - 6590 \cdot exp(-0.04821 \cdot DOY) \tag{3.6}$$

$$NDVI_{18d} = 0.7831 \cdot sin(0.02843 \cdot DOY + 1.433) \tag{3.7}$$

$$NDVI_{18f} = 0.8563 \cdot sin(0.01564 \cdot DOY + 4.417) \tag{3.8}$$

where the subscripts 17d, 17f, 18d, and 18f are, respectively, to identify the year ("17" = 2017 and "18" = 2018) and the irrigation treatment ("d" for deficit irrigated and "f" for fully irrigated).

### 3.3.2 Fractional Percent Cover ($f_c$)

The fractional vegetation cover was be calculated as a function of the remote sensing based index NDVI.

Johnson and Trout (2012) developed an empirical model to relate NDVI to the percentage of vegetation cover for different crop types. The model is indicated by equation 3.9:

$$f_c = \begin{cases} 1.26 \cdot NDVI - 0.18, \;\; if \;\; NDVI \geq 0.15 \\ 0, \;\; if \;\; NDVI < 0.15 \end{cases} \tag{3.9}$$

### 3.3.3 Calculation of Leaf Area Index

Leaf area index is a vegetation index that relates the unit area of one side of the leaf and the unit area of the ground surface. LAI might be obtained through both measurements or empirical and semi-empirical equations. The estimation of LAI was done by using the empirical approach for sorghum and corn crops developed by Chavez et al. (2009) that relates LAI ($m^2/m^2$) and the optimized soil adjusted vegetation index (OSAVI):

$$LAI = 0.263 \cdot exp(3.813 \cdot OSAVI) \tag{3.10}$$

### 3.3.4 Calculation of OSAVI

OSAVI vegetation index is a modified version of NDVI developed by Rondeaux et al. (1996) that attempts to minimize the interference caused by the exposed soil on reflectance readings. Equation 3.11 shows the general expression for OSAVI:

$$OSAVI = \frac{(NIR - RED) \cdot (1 + L)}{NIR + RED + L} \tag{3.11}$$

where L is the adjusted factor term that reduces the interference caused by the soil on the vegetation index.

Rondeaux et al. (1996) indicated that $L = 0.16$ is the optimizing value for OSAVI. Equations 3.12 ($R^2 = 0.98$) and 3.13 ($R^2 = 0.94$) indicate the interpolation models for, respectively, deficit and fully irrigated treatments in 2017. Equations 3.14 ($R^2 = 0.89$) and 3.15 ($R^2 = 0.93$) show the interpolation equations for, respectively, the deficit and fully irrigated fields. The interpolated method followed the same procedure for NDVI interpolation and was developed using the MATLAB curve fitting toolbox.

$$OSAVI_{17d} = 0.5472 + 0.2724 \cdot cos(0.05075 \cdot DOY) - 0.1167 \cdot sin(0.0575 \cdot DOY) \tag{3.12}$$

$$OSAVI_{17f} = 3.043 \cdot exp(-0.004854 \cdot DOY) - 6571 \cdot exp(-0.04821 \cdot DOY) \tag{3.13}$$

$$OSAVI_{18d} = 0.6803 \cdot sin(0.02925 \cdot DOY + 7.516) \tag{3.14}$$

$$OSAVI_{18f} = 0.7638 \cdot sin(0.01767 \cdot DOY + 3.974) \tag{3.15}$$

The subscripts on equations 3.12 to 3.15 follow the same criteria for NDVI equations 3.5 to 3.8.

### 3.3.5 Interpolation of Crop Height ($h_c$)

Crop height and phenology data were measured throughout the growing season for both fields during each year of measurement. Tables 3.5 and 3.6 indicate the measurements dates and crop height values in 2017 and 2018 for, respectively, deficit and fully irrigated treatment plots. Tables 3.7 and 3.8 provide information about the phenology growth stage in 2017 and 2018 for, respectively, the deficit and fully irrigated treatment fields. To interpolate the crop height for the days without measurements, MATLAB curve fitting toolbox was used to determine the best model for $h_c$ as function of DOY. Equations 3.16 ($R^2 = 0.99$) and 3.17 ($R^2 = 0.99$) are, respectively, the model for crop height on the deficit and fully irrigated fields in 2017. Regarding the 2018 data, equations 3.18 ($R^2 = 0.99$) and 3.19 ($R^2 = 0.99$) show the models for the deficit and fully irrigated plots.

$$hc_{17d} = 97.89 - 61.74 \cdot cos(0.04138 \cdot DOY) - 48.34 \cdot sin(0.04138 \cdot DOY) \tag{3.16}$$

$$hc_{17f} = 130.1 + 68.3 \cdot cos(0.04979 \cdot DOY) - 92.6 \cdot sin(0.04979 \cdot DOY) \tag{3.17}$$

$$hc_{18d} = 122.4 + f_1(DOY) + f_2(DOY) \tag{3.18}$$

$$hc_{18f} = 109.3 + f_3(DOY) + f_4(DOY) \tag{3.19}$$

where equations 3.16 to 3.19 provide interpolated values of crop height in cm and the respective subscripts follow the same approach as for NDVI and OSAVI interpolated equations. The functions $f_1$(DOY), $f_2$(DOY), $f_3$(DOY) and $f_4$(DOY) are indicated by equations 3.20 to 3.23:

$$f_1(DOY) = -110.2 \cdot cos(0.04039 \cdot DOY) - 17.16 \cdot sin(0.04039 \cdot DOY) \tag{3.20}$$

$$f_2(DOY) = 39.5 \cdot cos(0.08078 \cdot DOY) - 8.711 \cdot sin(0.08078 \cdot DOY) \tag{3.21}$$

$$f_3(DOY) = 6.623 \cdot cos(0.03044 \cdot DOY) - 17.16 \cdot sin(0.03044 \cdot DOY) \tag{3.22}$$

$$f_4(DOY) = 24.11 \cdot cos(0.06088 \cdot DOY) - 8.711 \cdot sin(0.06088 \cdot DOY) \tag{3.23}$$

**Table 3.5:** Crop height measurements for both treatment fields in 2017.

| | | Deficit irrigated | Fully Irrigated |
|---|---|---|---|
| Date | DOY | $h_c$ | $h_c$ |
| [-] | [-] | [m] | [m] |
| 6/13/2017 | 164 | 0.20 | 0.20 |
| 6/30/2017 | 181 | 0.28 | 0.32 |
| 7/7/2017 | 188 | 0.49 | 0.60 |
| 7/14/2017 | 195 | 0.67 | 0.83 |
| 7/19/2017 | 200 | 0.83 | 1.18 |
| 7/26/2017 | 207 | 0.98 | 1.57 |
| 8/2/2017 | 214 | 1.15 | 2.00 |
| 8/9/2017 | 221 | 1.42 | 2.30 |
| 8/15/2017 | 227 | 1.70 | 2.30 |
| 9/1/2017 | 244 | 1.73 | 2.32 |

**Table 3.6:** Crop height measurements for both treatment fields in 2018.

| | | Deficit irrigated | Fully Irrigated |
|---|---|---|---|
| Date | DOY | $h_c$ | $h_c$ |
| [-] | [-] | [m] | [m] |
| 5/25/2018 | 145 | 0.10 | 0.10 |
| 7/6/2018 | 187 | 0.96 | 0.99 |
| 7/13/2018 | 194 | 1.01 | 1.39 |
| 7/19/2018 | 200 | 1.20 | 1.80 |
| 7/26/2018 | 207 | 1.49 | 1.87 |
| 8/3/2018 | 215 | 1.57 | 1.92 |
| 8/10/2018 | 222 | 1.58 | 1.95 |
| 8/20/2018 | 232 | 1.58 | 1.95 |
| 8/26/2018 | 238 | 1.58 | 1.98 |
| 9/8/2018 | 251 | 1.63 | 2.01 |
| 9/15/2018 | 258 | 1.63 | 2.01 |
| 9/22/2018 | 265 | 1.63 | 2.01 |

**Table 3.7:** Corn phenology for both irrigation treatment plots in 2017.

| Date | Deficit irrigated | Fully Irrigated |
|---|---|---|
| 6/13/2017 | V3 | V3 |
| 6/28/2017 | V5 | V5 |
| 7/7/2017 | V5 to V6 | V7 |
| 7/14/2017 | V7 to V8 | V8 to V9 |
| 7/19/2017 | V8 | V9 |
| 7/26/2017 | V9 to V10 | V11 to V12 |
| 8/02/2017 | V11 to V12 | V15 |
| 8/9/2017 | V14 to V15 | R1 |
| 8/15/2017 | R1 to R2 | R2 |
| 9/1/2017 | R3 | R3 |
| 9/22/2017 | R4 | R4 |
| 9/29/2017 | R5 | R5 |
| 10/6/2017 | R6 | R6 |

**Table 3.8:** Corn phenology for both irrigation treatment plots in 2018.

| Date | Deficit irrigated | Fully Irrigated |
|---|---|---|
| 5/25/2018 | V2 | V2 |
| 7/6/2018 | V6 | V6 |
| 7/13/2018 | V6 | V6 to V8 |
| 7/19/2018 | V6 | V10 |
| 7/26/2018 | V10 to V12; Silking | V12 to V15; Silking |
| 8/3/2018 | V10 to V12; Silking | V12 to V15; Silking |
| 8/10/2018 | V12/Silking | V12 to V15; Silking |
| 8/26/2018 | R2 | R2 to R3 |
| 9/8/2018 | R4 | R4 |
| 9/15/2018 | R5 | R5 |
| 9/22/2018 | R6 | R6 |

### 3.3.6 Calculation of the Aerodynamic Resistance ($r_{ah}$)

For neutral conditions in which adiabatic conditions of the atmosphere prevail, the aerodynamic resistance is calculated using bulk resistance approach indicated by equation 3.24:

$$r_{ah} = \frac{ln\left(\frac{Z_m - d}{z_{om}}\right) \cdot ln\left(\frac{Z_m - d}{z_{oh}}\right)}{u \cdot k^2} \tag{3.24}$$

where $Z_m$ is the height at which wind speed is measured (m); u is the wind speed at height $Z_m$ (m/s); k is the Von Karman constant (0.41); and $r_{ah}$ is given in s/m.

Monin and Obukhov (1954) demonstrated that the resistance factor must be corrected for atmospheric stability, since the conditions on site are not often under adiabatic heat exchange. Therefore, the adjusted $r_{ah}$ is given by equation 3.25 (Yasuda, 1988):

$$r_{ah} = \frac{ln\left(\frac{Z_m - d}{z_{oh}}\right) - \psi_h}{u_* \cdot k} \tag{3.25}$$

where $u_*$ is the friction velocity (m/s); $\psi_h$ is the atmospheric stability correction function for heat transfer; $z_{oh}$ is the roughness length for Heat (m) and it was calculated as approximately 10 % of $z_{om}$ (Brutsaert, 1982).

The atmospheric stability corrections are dependant on the canopy roughness elements, height of wind speed measurements, and the Monin-Obukhov stability length ($L_{MO}$). $L_{MO}$ is calculated as indicated by Monin-Obukhov (1954):

$$L_{MO} = -\frac{u_*^3 \cdot T_a \cdot \rho_a \cdot Cp_a}{g \cdot k \cdot H} \tag{3.26}$$

where g is the gravity acceleration (9.81 $m/s^2$).

Monin and Obukhov (1954) indicates that $L_{MO}$ is significant large when the atmosphere under near neutral conditions. Therefore, the initial calculation of $u_*$ for neutral atmospheric conditions followed equation 3.27:

$$u_* = \frac{u \cdot k}{ln\left(\frac{Z_m - d}{z_{om}}\right)} \tag{3.27}$$

However, when the conditions are not neutral, a correction factor must be introduced into the calculation of $u_*$ to account for atmospheric stability conditions. Then, the corrected $u_*$ equation is shown by equation 3.28 (Yasuda, 1988):

$$u_* = \frac{u \cdot k}{ln\left(\frac{Z_m - d}{z_{om}}\right) + \psi_m} \tag{3.28}$$

The determination of the stability correction functions followed the approach developed by Yasuda (1988). For unstable atmospheric conditions, in which air temperature decreases with an increase in height ($L_{MO} < 0$):

$$\psi_h = 2 \cdot ln\left(\frac{1 + x_2^2}{2}\right) - 2 \cdot ln\left(\frac{1 + x_1^2}{2}\right) \tag{3.29}$$

$$\psi_m = \psi_{m2} - \psi_{m1} \tag{3.30}$$

where:

$$\psi_{m2} = 2 \cdot ln\left(\frac{1 + x_3^2}{2}\right) + ln\left(\frac{1 + x_3^2}{2}\right) - 2 \cdot atan(x_3) + \frac{\pi}{2} \tag{3.31}$$

$$\psi_{m1} = 2 \cdot ln\left(\frac{1+x_1^2}{2}\right) + ln\left(\frac{1+x_1^2}{2}\right) - 2 \cdot atan(x_1) + \frac{\pi}{2} \tag{3.32}$$

$$x_1 = \left[1 - \frac{16 \cdot (Z_m - d)}{L_{MO}}\right]^{0.25} \tag{3.33}$$

$$x_2 = \left[1 - \frac{16 \cdot z_{oh}}{L_{MO}}\right]^{0.25} \tag{3.34}$$

$$x_3 = \left[1 - \frac{16 \cdot z_{om}}{L_{MO}}\right]^{0.25} \tag{3.35}$$

For stable atmospheric conditions, in which air temperature increases with an upward increment in height ($L_{MO} > 0$):

$$\psi_h = 6 \cdot ln\left(1 - \frac{Z_m}{L_{MO}}\right) \cdot \left[\frac{z_{om}}{L_{MO}} - \frac{Z_m - d}{L_{MO}}\right] \tag{3.36}$$

$$\psi_m = \psi_h \tag{3.37}$$

## 3.4 Aerodynamic Surface Temperature Modeling

$T_o$ was modeled following linear and non-linear equations to incorporate the effects of weather and surface properties on the occurrence of the temperature that originates the air temperature gradient of heat transfer between surface and nearby atmosphere and to be able to identify the type of model that provides better estimation of $T_o$. The modeling for $T_o$ becomes an artifice to be applied on remote sensing based methods to estimate surface energy balance heat flux for agricultural applications. The general linear and non-linear model types for $T_o$ are indicated by equations 3.38 and 3.39, respectively:

$$T_o = a_1 \cdot f_c + a_2 \cdot T_a + a_3 \cdot T_s + a_4 \cdot r_p + a_5 \tag{3.38}$$

$$T_o = T_a + p_1 \cdot ln|T_s - T_a| + p_2 \cdot \frac{r_p}{f_c} + p_3 \tag{3.39}$$

where $r_p$ is the new term named turbulent-mixing row resistance (s/m); $a_i$ and $p_i$ are fitted coefficients for the empirical models.

The development of the $r_p$ variable was based on the early work of Thom (1972) that approximate the bulk aerodynamic resistance as inversely proportional to wind speed as a predictor for turbulence and a drag coefficient for a given wind speed magnitude. Since $r_p$ is proposed to be a variable that might be representative for the interactions between the wind flowing above the surface and the crop row orientation, the drag coefficient term was replaced by a variable that attempts to represent the relative orientation of the wind in regards to the crop row.

Air temperature was measured on site using the cross-arm of each aerodynamic flux Towers at a height of 3.3 m above ground surface. Surface temperature was measured using Infrared Thermometers (IRT), raised every week to allow measurements to be done at 1 m above the canopy height, perpendicularly to the ground surface, and facing downwards (NADIR view).

Wind speed was measured at a height of 3.3 m above ground surface at each site. Wind speed direction was obtained on site, in 2017, through the eddy covariance measurements from the wind direction compass system at 3.5 m height. For 2018, the direction of wind was acquired from the CoAgMet station Greeley 04 (GLY04) located on the LIRF site. GLY04 weather station is located at Latitude of 40.4487 and longitude of -104.6380 northwest of the fields and above fully well-watered grass kept at a height of 0.12 m above ground. The wind speed direction measurements were done at a height of 2 m above ground surface. For the development of the $T_o$ model, it is

assumed that the wind speed direction at the weather station was equivalent to the treatment plots since the GLY04 CoAgMet station is located within the facility.

Only unstable atmospheric conditions ($H > 0$) were considering when modeling $T_o$ and assessing models for sensible heat flux since most of the daytime ($R_n > 0$) filtered data for wind speed direction at LIRF were under $T_s > T_a$ conditions. Daytime data were chosen due to the fact that most remote sensing based applications on estimating surface heat fluxes collect data for calculations between late morning and early afternoon. Figure 3.4 shows the pattern of $T_s$ and $T_a$ for daytime data in on both fields at LIRF combining 2017 and 2018 data sets.

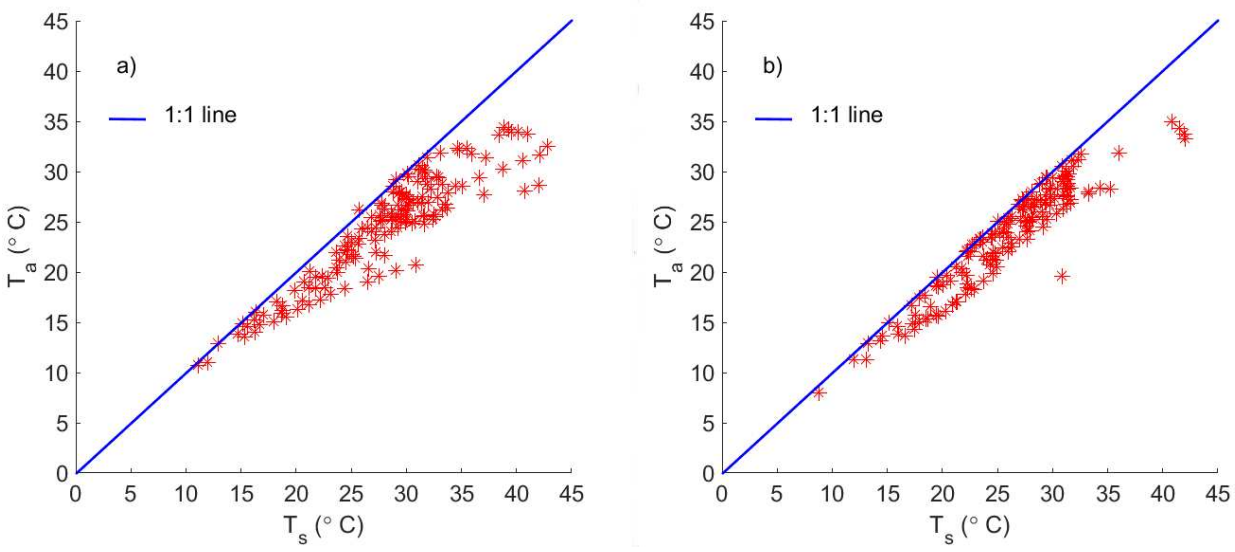


**Figure 3.4:** $T_s$ vs. $T_a$ at LIRF for different irrigation treatment practices in 2017-2018 data set. Graphs 3.4(a) and 3.4(b) show, respectively, the plots of surface temperature vs. on-site air temperature for the deficit and fully irrigated fields when 2017 and 2018 data are combined.

### 3.4.1 Calculation of Inverted $T_o$

In order to obtain a reference value for the aerodynamic surface temperature, the term inverted $T_o$ was assigned to indicate the magnitude of that given temperature based on the measured sensible heat data obtained from the LAS measurements. Inverted $T_o$ was calculated by solving the

bulk aerodynamic resistance equation for $T_o$, indicated by equation 3.40:

$$T_{oi} = T_a + \left( \frac{H_{LAS} \cdot r_{ah}}{Cp_a \cdot \rho_a} \right) \tag{3.40}$$

where $T_{oi}$ is the inverted $T_o$ (°C) and $r_{ah}$ is calculated based on the data from LAS.

The aerodynamic resistance based on data from LAS was calculated using the LAS estimated friction velocity and Monin-Obukhov atmospheric stability length. The canopy roughness elements (d, $Z_{om}$, and $Z_{oh}$) were calculated as indicated by Kipp and Zonen (2007). The corrections for atmospheric stability followed the approach by Yasuda (1988). The inverted $T_o$ approach was used to evaluate the models for the surface aerodynamic temperature and to derive the proposed empirical models. The modeling process for the aerodynamic surface temperature was performed using LAS H data for the inverted $T_o$ under unstable atmospheric conditions, when sensible heat flux is positive and away from the surface. That is due to the fact that most of applications of remote sensing associated to the estimation of surface heat fluxes and evapotranspiration are done during daytime around noon or early afternoon, in which the nearby atmosphere is often under unstable conditions, except on limited situations when the surface is wet due to irrigation or rainfall events.

### 3.4.2 Published $T_o$ Equations to Evaluate Proposed $T_o$ Models Performance

In order to assess improvement on modeling $T_o$, the models developed by Chavez et al. (2005) and Chehbouni et al. (1996) were chosen to assess the potential results improvements of the proposed models.

Chavez et al. (2005) developed a multiple linear regression model for $T_o$ based on remote sensing and weather data empirically developed for corn under sub-humid climate conditions. The model published is indicated by equation 3.41 ($R^2 = 0.77$):

$$T_o = 0.534 \cdot T_s + 0.39 \cdot T_a + 0.224 \cdot LAI - 0.192 \cdot u + 1.67 \tag{3.41}$$

where $T_a$ and $T_s$ are given in °C, and u is on units of m/s.

Chehbouni et al. (1996) developed a semi-empirical model to estimate the temperature gradient that derives the occurrence of sensible heat flux based on LAI and $T_s$ and was developed for sparse vegetation types under semi-arid climate conditions. Equation 3.42 indicates the referred model:

$$T_o - T_a = \frac{T_s - T_a}{exp\left(\frac{1.5}{1.5 - LAI}\right) - 1} \tag{3.42}$$

where $T_a$ and $T_s$ are given in °C.

## 3.5 Determination of Turbulence Mixing Row Resistance ($r_p$)

There are few publications that try to explain the potential influence of row crop layout on the transfer of momentum and heat from the surface to the atmosphere. McInnes et al. (1995) have indicated that, depending on the trajectory of air flowing above the canopy, its interaction with the crop row orientation has a direct effect on the conductance of heat and influences the processes that derive the exchange of energy at the surface level.

The work developed by Thom (1972), following the efforts by McIntosh and Thom (1969) to characterize the mechanism of mass, heat, and momentum transfer, has indicated that aerodynamic resistance to heat transfer might be generally expressed by the following expression:

$$r_{ah}(z) = \frac{1}{u(z)} \cdot \left[CD(z)\right]^{-1}, \quad if \quad z \geq h_c \tag{3.43}$$

where $r_{ah}(z)$ is the aerodynamic resistance term determined from wind speed measurement at a general height (z) above ground (s/m), u(z) is the mean wind speed at height of measurement z above ground surface (m/s), and CD(z) is the bulk drag coefficient associated to the height z (dimensionless).

From Thom (1972), resistance based terms could be inferred to be represented by the product of a dimensionless term that accounts for nature of the resistance variable and the inverse of the wind speed. Consider that wind which directions are closer to the crop row orientation will provide better conditions for transfer of heat and momentum. That could be explained based on the air flowing above canopy not being affected by as many elements as when air crosses the field on a more oblique direction.

The assumption that there will be more constrains from the top of the surface when the wind is blowing from an originated direction that is not entirely aligned with the crop layout seems to be a reasonable argument. Regarding the turbulence factor, the more turbulence - indicated by high values of wind speed - the less resistance for heat and momentum transfer since the mechanisms of mixing of the air and vapor are easily activated by the degree of turbulence caused by the unpredictable movement of particles within the atmosphere. That assumption may indicate that resistance and wind speed are inversely related. Besides that, wind flowing above the canopy under the same trajectory, but with opposite directions, will have the same relative angle towards the crop row layout, considering that row are homogeneously aligned on the same orientation and with similar biomass development.

Therefore, as a way to incorporate the influence of canopy row orientation and wind characteristics into the modeling of $T_o$, the $r_p$ term includes a relative wind direction factor ($\tau$) related to

ratio between wind speed direction ($\theta_u$) and the degree of wind trajectory regarding the direction of wind above the canopy in relation to the corn row orientation ($\theta_r$) and the turbulent mixing of air above the canopy expressed as the wind speed. $\theta_r$ might be defined as the horizontal angle from the crop row towards the wind vector that follows an anticlockwise direction. $\theta_u$ is the horizontal angle where the wind is coming from in regards to the magnetic north.

Equation 3.44 presents the proposed expression for the turbulent-mixing row resistance as the following:

$$r_p = \tau \cdot \frac{1}{u} \tag{3.44}$$

where u is the wind speed (m/s); $\tau$ is the relative wind direction factor (dimensionless).

## 3.6 Relative Wind Direction Factor

The $\tau$ factor is given by the equation 3.45 as the ratio between the wind speed direction and the relative wind direction to the crop row layout.

$$\tau = \begin{cases} \dfrac{\theta_u}{\theta_r}, & \theta_u \leq \theta_r \\ \\ \dfrac{\theta_r}{\theta_u}, & \theta_u > \theta_r \end{cases} \tag{3.45}$$

The main assumption regarding the relative wind direction factor ($\tau$) is that air flowing in reversed directions must have the same relative angle regarding the crop row layout. To account for that, the surface must be divided into 4 quadrants (figure 3.5) to properly incorporate the different

scenarios of wind direction. That assumption allows the determination of $\tau$ to be done for pairs of opposite quadrants on the horizontal plane that represent the surface. The referred pairs will be designated as first and third (1Q, 3Q) and second and fourth quadrants (2Q, 4Q). Table 3.9 shows the range of wind speed direction on each quadrant.

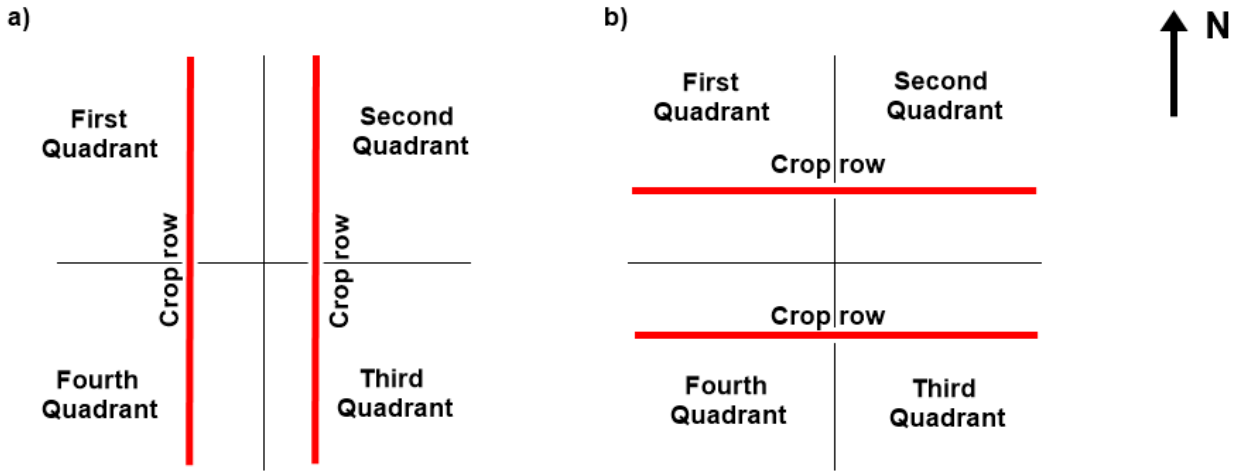


**Figure 3.5:** Graphical representation of the quadrants and the crop layout. Figure 3.5(a) represents the scenario in which the crop row is oriented north-south or south-north. Figure 3.5(b) indicates the crop layout west-east or east-west.

**Table 3.9:** Wind speed direction range of values for each horizontal quadrant on the surface.

| Quadrant | ID code | Wind direction range |
|---|---|---|
| First Quadrant | 1Q | $270^o < \theta_u \leq 360^o$ |
| Second Quadrant | 2Q | $0^o \leq \theta_u \leq 90^o$ |
| Third Quadrant | 3Q | $90^o < \theta_u \leq 180^o$ |
| Fourth Quadrant | 4Q | $180^o < \theta_u \leq 270^o$ |

The calculation of $\tau$ depends on the orientation of the crop row layout on the field. That is due to the fact that wind speed direction is given as an azimuth angle and the relative angle to crop row

will take different orientation depending if the rows are oriented north-south or east-west. Figure 3.6 represents that concept.

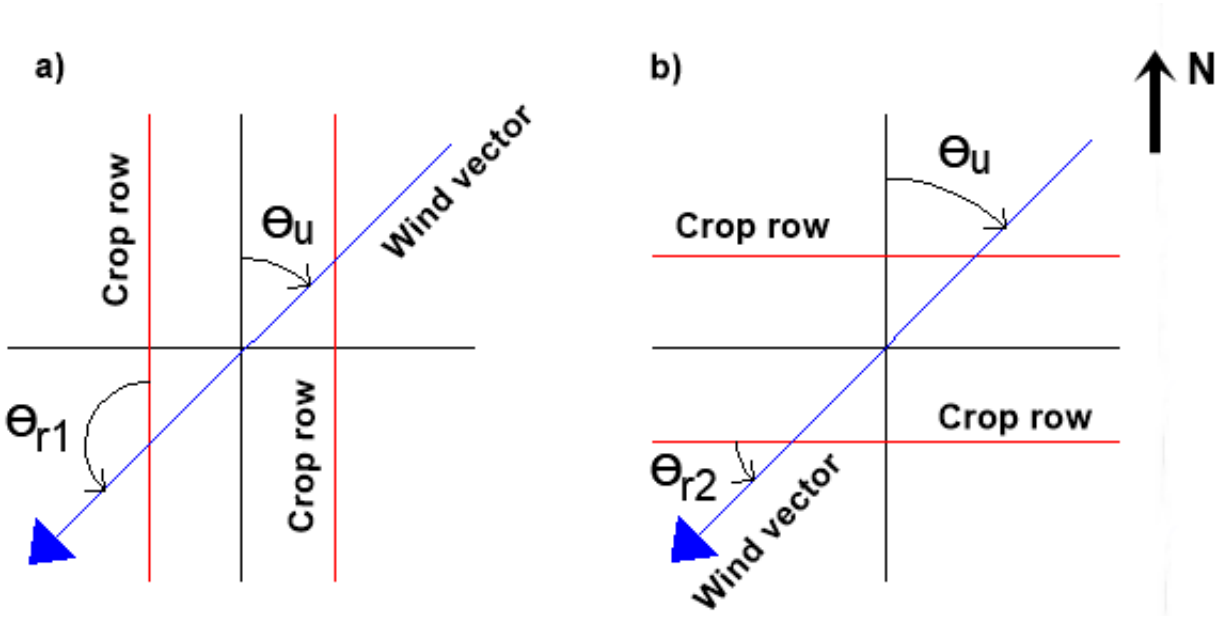


**Figure 3.6:** $\theta_r$ determination depending on the crop row orientation. Figure 3.6(a) represents the scenario in which the crop row is oriented north-south or south-north. Figure 3.6(b) indicates the crop layout west-east or east-west.

### 3.6.1 Relative Wind Direction Factor for North-South Row Orientation

Figure 3.7 shows the schematic of the determination of $\tau$ as a function of wind speed direction for the when the crop row layout is north-south. The boundary conditions are such that when the wind vector direction is parallel to the crop row ($\theta_u$ = $0^o$, $180^o$, or $360^o$), $\tau$ is equal to 0. When the wind crosses the surface perpendicularly to the crop row layout ($\theta_u$ = $90^o$ or $270^o$), $\tau$ assumes a maximum value of 1.

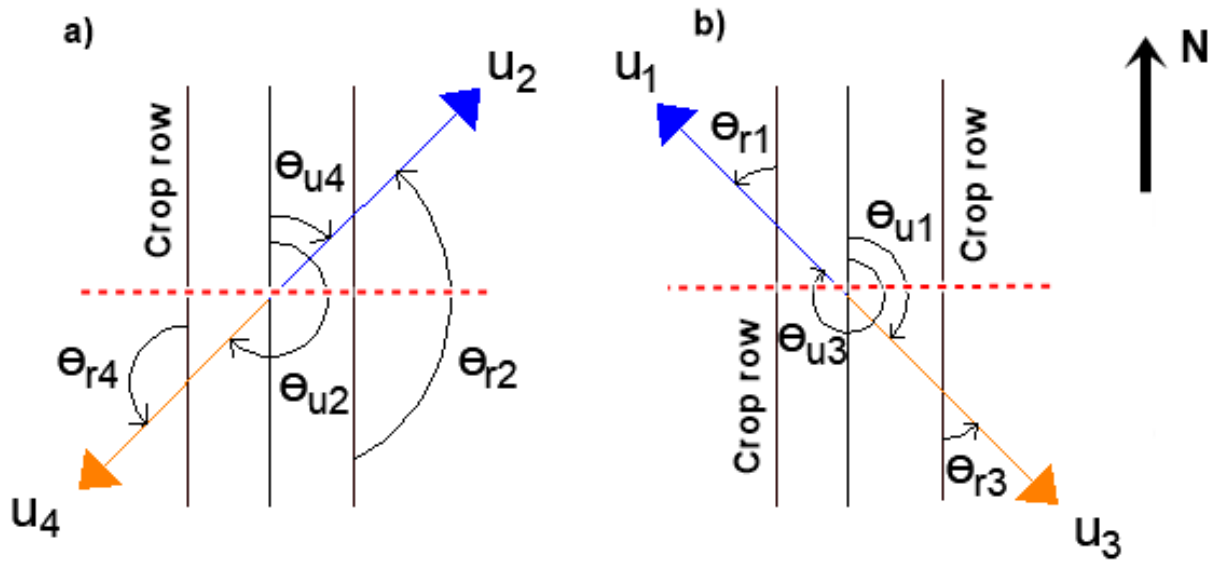


**Figure 3.7:** $\tau$ determination for quadrants 1Q, 2Q, 3Q, and 4Q regarding crop row orientation north-south. Figures 3.7(a) and 3.7(b) indicate $\theta_u$ and $\theta_r$ for, respectively, the 2Q and 4Q and 1Q and 3Q quadrants.

It is assumed that $\tau_1 = \tau_3$ and $\tau_2 = \tau_4$ based on the fact that pair of wind vectors ($u_1$, $u_3$) and ($u_2$, $u_4$) have opposite directions and same $\theta_r$. Therefore, based on trigonometry properties, the following relationships seems to be valid:

$$\theta_{u2} - \theta_{u4} = 180^o \tag{3.46}$$

$$\theta_{r4} = 180^o - \theta_{u4} \tag{3.47}$$

$$\theta_{u3} - \theta_{u1} = 180^o \tag{3.48}$$

$$\theta_{r1} = 180^o - \theta_{u1} \tag{3.49}$$

For quadrant 2Q, $\theta_r > \theta_u$. Thus, $\tau$ for the second quadrant is given by the following expression:

$$\tau_4 = \frac{\theta_{u4}}{\theta_{r4}} = \frac{\theta_{u4}}{180^o - \theta_{u4}}, \quad 0^o \leq \theta_{u4} \leq 90^o \tag{3.50}$$

From equation 3.46:

$$\theta_{u4} = \theta_{u2} - 180^o \tag{3.51}$$

Thus, replacing $\theta_{u4}$ on equation 3.50 by equation 3.51, $\tau$ factor for quadrant 4Q is the following:

$$\tau_2 = \tau_4 = \frac{\theta_{u4}}{180^o - \theta_{u4}} = \frac{(\theta_{u2} - 180^o)}{180^o - (\theta_{u2} - 180^o)} = \frac{\theta_{u2} - 180^o}{360^o - \theta_{u2}}, \quad 180^o < \theta_{u2} \leq 270^o \tag{3.52}$$

For the quadrant 3Q, $\theta_r < \theta_u$. Thus, $\tau$ for the third quadrant is given by the following expression:

$$\tau_1 = \frac{\theta_{r1}}{\theta_{u1}} = \frac{180^o - \theta_{u1}}{\theta_{u1}}, \quad 90^o < \theta_{u1} \leq 180^o \tag{3.53}$$

From equation 3.48:

$$\theta_{u1} = \theta_{u3} - 180^o \tag{3.54}$$

Thus, replacing $\theta_{u1}$ on equation 3.53 by equation 3.54, $\tau$ factor for quadrant 1Q is the following:

$$\tau_3 = \tau_1 = \frac{180^o - \theta_{u1}}{\theta_{u1}} = \frac{180^o - (\theta_{u3} - 180^o)}{(\theta_{u3} - 180^o)} = \frac{360^o - \theta_{u3}}{\theta_{u3} - 180^o}, \quad 270^o < \theta_{u3} \leq 360^o \tag{3.55}$$

Therefore, the $\tau$ factor for the crop row orientation north-south is calculated, as function of a given $\theta_u$, by the equation 3.56:

$$\tau = \begin{cases} \dfrac{\theta_u}{180^o - \theta_u}, & 0^o \leq \theta_u \leq 90^o \\ \dfrac{180^o - \theta_u}{\theta_u}, & 90^o < \theta_u \leq 180^o \\ \dfrac{\theta_u - 180^o}{360^o - \theta_u}, & 180^o < \theta_u \leq 270^o \\ \dfrac{360^o - \theta_u}{\theta_u - 180^o}, & 270^o < \theta_u \leq 360^o \end{cases} \tag{3.56}$$

where $\theta_u$ is the wind speed direction in degrees.

Figure 3.8 shows the $\tau$ plots of equation 3.56 based on the range of wind direction values.

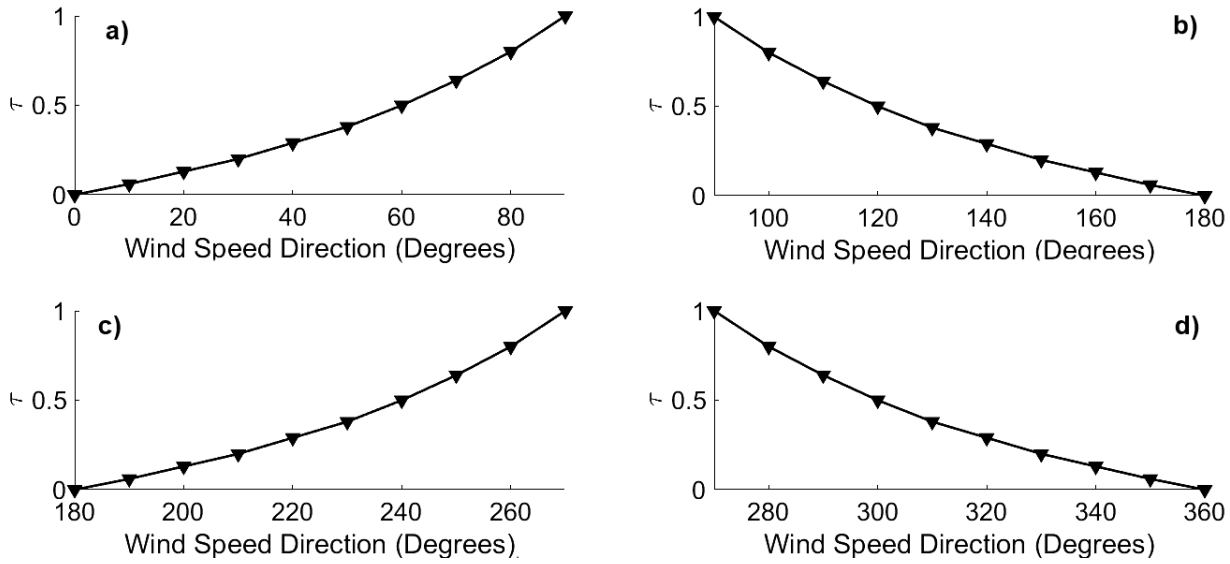


**Figure 3.8:** Graphical representation of the relationship between $\tau$ and $\theta_u$ for the north-south crop layout.

### 3.6.2 Relative Wind Direction Factor for East-West Crop Row Orientation

Figure 3.9 shows the schematic of the determination of $\tau$ as a function of wind speed direction for the when the crop row layout is east-west. The boundary conditions for this scenario are such that when the wind vector direction is parallel to the crop row ($\theta_u$ = 90$^o$ or 270$^o$), $\tau$ is equal to zero. When the wind crosses the surface perpendicularly to the crop row layout ($\theta_u$ = 0$^o$, 180$^o$, or 360$^o$), $\tau$ assumes a maximum value of 1.

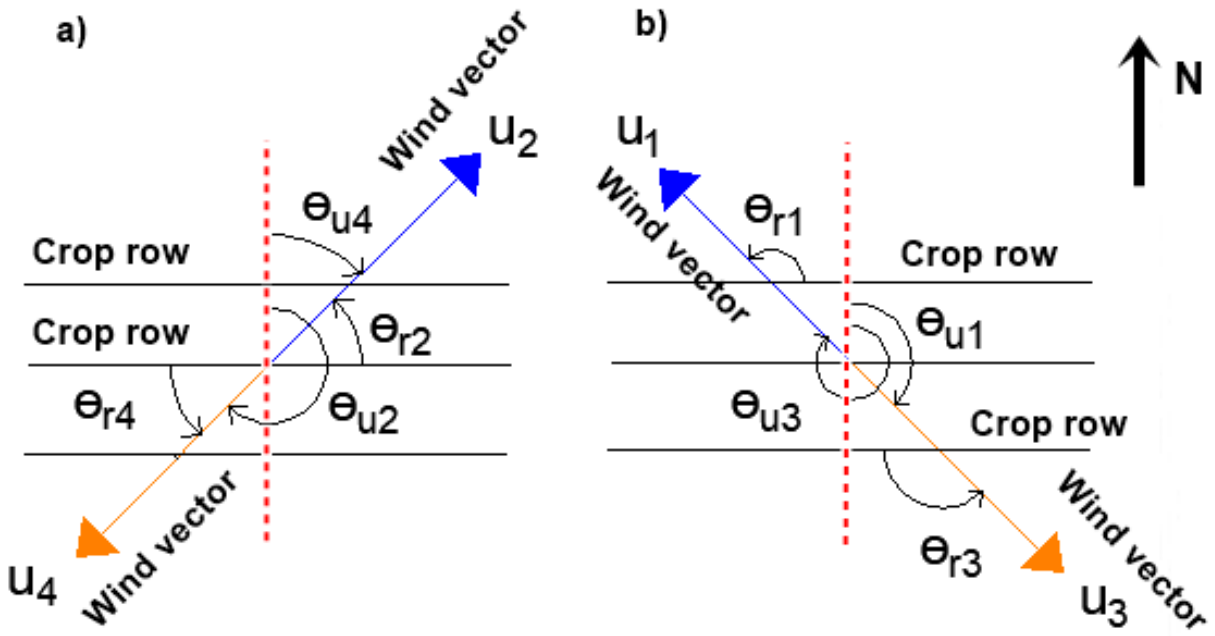


**Figure 3.9:** $\tau$ determination for quadrants 1Q, 2Q, 3Q, and 4Q regarding crop row orientation east-west. Figures 3.9(a) and 3.9(b) indicate $\theta_u$ and $\theta_r$ for, respectively, the 2Q and 4Q and 1Q and 3Q quadrants.

When the crop row is east-west, $\tau$ equations must be adjusted based on the north-south approach to account for the different boundary conditions. An alternative approach is to perform a hypothetical rotation of the fields to the north-south position to obtain mathematical relationships between $\theta_u$ from the original position (east-west) and the equivalent wind direction for the new north-south orientation ($\theta_w$). Figure 3.10 shows the schematic of the rotation approach to estimate

the relative wind direction factor for east-west crop row orientation.

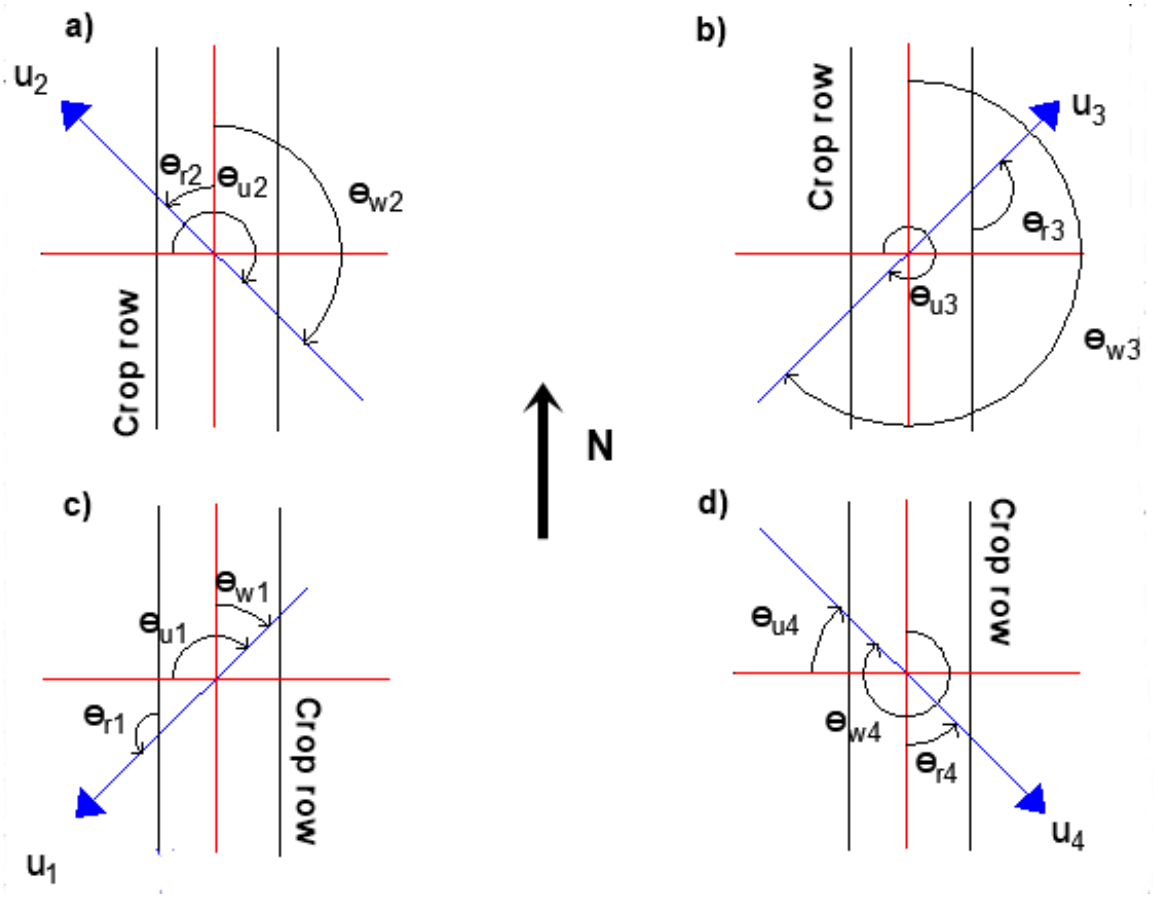


**Figure 3.10:** Rotated quadrants 1Q, 2Q, 3Q, and 4Q from east-west to north-south position. Figures 3.10(a), 3.10(b), 3.10(c), and 3.10(d) indicate $\theta_u$, $\theta_r$, and $\theta_w$ for, respectively, 4Q, 1Q, 3Q, and 2Q quadrants of the original east-west crop row layout.

Table 3.10 presents the summary of expressions for the original east-west and the rotated crop layout wind direction.

**Table 3.10:** Summary of the expressions to relate $\theta_u$ and $\theta_w$ based on figure 3.10.

| East-west quadrant | Figure ID | $\theta_w$ range | $\theta_u$ range | $\theta_w = f(\theta_u)$ | $\tau(\theta_w)$ |
|---|---|---|---|---|---|
| 4Q | Figure 3.9(a) | $90^o < \theta_w \leq 180^o$ | $180^o < \theta_u \leq 270^o$ | $\theta_w = \theta_u - 90^o$ | $\tau = \frac{180^o - \theta_w}{\theta_w}$ |
| 1Q | Figure 3.9(b) | $180^o < \theta_w \leq 270^o$ | $270^o < \theta_u \leq 360^o$ | $\theta_w = \theta_u - 90^o$ | $\tau = \frac{\theta_w - 180^o}{360^o - \theta_w}$ |
| 3Q | Figure 3.9(c) | $0^o \leq \theta_w \leq 90^o$ | $90^o < \theta_u \leq 180^o$ | $\theta_w = \theta_u - 90^o$ | $\tau = \frac{\theta_w}{180^o - \theta_w}$ |
| 2Q | Figure 3.9(d) | $270^o < \theta_w \leq 360^o$ | $0^o \leq \theta_u \leq 90^o$ | $\theta_w = 270^o + \theta_u$ | $\tau = \frac{360^o - \theta_w}{\theta_w - 180^o}$ |

Thus, the development of $\tau$ expressions for each range of $\theta_u$ on east-west original crop row layout is given by the following:

$$\tau_4 = \frac{360^o - \theta_{w4}}{\theta_{w4} - 180^o} = \frac{360^o - (270^o + \theta_{u4})}{(270^o + \theta_{u4}) - 180^o} = \frac{90^o - \theta_{u4}}{90^o + \theta_{u4}}, \;\; 0^o \leq \theta_{u4} \leq 90^o \tag{3.57}$$

$$\tau_1 = \frac{\theta_{w1}}{180^o - \theta_{w1}} = \frac{\theta_{u1} - 90^o}{180^o - (\theta_{u1} - 90^o)} = \frac{\theta_{u1} - 90^o}{270^o - \theta_{u1}}, \;\; 90^o < \theta_{u1} \leq 180^o \tag{3.58}$$

$$\tau_2 = \frac{180^o - \theta_{w2}}{\theta_{w2}} = \frac{180^o - (\theta_{u2} - 90^o)}{(\theta_{u2} - 90^o)} = \frac{270^o - \theta_{u2}}{90^o - \theta_{u2}}, \;\; 180^o < \theta_{u2} \leq 270^o \tag{3.59}$$

$$\tau_3 = \frac{\theta_{w3} - 180^o}{360^o - \theta_{w3}} = \frac{(\theta_{u3} - 90^o) - 180^o}{360^o - (\theta_{u3} - 90^o)} = \frac{\theta_{u3} - 270^o}{450^o - \theta_{u3}}, \;\; 270^o < \theta_{u3} \leq 360^o \tag{3.60}$$

Therefore, the relative wind direction factor for the crop row orientation east-west is calculated, as function of a given $\theta_u$, by the equation 3.61:

$$\tau = \begin{cases} \dfrac{90^o - \theta_u}{90^o + \theta_u}, & 0^o \leq \theta_u \leq 90^o \\ \dfrac{\theta_u - 90^o}{270^o - \theta_u}, & 90^o < \theta_u \leq 180^o \\ \dfrac{270^o - \theta_u}{\theta_u - 90^o}, & 180^o < \theta_u \leq 270^o \\ \dfrac{\theta_u - 270^o}{450^o - \theta_u}, & 270^o < \theta_u \leq 360^o \end{cases} \tag{3.61}$$

Figure 3.11 shows the $\tau$ plots of equation 3.61 based on the range of wind direction values.

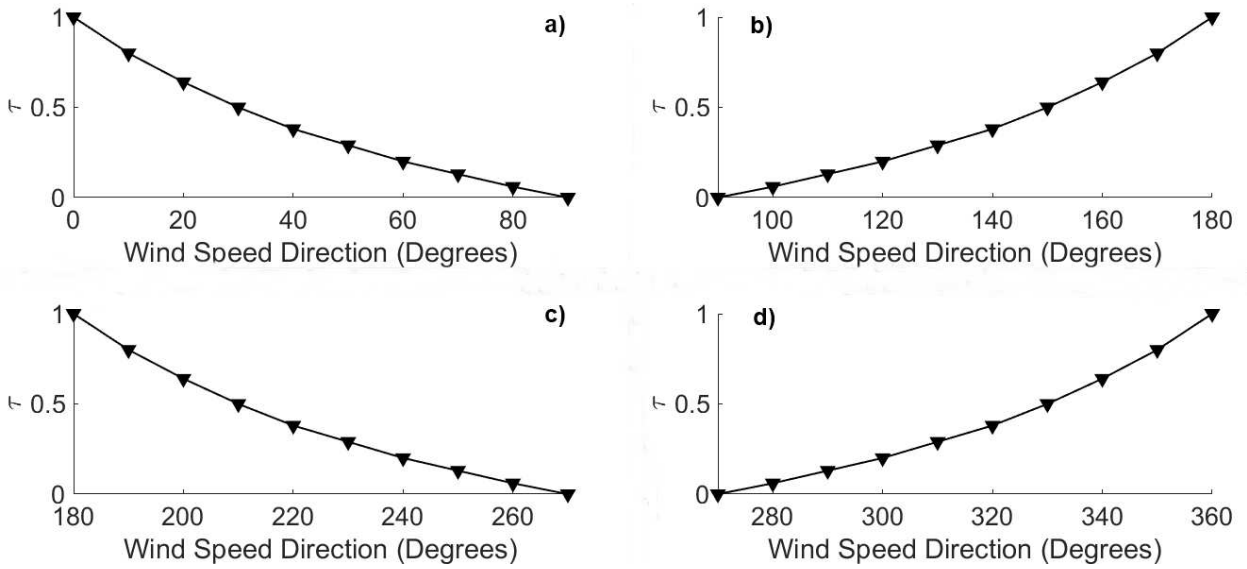


**Figure 3.11:** Graphical representation of the relationship between $\tau$ and $\theta_u$ for the east-west crop layout.

## 3.7 Measurements of Surface Heat Fluxes at LIRF

The experiment was designed for acquisition of all data needed for modeling and measuring all components of the surface energy balance in order to provide reliable information for assessing the modeling for $T_o$ and sensible heat flux. Net radiation and soil heat flux were measured in two different locations at north and middle sections in each field that accounted for similarities in biomass conditions to minimize the introduction of bias into the measurements by incorporating surface heterogeneity within the measured data.

### 3.7.1 Net Radiation Measurements

Two net radiometers per field were installed to measure $R_n$ at a height of 3.3 m above ground surface. Three $R_n$ sensors were two-way net radiometers that provide the net long-wave and net short-wave radiation terms. A four-way net radiometer (figure 3.12) was installed in the middle of field 2 during both years and measured all the four components of the radiation budget (incoming short-wave radiation, reflected short-wave radiation, incoming long-wave radiation from nearby atmosphere, and emitted long-wave radiation from the surface). The four-way net radiometer provided data for the fully irrigated treatment in 2017 and deficit irrigated treatment in 2018. For both fields, the measurements of $R_n$ were stored every minute and averaged every 15 minutes. The measurements from each point measurement per field were averaged to provide a more representative data that could be assumed for the entire field.

**Figure 3.12:** 4-Way net radiometer installed at LIRF in 2017 and 2018.

### 3.7.2 Soil Heat Flux Measurement

Soil heat flux at the surface level (G) was measured following the soil heat flux plate method (SHFP), in which consists on installing small sensor plates of known heat conductivity to measure the transfer of heat at a fixed depth within the root zone and accounting for the heat storage capacity of the soil layer between the sensor plate and ground surface (figure 3.13). Two identical plates (figure 3.14) were buried per station per field on both years, being one below the corn row and another in the inter row. Following the same approach for the net radiation data acquisition, recordings of soil heat flux plates were stored every minute and averaged every 15 minutes. For obtaining representative G values for each field in their total extension, measured G from all stations per field were averaged.

The determination of measured G was calculated following the approach reported by Ochsner et al. (2006) and indicated by equation 3.62:

$$G = G_p + S \tag{3.62}$$

where $G_p$ is the soil heat flux measured by the plate ($W/m^2$) and S is the storage heat term of the soil layer immediately above the plate and below ground surface ($W/m^2$).

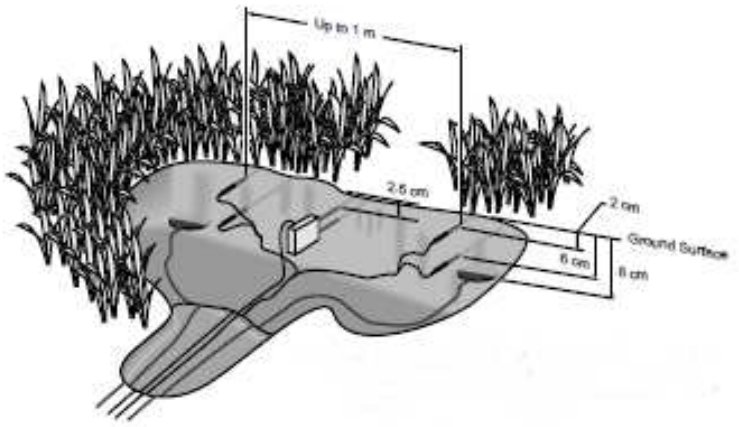


**Figure 3.13:** Schematic of the soil heat flux sensors installation (Campbell Scientific, 2003).

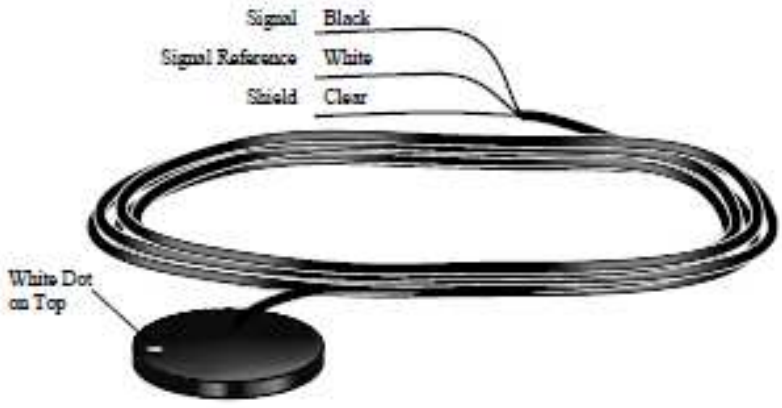


**Figure 3.14:** Soil heat flux plate installed on the fields on both underneath corn row and on the inter-row (Campbell Scientific, 2003).

Soil heat storage is a function of the gradient of soil temperature within the profile, heat capacity of the soil, and the thickness of the layer. Equation 3.63 represents that formulation as:

$$S = \frac{\Delta T_s \cdot C_s \cdot d_z}{t} \tag{3.63}$$

where $\Delta T_s$ is the change on soil temperature at two different depths above the plate's location (°C); $C_s$ is the heat capacity of moist soil (J/Kg/K); $d_z$ is the depth where the soil heat flux plates were buried (m), and t is the time interval between the readings of soil temperature (s).

The heat capacity of moist soils is a function of the mineral properties and soil water content and water properties. As water flows in three dimensions within the root zone, it carries heat that must be accounted for when determining the soil heat storage. Equation 3.64 indicates the general approach to calculate the storage of heat on the soil.

$$C_s = \rho_b \cdot (C_d + \theta_v \cdot \rho_w \cdot C_w) \tag{3.64}$$

where $\rho_b$ is the soil bulk density ($Kg/m^3$); $C_d$ refers to the heat capacity of soil minerals and it is often taken as 840 J/Kg/K (Hanks and Ashcroft, 1980); $\theta_v$ is the volumetric soil water content ($m^3/m^3$), and $C_w$ is the water heat capacity (J/Kg/K).

The soil heat flux plates were buried at a depth of 8 cm below ground surface and soil temperature was measured at 2 cm and 6 cm below ground. Soil water content readings on the 8 cm soil layer were done by using a capacitance based soil water content sensor at a depth of 4 cm. The installation of soil heat flux plates was done for all stations and it included underneath corn row and inter row measurements. Thus, a total of 4 soil heat flux plates, 4 soil water content sensors at shallow depth, and 8 soil temperature probes per field were installed to provide all data needed for measuring soil heat flux at the surface level for both different irrigation water management

practices.

As indicated by Varble and Chavez (2011), capacitance based soil water content sensors are very sensitive to salinity and soil temperature and are often needed to have their final output data calibrated by more accurate methods for determining soil water content. For the shallow depth measurements of water in the root zone, the calibration of the soil water content data was performed through a linear regression model based on data from time domain reflectometer (TDR). The calibration followed the general linear model indicated by equation 3.65:

$$\theta_{TDR} = \hat{\beta}_1 \cdot \theta_{5TE} + \hat{\beta}_2 \tag{3.65}$$

where $\theta_{TDR}$ is the volumetric soil water content obtained from the TDR readings at 15 cm below ground surface ($m^3/m^3$); $\theta_{5TE}$ is the shallow (4 cm) volumetric water content measured using the capacitance based sensor ($m^3/m^3$); $\hat{\beta}_1$ and $\hat{\beta}_2$ are linear fitted coefficients for the calibration equation.

TDR readings were done once a week in 2017 in both fields, always before a irrigation event to consider the period when the root zone profile was being dried up through the plants and evaporation from the top soil surface. In 2018, the same approach for measuring water content using the TDR was followed. However, the number of measurements were before and after irrigation events to provide more data for the calibration. Calibration of soil water content was done at each station for each year individually to provide better adjustment due to the fact that the installation of the stations were not at the same location in both years. Since the capacitance-based sensors provided data continuously every 15 minutes, the pair of points for the development of the soil water content calibration equation were selected considering the data from the 5TE capacitance based sensor and the TDR measurement at the same day and about the time.

### 3.7.3 Sensible Heat Flux Measurements - Bowen Ratio Method

The Bowen ratio method (BR) provides estimates of H and LE based on the ratio between those two surface heat fluxes. The method has been researched, improved, and considered well accepted as a reliable way to estimate sensible and latent heat fluxes at the surface level (Perez et al., 1999; Comunian et al., 2018; Buttar et al., 2018). Equation 3.66 indicates the basic approach of the BR approach:

$$\beta_o = \frac{H}{LE} \tag{3.66}$$

where $\beta_o$ is the Bowen ratio (dimensionless).

Perez et al. (1999) explain that a meaningful determination of surface heat fluxes based on the Bowen ratio method depends on providing accurate values of $\beta_o$ in order to minimize the spread of bias that is accumulated when errors from the measurements of $R_n$ and $G$ are also taken into account.

Arya (2001) indicates that the $\beta_o$ might be calculated as an approximation of the ratio characterized by the gradients of heat and vapor when the assumption that the coefficients of heat and vapor transfer are the same in magnitude is valid. Equation 3.67 shows the algebraic representation of that assumption.

$$\beta_o \cong \frac{Cp_a \cdot K_h \cdot \Delta T}{\lambda \cdot K_v \cdot \Delta e} = \left(\frac{Cp_a}{\lambda}\right) \cdot \left(\frac{\Delta T}{\Delta e}\right) \tag{3.67}$$

where $Cp_a$ is the specific heat of air (J/Kg/K); $K_h$ and $K_v$ are, respectively, the diffusivity coefficients for heat and vapor transfer ($m^2/s$); $\lambda$ is the latent heat of vaporization of water (J/Kg/K); $\Delta T$ and $\Delta e$ are, respectively, the temperature (°C) and actual vapor pressure (kPa) difference be-

tween data at two different heights.

As indicated by ASCE-EWRI (2005), the ratio $\frac{Cp_a}{\lambda}$ is often expressed as the psychometric constant ($\gamma$) and calculated as a function of local atmospheric pressure, as indicated by equation 3.68:

$$\gamma = \frac{Cp_a}{\lambda} = 0.000665 \cdot P_a \tag{3.68}$$

where $P_a$ is the local atmospheric pressure (kPa). $\gamma$ has units of $kPa/C$.

$P_a$ might be calculated as indicated by ASCE-EWRI (2005) as a function of local ground elevation:

$$P_a = 101.3 \cdot \left( \frac{293 - 0.0065 \cdot Z_g}{293} \right)^{5.256} \tag{3.69}$$

where $Z_g$ is the local ground elevation (m).

The calculation of actual vapor pressure from each height of measurement was done as indicated by equation 3.70:

$$e_a = RH \cdot e_s \tag{3.70}$$

where $e_a$ is the actual vapor pressure (kPa); RH is the relative humidity (dimensionless); $e_s$ refers to the saturation vapor pressure (kPa).

$e_s$ was calculated using the approach developed by Buck (1981), as shown on equation 3.71:

$$e_s = 0.61121 \cdot exp\left( \frac{17.502 \cdot T_a}{T_a + 240.97} \right) \tag{3.71}$$

where $T_a$ is given in (°C).

For LIRF fields, the change in air temperature and actual vapor pressure were obtained from measurements of $T_a$ and relative humidity at two different heights. For the year of 2017, the heights selected were at 2.7 m and 3.7 m above ground surface. For the year of 2018, the heights that provided data for the Bowen ratio calculation of sensible heat flux were located at 2.6 m and 3.2 m above ground surface for field 1 and at 2.6 m and 4.2 m for field 2. Those data were obtained from the aerodynamic flux towers located at the north side of both fields 1 and 2 on both years (figure 3.15). Sensible heat flux values were obtained by solving equation 3.66 for H and replacing LE as the residual of the surface energy balance equation, as indicated by equations 3.72 to 3.75:

$$H_{BR} = LE \cdot \beta_o = (R_n - G - H_{BR}) \cdot \beta_o = (R_n - G) \cdot \beta_o - H_{BR} \cdot \beta_o \tag{3.72}$$

Keeping only the term $(R_n - G) \cdot \beta_o$ on the last equality of equation 3.72:

$$H_{BR} + H_{BR} \cdot \beta_o = (R_n - G) \cdot \beta_o \tag{3.73}$$

Rewriting the left hand side of the equation 3.73 in terms of $H_{BR}$:

$$H_{BR} \cdot (1 + \beta_o) = (R_n - G) \cdot \beta_o \tag{3.74}$$

Dividing all sides of equation 3.73 by $(1 + \beta_o)$:

$$H_{BR} = \left( \frac{\beta_o}{1 + \beta_o} \right) \cdot (R_n - G) \tag{3.75}$$

where $R_n$ and G are given in $W/m^2$ units.

Perez et al. (1999) recommend that the values of H obtained from the Bowen ratio method must be coherent regarding the symbols and assumptions proposed. Values of $\beta_o$ that are not con-

sistent with the measured data must not be used into the calculation of H, since it will add bias to the determination of surface heat fluxes. For this study, negative values of $\beta_o$ were not included on the calculation of H for daytime conditions, in which $R_n$ is assumed positive towards the surface.

### 3.7.4 Sensible Heat Flux Measurements - Aerodynamic Profile or Gradient Method

The aerodynamic method (AERO) consists on calculating sensible heat and latent heat fluxes based on the relationship between those energy density fluxes and atmospheric variables that allow H and LE to take place within the atmospheric boundary layer (Prueger and Kuskas, 2005).

Sensible heat flux might be calculated as following:

$$H_{AERO} = -\rho_a \cdot Cp_a \cdot u_{aero} \cdot T_{aero} \tag{3.76}$$

where $u_{aero}$ and $T_{aero}$ are, respectively, scaling factors for friction velocity and temperature.

The scaling factors for friction velocity and temperature are calculated, respectively, by equations 3.77 and 3.78:

$$u_{aero} = \frac{k}{\alpha_u} \tag{3.77}$$

$$T_{aero} = \frac{k}{\alpha_t} \tag{3.78}$$

where $\alpha_u$ and $\alpha_t$ are, respectively, the slopes of the line obtained when plotting $ln(Z_m) - \psi_m(Z_m/L_{MO})$ vs. $u$ and $ln(Z_m) - \psi_h(Z_m/L_{MO})$ vs. $T_m$, where $T_m$ is the air temperature measured at height $Z_m$.

The weather data needed for obtaining H from the aerodynamic method was $T_a$ and wind speed at four different heights on each field. The data points for establishing the linear regression were considered to be the averaged values between two consecutive heights. Therefore, the weather data was averaged for the section represented by the four heights of the aerodynamic flux towers: $h_1$ to $h_2$, $h_2$ to $h_3$, and $h_3$ to $h_4$, where $h_1 < h_2 < h_3 < h_4$. In 2017, the weather data needed were from at the following heights: 1.5 m, 2.7 m, 3.3m, and 3.7 m above ground surface. In 2018, the heights at which the data were collected were at 1.5 m, 2.6 m, 3.2 m, and 4.2 m. Data from all heights were recorded every 15 minutes as an average of 1 minute data for every quarter hour.

The friction velocity and Monin-Obukhov atmospheric stability length values regarding the calculation of the sensible heat from the AERO approach were obtained from the LAS output data instead of being calculated. The calculation of the stability correction factors for momentum transfer were done based on the work of Yasuda (1988) and presented by equations 3.29 to 3.37.

**Figure 3.15:** Aerodynamic flux tower with the eddy covariance system in 2017 on the field 2.

### 3.7.5 Sensible Heat Flux Measurements - Eddy Covariance System

Eddy covariance (EC) measurements of sensible heat were performed for a short period of time in 2017 on the fully irrigated treatment plot only. The data from EC measurements were obtained from July to September. Correction for wind coordinate rotation were performed, as described in Kaimal and Finnigan (1994), and Tanner and Thurtell (1969). Lag time issues caused by data-loggers were corrected by estimating each averaging interval through a cross correlation analysis between the scalar of interest and the vertical wind component. Then, comparing the correlations between the two signals lagged by different delays. The time lag that is selected is those that produces the highest correlation. Latent heat flux measurements from the krypton hygrometer were corrected for oxygen and Webb et al. (1980) term.

Two measurements of H were provided by the EC station: one being the corrected sensible heat flux ($EC_c$) based on sensible heat flux from the sonic anemometer based air temperature ($EC_s$) and corrected latent heat flux. Values of H were provided as averaged 15 minute data from high frequency 20 Hz measurements. The eddy covariance system was installed on the north side of field 2, 3.5 m above ground surface at an azimuth angle of $135^o$.

### 3.7.6 Sensible Heat Flux Measurements - Large Aperture Scintillometers (LAS)

The propagation of a beam of light through the air is often attenuated causing a reduction of the near infra-red light signal intensity from which it was originated. The changes on the beam of electromagnetic waves crossing a given surface preferentially on a horizontal trajectory are indicated as scintillations and they are related to the air property referred to as the refractive index of the air ($C_n^2$). Therefore, sensors to measure those changes in $C_n^2$ are capable of providing quantitative information regarding the distortions on the signal caused by the sensible heat flux interference on the refractive properties of the air as the vertical transfer of heat crosses the trajectory of the signal of the beam of photons (Kipp and Zonen, 2007).

The $C_n^2$, crucial variable for providing the information needed to characterize the external influences on the disturbances of the propagation of electromagnetic waves across a surface is calculated as indicated by Wang et al. (1978) and shown by equation 3.79:

$$C_n^2 = 1.12 \cdot \sigma_{lnI}^2 \cdot D^{7/3} \cdot L^{-3} \tag{3.79}$$

where D is the aperture diameter of the emitter and receiver sensors (m); L refers to the path length as the distance between the transmitter and the receiver (m); $\sigma_{lnI}^2$ is the statistical variance of the natural logarithm of the intensity variations.

The calculation of measured H using the scintillometer's approach is based on equation 3.80:

$$H_{LAS} = -\rho_a \cdot Cp_a \cdot u_* \cdot T_* \tag{3.80}$$

where $T_*$ is the LAS temperature scaling factor.

The determination of the $T_*$ incorporates the scintillation approach of measuring $C_n^2$. Therefore, $T_*$ is calculated following the approach of Wyngaard et al. (1971):

$$T_* = \sqrt{\frac{C_T^2 \cdot (Z_{LAS} - d)^{2/3}}{f_T \cdot \left(\frac{Z_{LAS} - d}{L_{MO}}\right)}} \tag{3.81}$$

where $C_T$ refers to the structure parameter of air temperature, $Z_{LAS}$ is the height of the scintillometer when the ground surface is taken as the datum reference (m); $f_T$ is the universal stability function.

The $C_T$ term is determined by equation 3.82 developed by Wesely (1976):

$$C_T^2 \approx C_n^2 \cdot \left(\frac{-0.78 \cdot 10^{-6} \cdot P_a}{T_a^2}\right)^{-2} \cdot \left(1 + \frac{0.03}{\beta_o}\right)^{-2} \tag{3.82}$$

The $f_T$ stability correction is calculated by using the equation 3.83 and published by De Bruin et al. (1993):

$$f_T = 4.9 \cdot \left(1 - c_o \cdot \frac{Z_{LAS} - d}{L_{MO}}\right)^{-2/3} \cdot \left(\frac{Z_{LAS} - d}{L_{MO}}\right)^{-1} \tag{3.83}$$

where $c_o$ is a constant adjustment factor for unstable ($c_o = 6.1$) or stable ($c_o = 2.2$) atmospheric conditions determined by the Monin-Obukhov atmospheric stability length.

For this study, one set of LAS sensors (transmitter and receiver) was installed in each field during both years of data collection. Figure 3.16 shows one of the emitters installed for the measurements. The sensors were positioned facing each other on a angle to account for the main wind direction above the fields. In 2017 the height of the sensors were 3.6 m above ground surface for the fully irrigated plot and 2.8 m for the deficit irrigated treatment, The LAS transmitter and receiver separation distance was 167 m. In 2018, the effective height was 3.8 m above ground for the fully irrigated field and 3 m for the deficit irrigated plot. The distance between the LAS receiver and transmitter sensors was 163 m.

The calculations of measured H using the LAS approach were done using the software WINLAS 2007 version 2.2. The software has the capability of calculating all the steps needed to obtain H from the $C_n^2$, sensor's layout, and on-site weather data such as air temperature, wind speed, and relative humidity.

The weather data provided to obtain H were from the aerodynamic flux towers located in each field. In 2017, the data used were originated from a height of 3.7 m above ground surface. In 2018, air temperature, wind speed and relative humidity data were obtained from 4.2 m above ground surface and used for calculating H from LAS. The differences in height from 2017 to 2018 calculations were needed to consider measurements of wind speed and air temperature would be at similar height to the beam of light trajectory from the LAS sensors and also due to the different set up of the towers between both years.

Measured H from LAS and also EC were filtered for wind speed directions. The filtering data process considered certain range of wind direction to avoid heat transfer interference from the

roads and nearby research site areas with different surface type (figure 3.17). EC and LAS methods account for measuring H over an area, instead of a point-source measurement, in which the filtering for wind speed might provide data for when air crosses the fields through a longer trajectory to better represent sensible heat flux over the fields studied (figure 3.18). Only wind speed direction varying from $125^o$ to $165^o$ and $285^o$ to $325^o$ were considered to the modeling and assessment of the research results regarding LIRF data on both 2017 and 2018 years.

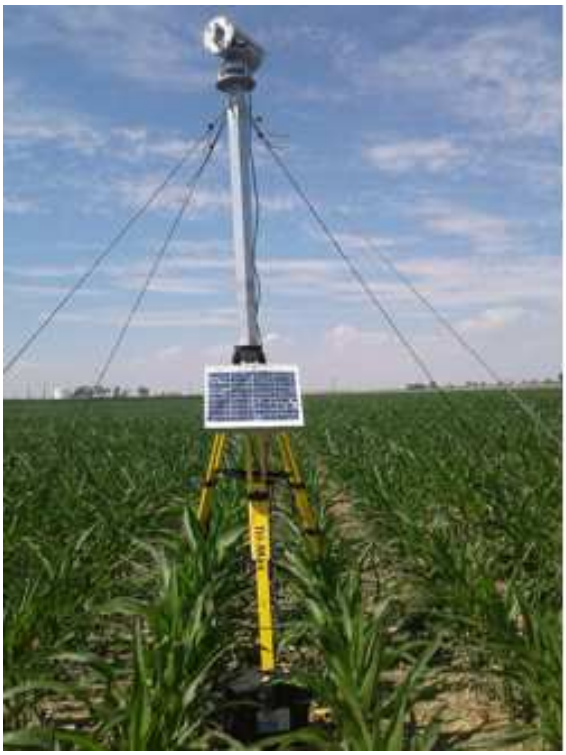

**Figure 3.16:** LAS Emitter.

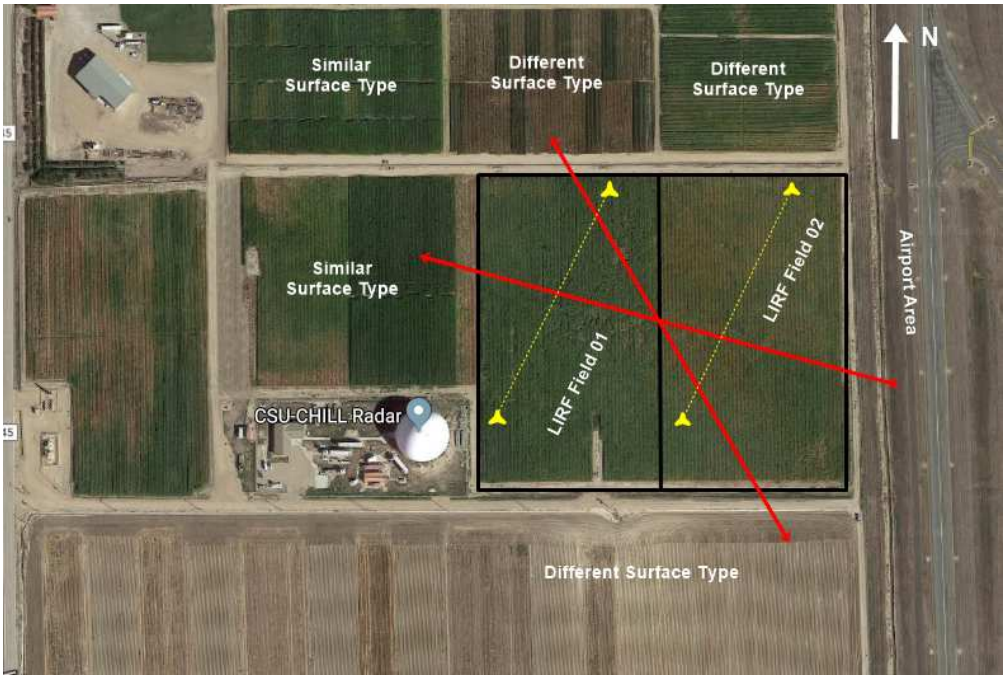


**Figure 3.17:** Layout of the surroundings of LIRF fields.The area in between the red lines are the desirable range of wind direction based on wind patterns and location of the LAS sensors (yellow triangles). That was chosen to avoid interference from the wind that would flow above plots that are had different surface types.

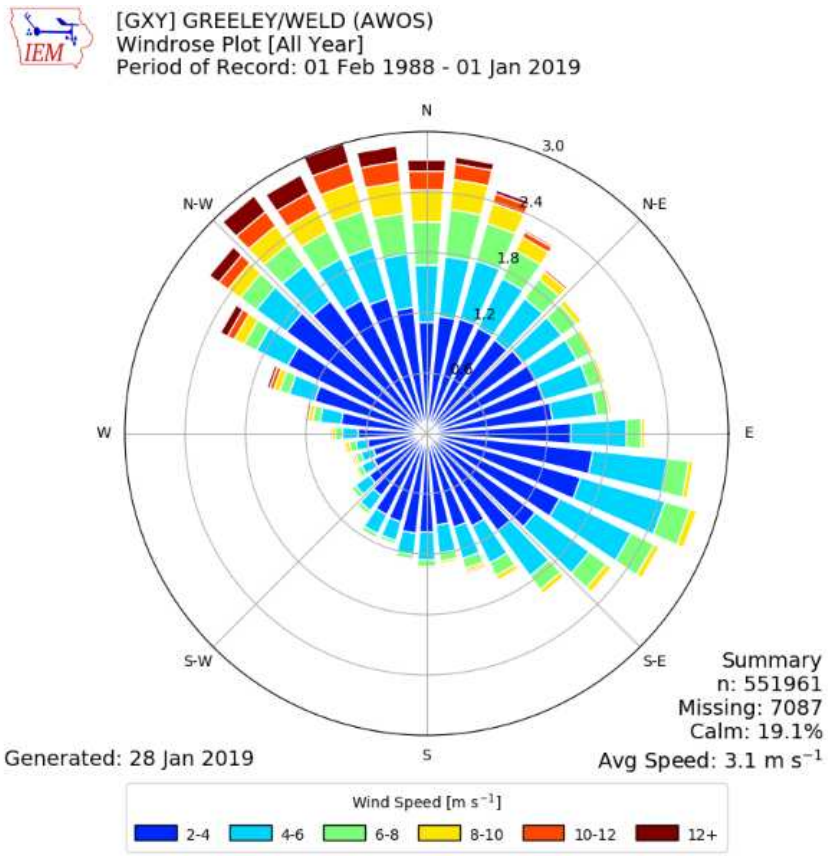


**Figure 3.18:** Wind speed patterns for Greeley (CO) area 1988-2019.

## 3.8 Statistical Analysis of Measured H

A multiple pairwise test statistic comparison analysis was performed to assess difference in population means between the measured sensible heat data from the different methods in order to evaluate sensible heat models with an extra data set of measured H besides the sensible heat flux from LAS that is the reference data for modeling $T_o$. Only daytime data under unstable atmospheric conditions ($H > 0$) were used on the analysis, which it was assumed to be when $R_n > 0$ and $L_{MO} < 0$.

### 3.8.1 Kruskal-Wallis Statistical Test for Inference on Difference in Means

The non-parametric test for difference in population means Kruskal-Wallis (KW), named after the work of Kruskal and Wallis (1952) was initially applied to identify overall differences among groups, as indicated by the equation 3.84:

$$TS = \frac{12}{N_T \cdot (N_T + 1)} \cdot \sum \left[ \frac{T_i^2}{N_i} - 3(N_T + 1) \right] \tag{3.84}$$

where TS denotes the test statistic variable; $N_i$ is the number of observations from a given sample "i"; $N_T$ is the total sample size; $T_i$ is the sum of the ranks for the data from a given sample "i" after combining.

The null ($H_o$) and the alternative ($H_A$) hypothesis for the Kruskal-Wallis test is the following:

$H_o$: The distribution of all the variables sampled are the same.

$H_A$: At least one population mean is different than the others.

According to Otto and Longnecker (2001), the non-parametric test as an alternative method for an analysis of variance (ANOVA) is recommended when the assumption of the normality of residuals is often violated. ANOVA tests are very sensitive to samples that provide linear model residuals that do not follow a gaussian probability distribution function. Thus, the non-parametric test by Kruskal and Wallis (1952) was chosen to avoid dealing with normality of the residuals of the linear model that is the premise of the analysis of variance method.

The KW test does not provide comparison among groups, but serve as an indicator to statistically identify if there are proof that differences among groups of the analysis are pertinent to the evaluation. A multiple pairwise comparison between pair of groups is required to assess the differences within the groups.

### 3.8.2 Non-Parametric Test for Multiple Pairwise Comparison

The pairwise multiple comparison test for non-parametric KW statistical method, developed by Dunn (1964), was performed to do, initially, a pairwise comparison analysis among the measured H data to identify those that are statistically the same. Dunn (1964) developed a test for multiple comparison among groups when the assumption that the cumulative density function of a given variable is independent and unique in regards the other variable in which the comparison is being performed. For a given number of variables (n), Dunn's test has the capability to provide a total number of k(k-1)/2 pairwise comparisons that rely on the approximations of Dunn's test statistic term. The test was chosen due to the fact that it is a non-parametric approach that provides pairwise comparisons analysis when the assumption of the normality of residuals is often violated. All statistical analysis were done assuming a level of confidence ($\alpha$) equals to 0.05. For an analysis that is statistically homogeneous, all samples were kept at the same size, since test-statistics are fundamentally dependent on the sample size.

The p-values were corrected for multiple pairwise comparisons using the approach developed by Sidak (1967). The correction of p-values was done by following equation 3.85:

$$p_a = max[1, 1 - (1 - p)^m] \tag{3.85}$$

where m is the total number of pairwise comparisons from Dunn's test; $p_a$ is the adjusted p-value; p is the non-adjusted p-value from Dunn's test.

The adjustment of p-values when performing a multiple pairwise comparison is justified by the fact that large number of variables compared to each other increase the chances of rejecting the null hypothesis when that is true (Ott and Longnecker, 2001).

The test was performed, then, to compare the measured sensible heat from BR, LAS, EC, and AERO methods and identify those in which the population of measured values might be consid-

ered statistically the same. The population of measured H is considered to be all 15 minute data throughout the entire growing season during daytime conditions and under unstable atmospheric conditions.

The pairwise comparison of those which p-values were less than 0.025 were ignored from the analysis, since p-values less than 0.025 shows strong statistical evidence that the sensible heat population means are not the same (Dunn, 1964).

## 3.9 Statistical Analysis for Model Quality Assessment

To assess the quality of the models developed, the mean bias error (MBE), root mean square error (RMSE), and the refined index of agreement ($d_r$) were considered to make an investigation about how the models for $T_o$ and H are performing well during different scenarios. The MBE and RMSE equations are specified by equations 3.86 and 3.87, respectively:

$$MBE = \frac{\sum(E_i - O_i)}{n} \tag{3.86}$$

$$RMSE = \sqrt{\frac{\sum(E_i - O_i)^2}{n}} \tag{3.87}$$

where $E_i$ and $O_i$ are referring to, respectively, the estimated and observed or measured values, and n is the sample size analyzed.

RMSE is a statistical term that indicates the spread of errors of a given model is occurring for a given data set analyzed (Chai and Draxler, 2014). Smaller RMSE values mean that the model providing good results when reporting values that are compared with observed data. The MBE is a measure of identifying the capability of the model to overestimate or underestimate predicted

values, which is indicated by positive or negative values, respectively.

The modified index of agreement was developed by Willmott et al. (2012) as an attempt to improve the initial approach introduced by Willmott (1981) and it is indicated by equation 3.88:

$$d_r = \begin{cases} 1 - \dfrac{\sum |E_i - O_i|}{2 \cdot \sum |O_i - \bar{O}|}, & \sum |E_i - O_i| \leq 2 \cdot \sum |O_i - \bar{O}| \\ \dfrac{2 \cdot \sum |O_i - \bar{O}|}{\sum |E_i - O_i|} - 1, & \sum |E_i - O_i| > 2 \cdot \sum |O_i - \bar{O}| \end{cases} \tag{3.88}$$

The refined $d_r$ statistical term aims to minimize the issues caused by the Willmott (1981) approach that seems to be very sensitive to a data set that has statistical outliers or extreme data values that add bias into the analysis of the model performance based on the Index of Agreement (Legates and McCabe, 1999).

The interpretation of the $d_r$ term is related to the assessment of how a given model with its spread of errors and imperfections is far away or close to the performance of a completely unbiased model that perfectly represents the nature of the processes that generate the observed values. Values of $d_r$ may vary from -1 to 1, being +1 the condition to identify a model as a true measured of a given observed process. As $d_r$ approaches towards -1, the given model is likely to have less results variability, although having unsatisfied performance (Willmott et al., 2012).

## 3.10 Data for Assessing $T_o$ and H Model Quality Results

### 3.10.1 The Iowa Soil Moisture Experiment (SMEX02)

SMEX02 experiment was located in Aimes, Iowa at latitude of 42 ° 01' N, longitude of 93 ° 44' W, and elevation of 327 m during the data collection campaign of 2002 (Anderson et al., 2004, Chavez et al., 2005, and Chavez and Lopez-Urrea, 2018). The experiment was developed through a partnership among several institutions, including Texas AM University, USDA-ARS, University of Iowa, Utah State University, Duke University, and Los Alamos National Laboratory. A total of 31 fields at the Walnut Creek Watershed south of Aimes were monitored throughout the rapid growth stage for mapping surface heat fluxes and soil water content using remote sensing techniques. Figure 3.19 shows the location of the fields and their surface type. Yellow regions indicate soybean fields while the green fields are corn.

The climate conditions during summer season might be characterized as humid continental climate. Precipitation is well distributed along the year. Koppen climate classification for that area is Dfa, which stands for hot summer continental climate. Average air temperature during the warmest month (July) is 23 °C, and average rainfall water depth during the wettest month (June) is 127 mm.

Data measurements on SMEX02 experiment consisted on all components of the surface energy balance ($R_n$, G, H, and LE), remote sensing variables ($T_s$, reflectance data) and weather data ($T_a$, wind speed, wind direction, and relative humidity), and soil properties (soil temperature and soil water content). Measurements of sensible and latent heat fluxes were done using eddy covariance systems, installed on each field facing south due to predominant wind direction coming from south and southwest. Net radiation and soil heat flux measurements were obtained with, respectively, net radiometers and soil heat flux plates installed on site. Soil thermocouples were installed at depths of 2 cm and 4 cm below surface and soil heat flux plates were buried at a depth of 6 cm below ground surface. Surface temperature was obtained through IRT's that were installed at NADIR view position facing downwards. EC 3D wind speed and water vapor concentration data were

averaged every 30 minutes based on high frequency 20 Hz data collection from June 20 to July 9 in 2002. Air temperature and humidity data were measured using air temperature and relative humidity sensors at a height in between 2 to 3 m above ground surface.

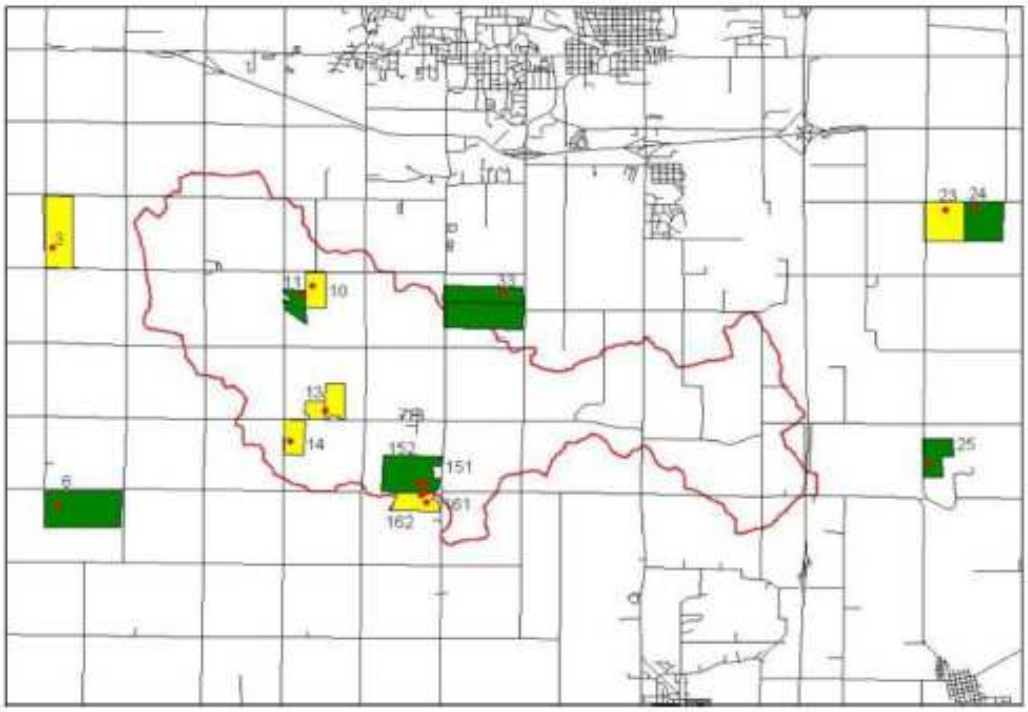


**Figure 3.19:** SMEX02 field locations. The yellow areas are soybeans and green areas indicate corn fields (Chavez and Lopez-Urrea, 2018).

The data from fields WC06, WC 15.1, and WC24 were used on this analysis. All fields are rainfed corn based and the data set were combined in one group of data for the analysis. Table 3.11 shows the coordinates of the field and information about the crop layout.

Surface reflectance data were collected on three dates in 2002 (June 16, July 1, and July 8) after calibrating raw multispectral airborne images of the fields. Calculation of NDVI and OSAVI were performed for those dates and later interpolated as a function of DOY, for each field, as indicated by the general model on equation 3.89:

$$VI = \hat{\alpha}_1 \cdot ln(DOY) + \hat{\alpha}_2 \tag{3.89}$$

where VI represents either NDVI or OSAVI.

Table 3.12 shows the coefficients of the interpolation equations for NDVI and OSAVI regarding SMEX02 data.

Air temperature, wind speed, and wind direction were obtained from the EC stations on each field. Inverted $T_o$ and $r_{ah}$ were calculated based on the same approach applied for LIRF data. The aerodynamic resistance was calculated using the friction velocity from EC measurements. Monin-Obukhov atmospheric stability length was calculated as indicated by Monin and Obukhov (1954) and the roughness canopy elements were determined based on the work of Brutsaert (1982). Filtered wind speed conditions were applied on the data set to account for the predominant wind direction of coming from southwest and south of the fields. Only unstable atmospheric conditions and daytime data were used on the analysis of $T_o$ and H. Surface energy balance closure and non-closure methods were also applied to the measured sensible heat flux, which provided two analysis of model's performance. The closure procedure performed is based on Bowen ratio approach and it was done by following the methodology described by Twine et al. (2000) and applied by Chavez et al. (2005) on SMEX02 EC data set.

**Table 3.11:** Summary of information about the fields WC06, WC15.1, and WC24 on SMEX02 experiment.

| Field ID | Crop | Row Direction | Row Spacing | Latitude | Longitude |
|---|---|---|---|---|---|
| [-] | [-] | [-] | [cm] | [Deg] | [Deg] |
| WC06 | Corn | North to South | 76 | 41.93289579 | -93.75331502 |
| WC15.1 | Corn | East to West | 76 | 41.93781824 | -93.6631318 |
| WC24 | Corn | North to South | 76 | 41.99291298 | -93.52857874 |

**Table 3.12:** Interpolation equations for NDVI and OSAVI for SMEX02.

| Field ID | Variable | $\hat{\alpha_1}$ | $\hat{\alpha_2}$ | $R^2$ |
|---|---|---|---|---|
| [-] | [-] | [-] | [-] | [-] |
| WC06 | NDVI | 3.0994 | -15.442 | 0.99 |
| | OSAVI | 2.8391 | -14.187 | 0.99 |
| WC15.1 | NDVI | 3.5939 | -17.911 | 0.93 |
| | OSAVI | 3.5416 | -17.747 | 0.91 |
| WC24 | NDVI | 1.7845 | -8.446 | 0.92 |
| | OSAVI | 1.9865 | -9.5989 | 0.92 |

### 3.10.2 Colorado State University Arkansas Valley Research Center (CSU AVRC)

The CSU AVRC field is located approximately 4 km south of Rocky Ford, CO, at latitude 38.0385, longitude -103.6950, and elevation of 1274 m. The research center has a large monolithic lysimeter that was used to study corn evapotranspiration ($ET_{lys}$) in 2013. The lysimeter is 3.0 m x 3.0 m x 2.4 m and provided measurements of corn evapotranspiration for the entire year of 2013. Averaged hourly ET data were used on the analysis. Net radiation and soil heat flux plates were installed at the lysimeter location to provide measured $R_n$ and G data. Soil temperature in the lysimeter was measured using temperature probes. However, the data provided did not come with measurements of soil water content at shallow depth to account for the soil heat storage above the soil heat flux plates. Measurements of volumetric soil water content were done using neutron probe on a weekly basis at different depths, but the shallow readings are not reliable data since neutron probe readings tend to be biased due to the increased chances of fast neutrons being lost to the atmosphere.

The climate conditions are very similar to the ones in Greeley, Colorado. Summer season is similar to semiarid regions. Koppen climate classification for that area is BSk, which stands for tropical and subtropical desert climates. Average air temperature during the warmest month (July) is 24.6 °C, and average rainfall water depth during the wettest month (July) is 53.3 mm.

Weather data were acquired using $T_a$ and relative humidity and anemometers to be assumed at the same constant height above the canopy height. As the corn increased in biomass and height, the mast holding the cup anemometer was raised up to maintain consistency about the measurement height of 1 to 2 m above the canopy.

Remote sensing variables were obtained on site. Surface temperature was measured using IRT's positioned at NADIR view. RED and NIR surface reflectance data were obtained from MSR5 readings that took place on the following dates indicated by table 3.13. Crop height was interpolated for the days without measurement based on non-linear functions having DOY as a predictor. The models were obtained through the MATLAB curve fitting toolbox. Equation 3.90 shows the model for interpolating crop height.

$$h_c = 1.328 + 0.9064 \cdot cos(0.0578 \cdot DOY) - 0.692 \cdot sin(0.0578 \cdot DOY) \tag{3.90}$$

where crop height is given in m.

The analysis of $T_o$ and H were done considering previous assumptions of unstable atmospheric conditions, daytime data, and wind speed greater than 1.5 m/s. Inverted $T_o$ was calculated based on the approach adopted using LIRF data. The aerodynamic resistance and atmospheric stability corrections were determined based on the work of Yasuda (1988). Measured sensible heat flux was obtained as the residual from the surface energy balance and given as equation 3.91 indicates:

$$H_{lys} = R_n - G - LE_{lys} \tag{3.91}$$

where $H_{lys}$ is the sensible heat flux at the corn lysimeter ($W/m^2$); $LE_{lys}$ is the latent heat flux ($W/m^2$).

$LE_{lys}$ was calculated from the hourly corn evapotranspiration water depth from the lysimeter, as indicated by equation 3.92:

$$LE_{lys} = \lambda \cdot \frac{ET_{lys}}{3600} \tag{3.92}$$

Due to the lack of enough data to provide accurate determination of soil heat flux based on the soil heat flux plate method, measured G was assumed to be approximately equal to twice the magnitude of the averaged soil heat flux plate, which it was taken as the mean value between the four plates installed in the lysimeter. Inverted $T_o$ calculation also followed the same approach when using LIRF data.

**Table 3.13:** MSR5 measurements dates at CSU ARVC in 2013.

| Date | DOY | Date | DOY |
|---|---|---|---|
| 5/7/2013 | 127 | 8/18/2013 | 230 |
| 7/3/2013 | 184 | 8/23/2013 | 235 |
| 7/25/2013 | 206 | 8/30/2013 | 242 |
| 8/1/2013 | 213 | 9/3/2013 | 246 |
| 8/15/2013 | 227 | 9/6/2013 | 249 |

# Chapter 4

# Results and Analysis

## 4.1 Weather Conditions Assessment at LIRF in 2017-2018

Figure 4.1 shows the average daily weather conditions at LIRF for 2017 and 2018. The data was obtained from the CoAgMet station GLY04 from mid July to early October for both years. Figure 4.2 shows the average daytime weather conditions at LIRF for 2017 and 2018. Figure 4.3 shows the same weather variables on figures 4.1 and 4.2, but considering average data around noon time (hourly data from 10 am to 2 pm). Table 4.1, 4.2, 4.3, and 4.4 indicate, respectively, the summary statistics of air temperature, vapor pressure deficit (VPD), wind speed, and rainfall during 2017 and 2018. The variables n. $\bar{y}$, SD, and SE refer to, respectively, sample size, mean, standard deviation, and standard error.

Figures 4.4 and 4.5 refer to, respectively, the wind roses for the growing season of 2017 and 2018 to assess the patterns of wind flowing above the corn fields at LIRF. Tables 4.5 and 4.6 show, respectively, the t-test results for comparing the weather variables between years for daytime and around noon averaged values.

Air temperature and VPD conditions of both years were very similar (p-value $> 0.05$). For wind speed, however, data indicate that the year of 2017 had less strong wind speed than 2018 (p-values $< 0.05$). That indicates the year of 2018 provided overall more turbulent conditions for heat and vapor transfer between the surface and atmosphere. However, the mean wind speed for both years during the growing season fall into the category of calm winds, as indicated by Arya (2001) as air flowing at a rate less than 2.5 $m/s$. Regarding precipitation, the year of 2017 had more contribution of rainfall to the soil water balance than in 2018 as it may be seen on figure 4.1(d), and therefore, more days when clouds conditions may have an effect on physical processes

of water extraction and losses from both fields.

**Table 4.1:** Summary statistics of air temperature in 2017-2018.

| Year | Category | n | $\bar{y}$ | SD | SE |
|---|---|---|---|---|---|
| [-] | [-] | [-] | [°C] | [°C] | [°C] |
| 2017 | Daily | 84 | 18.67 | 4.38 | 0.48 |
| | Daytime | 84 | 21.25 | 5.21 | 0.57 |
| | Around Noon | 84 | 23.34 | 5.92 | 0.65 |
| 2018 | Daily | 84 | 19.10 | 3.88 | 0.42 |
| | Daytime | 84 | 22.06 | 4.41 | 0.48 |
| | Around Noon | 84 | 24.39 | 5.16 | 0.56 |

**Table 4.2:** Summary statistics of VPD in 2017-2018.

| Year | Category | n | $\bar{y}$ | SD | SE |
|---|---|---|---|---|---|
| [-] | [-] | [-] | [kPa] | [kPa] | [kPa] |
| 2017 | Daily | 84 | 1.007 | 0.505 | 0.055 |
| | Daytime | 84 | 1.435 | 0.725 | 0.079 |
| | Around Noon | 84 | 1.724 | 0.915 | 0.100 |
| 2018 | Daily | 84 | 1.167 | 0.526 | 0.057 |
| | Daytime | 84 | 1.640 | 0.750 | 0.082 |
| | Around Noon | 84 | 1.950 | 0.975 | 0.106 |

**Table 4.3:** Summary statistics of wind speed in 2017-2018.

| Year | Category | n | $\bar{y}$ | SD | SE |
|---|---|---|---|---|---|
| [-] | [-] | [-] | [m/s] | [m/s] | [m/s] |
| 2017 | Daily | 84 | 1.467 | 0.495 | 0.054 |
| | Daytime | 84 | 1.689 | 0.649 | 0.071 |
| | Around Noon | 84 | 1.756 | 0.936 | 0.102 |
| 2018 | Daily | 84 | 1.596 | 0.556 | 0.061 |
| | Daytime | 84 | 1.884 | 0.768 | 0.084 |
| | Around Noon | 84 | 2.036 | 0.963 | 0.105 |

**Table 4.4:** Summary statistics of rainfall in 2017-2018.

| Year | Category | n | $\bar{y}$ | SD | SE |
|---|---|---|---|---|---|
| [-] | [-] | [-] | [mm] | [mm] | [mm] |
| 2017 | Daily | 84 | 0.05 | 0.17 | 0.02 |
| | Daytime | 84 | 0.06 | 0.27 | 0.03 |
| | Around Noon | 84 | 0.00 | 0.02 | 0.00 |
| 2018 | Daily | 84 | 0.01 | 0.04 | 0.00 |
| | Daytime | 84 | 0.01 | 0.02 | 0.00 |
| | Around Noon | 84 | 0.00 | 0.03 | 0.00 |

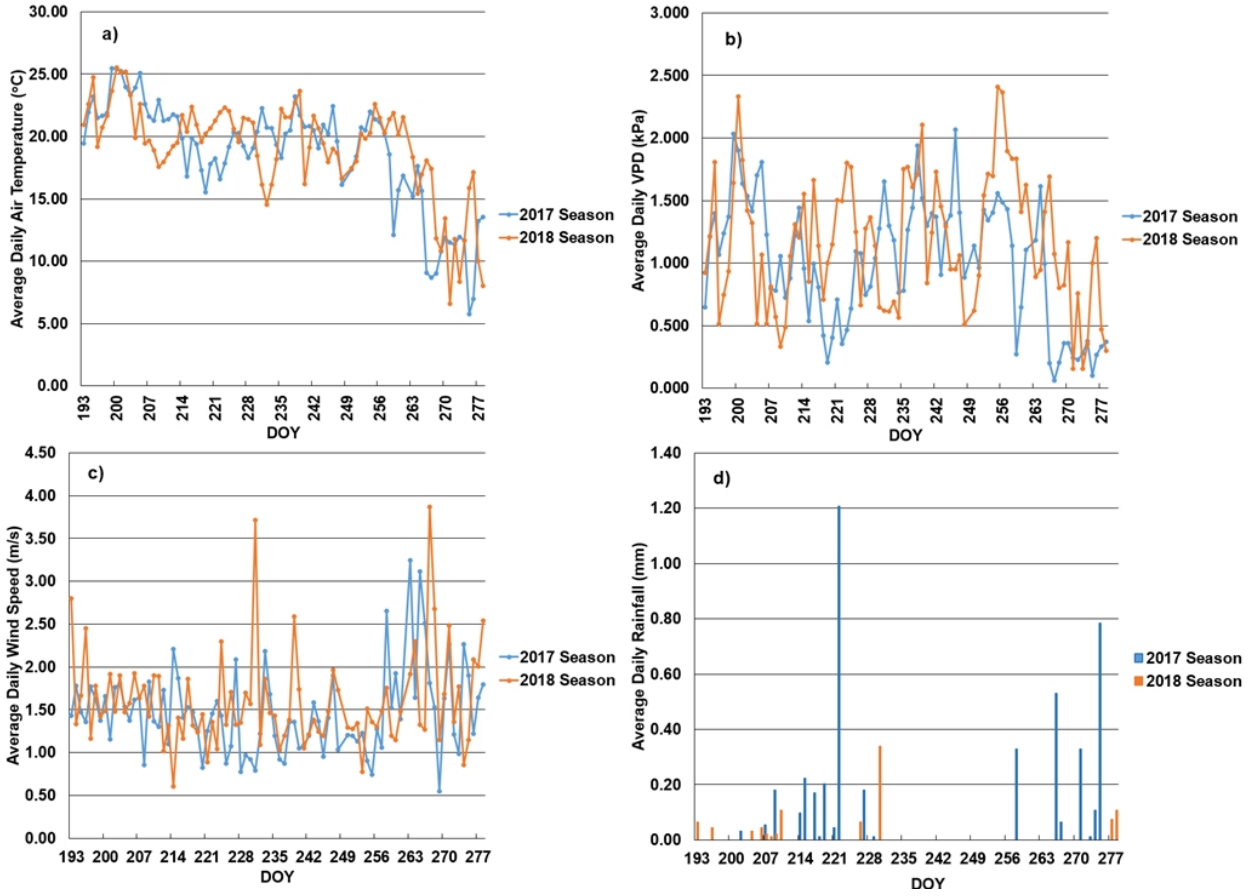


**Figure 4.1:** Average daily weather conditions at LIRF in 2017-2018. Graphs 4.1(a), 4.1(b), 4.1(c), and 4.1(d) show, respectively, air temperature, vapor pressure deficit (VPD), wind speed, and rainfall averaged daily data for both years based on CoAgMet weather station data at LIRF.

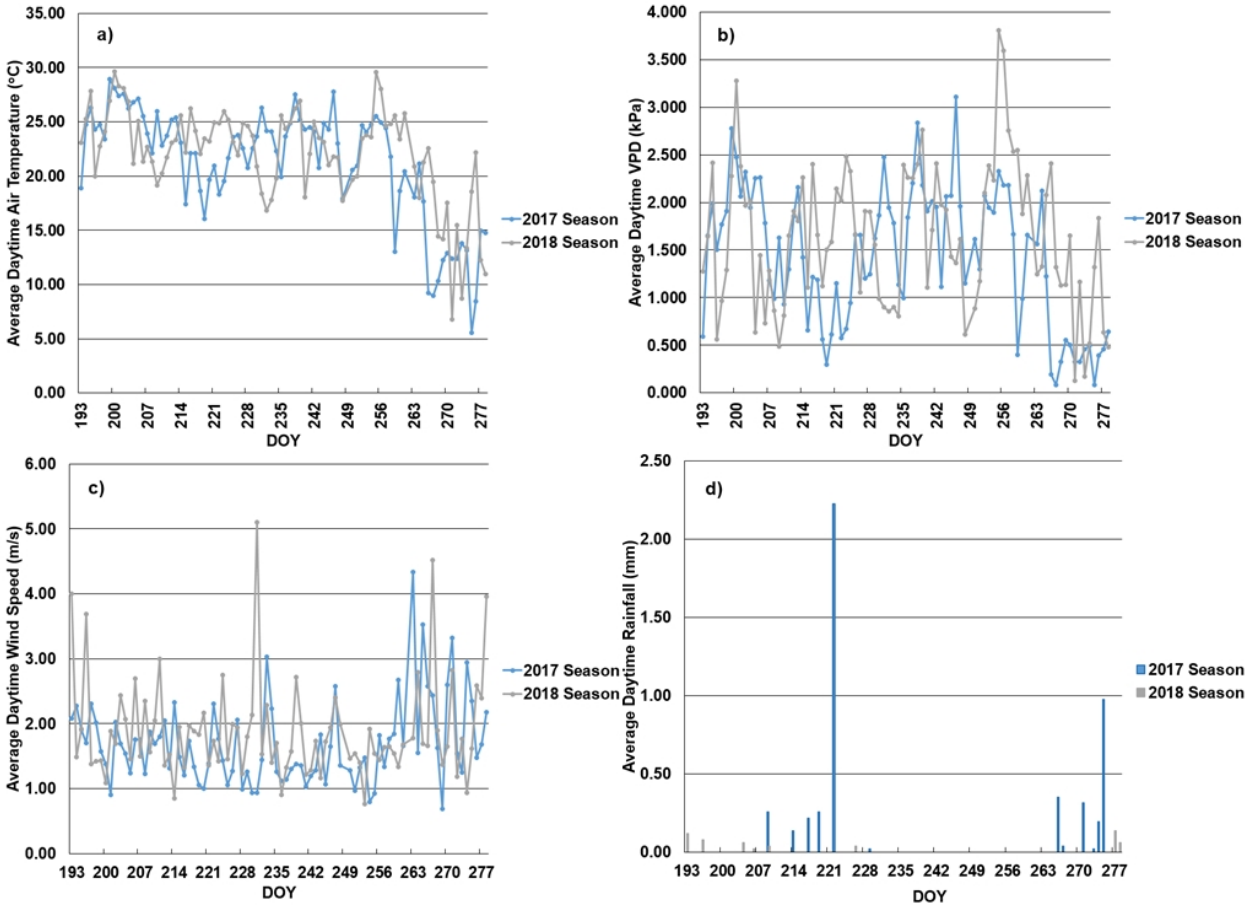


**Figure 4.2:** Average daytime weather conditions at LIRF in 2017-2018. Graphs 4.2(a), 4.2(b), 4.2(c), and 4.2(d) show, respectively, daily air temperature, vapor pressure deficit (VPD), wind speed, and rainfall averaged during daytime (6 am to 6 pm) data for both years.

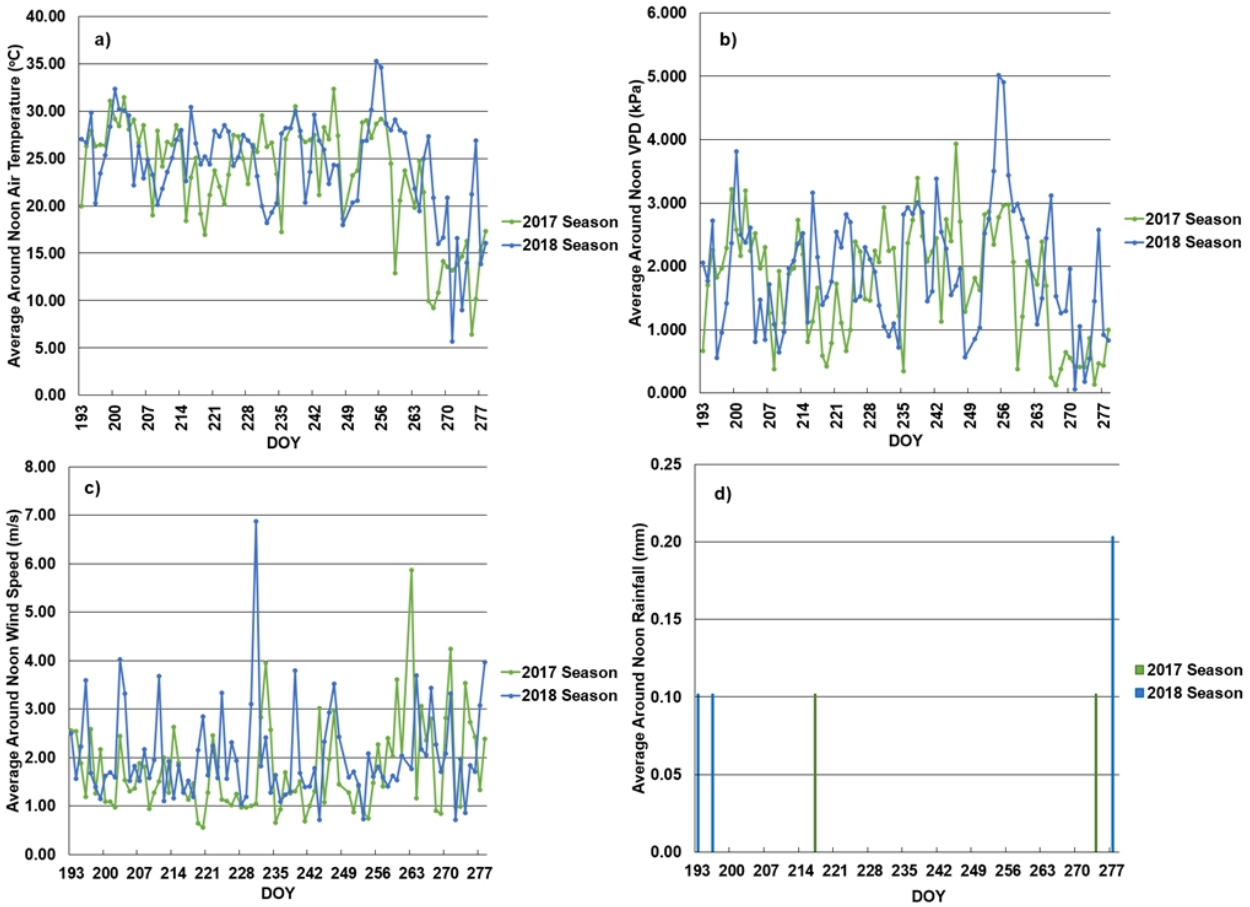


**Figure 4.3:** Average around noon weather conditions at LIRF in 2017-2018. Graphs 4.3(a), 4.3(b), 4.3(c), and 4.3(d) show, respectively, daily air temperature, vapor pressure deficit (VPD), wind speed, and rainfall averaged around noon time (10 am to 2 pm) data for both years.

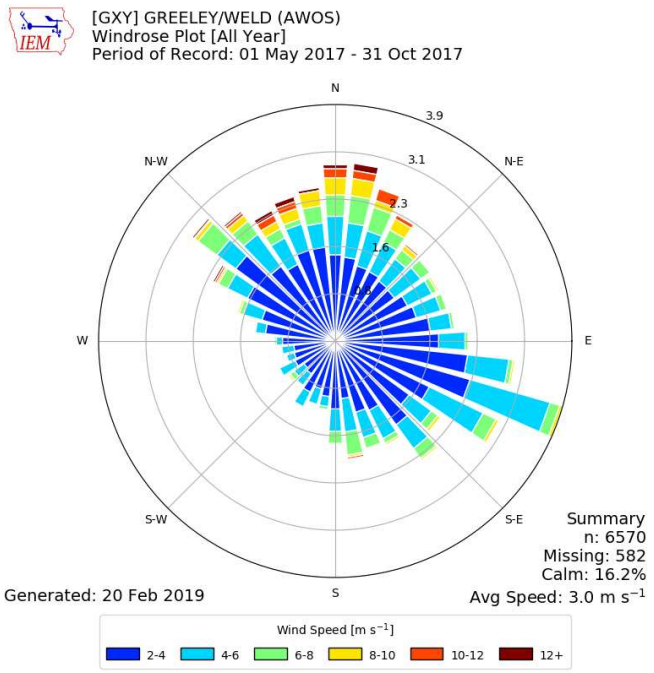


**Figure 4.4:** Wind rose showing the wind properties during the growing season of 2017.

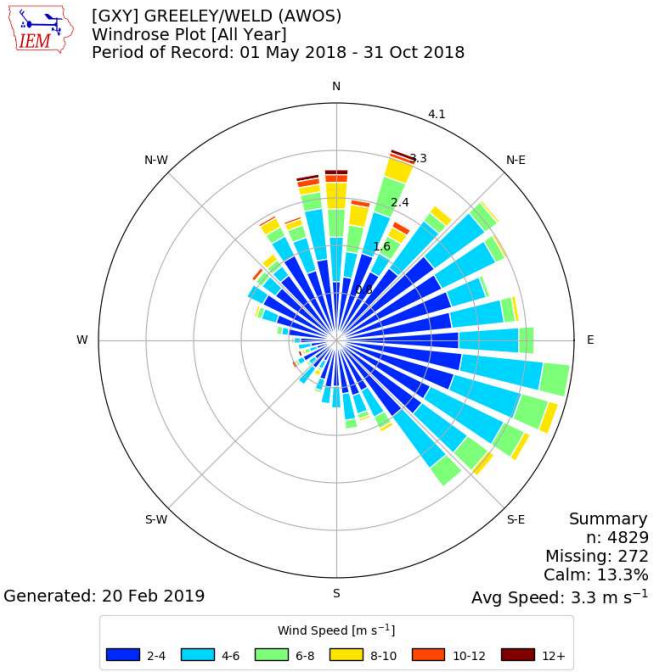


**Figure 4.5:** Wind rose showing the wind properties during the growing season of 2018.

**Table 4.5:** Rank sum test results for daytime Conditions.

| Weather Variable | t-Test | | $H_A$ | Test Conclusion |
|---|---|---|---|---|
| [-] | p-value | Test-Statistic | [-] | [-] |
| $T_a$ | 0.5605 | 3344 | $\mu_{17} \neq \mu_{18}$ | Do not Reject $H_o$ |
| | 0.2802 | 3344 | $\mu_{17} < \mu_{18}$ | Do not Reject $H_o$ |
| u | 0.0465 | 2900 | $\mu_{17} \neq \mu_{18}$ | Do not Reject $H_o$ |
| | 0.0233 | 3900 | $\mu_{17} < \mu_{18}$ | Do not Reject $H_o$ |
| VPD | 0.1109 | 3025 | $\mu_{17} \neq \mu_{18}$ | Do not Reject $H_o$ |
| | 0.0555 | 3025 | $\mu_{17} < \mu_{18}$ | Do not Reject $H_o$ |

**Table 4.6:** Rank sum test results for around noon time conditions.

| Weather Variable | t-Test | | $H_A$ | Test Conclusion |
|---|---|---|---|---|
| [-] | p-value | Test-Statistic | [-] | [-] |
| $T_a$ | 0.4342 | 3281 | $\mu_{17} \neq \mu_{18}$ | Do not Reject $H_o$ |
| | 0.2171 | 3281 | $\mu_{17} < \mu_{18}$ | Do not Reject $H_o$ |
| u | 0.0073 | 2682 | $\mu_{17} \neq \mu_{18}$ | Reject $H_o$ |
| | 0.0037 | 2682 | $\mu_{17} < \mu_{18}$ | Reject $H_o$ |
| VPD | 0.1885 | 3113 | $\mu_{17} \neq \mu_{18}$ | Do not Reject $H_o$ |
| | 0.0943 | 3113 | $\mu_{17} < \mu_{18}$ | Do not Reject $H_o$ |

## 4.2 Measured Heat Fluxes Results

### 4.2.1 Measured $R_n$

Figure 4.6 shows the comparison between the point-source measured $R_n$ per stations and fields in 2017 and 2018. Table 4.7 shows the summary statistic of the measured $R_n$. The variables n, $\bar{y}$, SD, and SE are respectively, the sample size, sample mean, sample standard deviation, and stan-

dard error.

The measured $R_n$ was evaluated during daytime conditions and when the average values between the two stations per field were positive and greater than 0.

The measurements of net radiation on the different irrigation treatments seem to be similar on average based on the large sample sizes analyzed. For all stations in the deficit and fully irrigated fields, with exception of station 1.2, the sample mean and standard error values were similar in magnitude. For station 1.2 only, the data from the deficit irrigated treatment (year 2017) and fully irrigated treatment (year 2018) were quite different based on the sample mean (250.1 $W/m^2$ and 309.2 $W/m^2$, respectively) and standard error values (2.8 $W/m^2$ and 3.5 $W/m^2$, respectively).

It seems that for the year of 2017, there were considerable variability between measurements within the same treatment plot, when compared with 2018 data. As 2017 data is compared by having the 1:1 line as reference, the measurements at station 1.1 were overall greater than the data provided by station 1.2. The sensors were installed at the same fields in both years, which it may indicate that the performance of the sensors from one year to another is reliable on the weather patterns for a given season. A possible explanation for the discrepancies between measured $R_n$ between 2017 and 2018 are related to: presence of birds, stations mast and poles installation issues, and leveling the sensors. Those factors could be the cause for the evident variability of the measurements identified during the 2017 data collection campaign.

**Table 4.7:** Summary statistics of the measured $R_n$ per station in 2017 and 2018.

| Station | Year | n | $\bar{y}$ | SD | SE |
|---|---|---|---|---|---|
| [-] | [-] | [-] | $[W/m^2]$ | $[W/m^2]$ | $[W/m^2]$ |
| 1.1 | 2017 | 3741 | 307.8 | 209.7 | 3.4 |
| 1.1 | 2018 | 3522 | 300.7 | 198.5 | 3.3 |
| 1.2 | 2017 | 3741 | 250.1 | 172.1 | 2.8 |
| 1.2 | 2018 | 3522 | 309.2 | 208.7 | 3.5 |
| 2.1 | 2017 | 4090 | 292.8 | 206.7 | 3.2 |
| 2.1 | 2018 | 3714 | 305.7 | 215.3 | 3.5 |
| 2.2 | 2017 | 4090 | 310.1 | 211.2 | 3.3 |
| 2.2 | 2018 | 3714 | 314.7 | 206.5 | 3.4 |

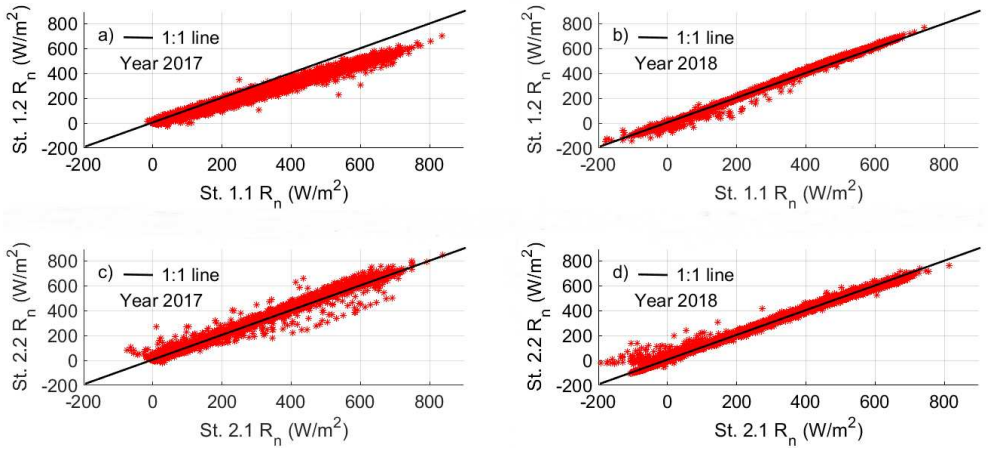


**Figure 4.6:** Net radiation point measurement comparisons in 2017-2018. Graphs 4.6(a) and 4.6(b) show $R_n$ measurements on Field 01 for, respectively, deficit irrigated and fully irrigated treatments. Graphs 4.6(c) and 4.6(d) show $R_n$ measurements on Field 02 for, respectively, fully irrigated and deficit irrigated treatments.

### 4.2.2 Measured G

Tables 4.8 and 4.9 show, respectively, the summary statistics of the measured $G$ during daytime and around noon conditions. Tables 4.10 to 4.13 indicate the calibration equation coefficients for

each station per year and accounting for the measurements below and between corn rows.

The measured G is dependent on the soil texture, water holding capacity, changes in soil bulk density through compaction of the soil particles, etc. Among stations within the same field, the differences in soil heat flux magnitude might be attributed to differences on biomass growth that affect the amount of energy that goes into the soil profile. From tables 4.8 and 4.9, it is evident that the measurements of soil heat flux were significant different based on the SE values. For Field 02, the small differences in SE values from one year to another indicates that the stations were positioned at locations with similar soil type for both years. However, for Field 01, it is possible to infer that the measurements of G from 2017 to 2018 were different due to the station's location and soil type.

The soil heat flux plates, temperature probes, and soil water content sensors had to be moved to a different location than 2017 because of technical issues during the seeding stage at the beginning of the season. Therefore, differences in soil heat flux magnitude were expected to occur due to the soil variability across the fields. Another factor to take into consideration is the influence of the subsurface drip line location on the wet bulb shape and expansion within the root zone. Depending on the location of the soil heat flux plates in regards to the drip system, the changes on soil water content above the plates might not be capturing the entire soil water dynamics over time, which it could affect the soil heat storage computation and the determination of measured surface soil heat flux.

**Table 4.8:** Descriptive statistic of measured G during daytime in 2017 and 2018.

| Station | Year | n | $\bar{y}$ | SD | SE |
|---|---|---|---|---|---|
| [-] | [-] | [-] | $[W/m^2]$ | $[W/m^2]$ | $[W/m^2]$ |
| 1.1 | 2017 | 2525 | 71.8 | 55.2 | 1.1 |
| 1.1 | 2018 | 1900 | 52.1 | 35.7 | 0.8 |
| 1.2 | 2017 | 2525 | 46.4 | 26.6 | 0.5 |
| 1.2 | 2018 | 1900 | 63.9 | 54.0 | 1.2 |
| 2.1 | 2017 | 2279 | 33.8 | 22.8 | 0.5 |
| 2.1 | 2018 | 2210 | 31.7 | 21.9 | 0.5 |
| 2.2 | 2017 | 2279 | 36.7 | 33.5 | 0.7 |
| 2.2 | 2018 | 2210 | 46.7 | 34 | 0.7 |

**Table 4.9:** Descriptive statistic of measured G around noon time in 2017 and 2018.

| Station | Year | n | $\bar{y}$ | SD | SE |
|---|---|---|---|---|---|
| [-] | [-] | [-] | $[W/m^2]$ | $[W/m^2]$ | $[W/m^2]$ |
| 1.1 | 2017 | 1423 | 92.1 | 56.1 | 1.5 |
| 1.1 | 2018 | 1049 | 73.5 | 32.1 | 1.0 |
| 1.2 | 2017 | 1423 | 58.4 | 24.0 | 0.6 |
| 1.2 | 2018 | 1049 | 92.5 | 53.9 | 1.7 |
| 2.1 | 2017 | 1183 | 44.7 | 22.6 | 0.7 |
| 2.1 | 2018 | 1063 | 46.8 | 19.3 | 0.6 |
| 2.2 | 2017 | 1183 | 50.3 | 37.2 | 1.1 |
| 2.2 | 2018 | 1063 | 73.0 | 27.6 | 0.8 |

**Table 4.10:** Calibration equation coefficients for volumetric SWC at Field 1 below corn row.

| Station | Year | $\hat{\beta}_1$ | $\hat{\beta}_2$ | $R^2$ |
|---|---|---|---|---|
| 1.1 | 2017 | 0.4028 | 0.1004 | 0.70 |
| 1.2 | 2017 | 1.5417 | -0.0307 | 0.80 |
| 1.1 | 2018 | 1.0771 | 0.0166 | 0.87 |
| 1.2 | 2018 | 1.1003 | -0.0123 | 0.79 |

**Table 4.11:** Calibration equation coefficients for volumetric SWC at Field 1 between corn rows.

| Station | Year | $\hat{\beta}_1$ | $\hat{\beta}_2$ | $R^2$ |
|---|---|---|---|---|
| 1.1 | 2017 | 1.8243 | 0.0135 | 0.87 |
| 1.2 | 2017 | 1.6787 | -0.0226 | 0.85 |
| 1.1 | 2018 | 3.1428 | -0.4081 | 0.81 |
| 1.2 | 2018 | 0.393 | 0.0861 | 0.85 |

**Table 4.12:** Calibration equation coefficients for volumetric SWC at Field 2 below corn row.

| Station | Year | $\hat{\beta}_1$ | $\hat{\beta}_2$ | $R^2$ |
|---|---|---|---|---|
| 2.1 | 2017 | 1.9041 | 0.153 | 0.88 |
| 2.2 | 2017 | 1.1059 | 0.0936 | 0.80 |
| 2.1 | 2018 | 1.1818 | 0.0282 | 0.91 |
| 2.2 | 2018 | 1.3748 | -0.0606 | 0.84 |

**Table 4.13:** Calibration equation coefficients for volumetric SWC at Field 2 between corn rows.

| Station | Year | $\hat{\beta}_1$ | $\hat{\beta}_2$ | $R^2$ |
|---|---|---|---|---|
| 2.1 | 2017 | 1.4825 | 0.0285 | 0.78 |
| 2.2 | 2017 | 2.6389 | -0.2692 | 0.71 |
| 2.1 | 2018 | 1.7791 | -0.0214 | 0.94 |
| 2.2 | 2018 | 0.3984 | 0.0747 | 0.76 |

### 4.2.3 Multiple Pairwise Comparison Among Measured H

Tables 4.14 to 4.17 show the summary of the multiple pairwise comparisons obtained after Dunn's test was performed for the 2017 and 2018 measured sensible heat flux data. The "*" symbol nearby the p-values is to highlight values that are less than 0.025.

Figures 4.7 and 4.8 indicate, respectively, the boxplot graphs of the measured sensible heat flux for 2017 and 2018 data.

For the fully irrigated field in 2017, the sensible heat obtained from Bowen ratio and aerodynamic methods were different than all other methods (p-value $< 0.025$). The statistical differences in population mean between LAS and Bowen ratio methods could be justify based on sensors installation issues such as leveling of the cross-arms on the aerodynamic flux towers. Thus, bias on air temperature and relative humidity were potentially introduced into the measurements. Therefore, for Field 01, the measured sensible heat from LAS and Eddy covariance were used to assess sensible heat flux model performance. In 2018, the LAS and BR sensible heat fluxes were statistically proven to yield similar results (p-value $> 0.025$). Therefore, they were the measured H data set used on the analysis of the data in 2018.

For the deficit irrigated field in 2017 and 2018, only the aerodynamic profile method was shown able to provide sensible heat results that were different than the other two methods (p-value $< 0.025$). Therefore, only LAS and Bowen ratio method were used to assess the sensible heat flux model.

The AERO H measured values do not statistically provide similar results compared to LAS H measurements possibly due to limitations on the sensors resolution to capture significant changes on the gradients of air temperature and humidity between two consecutive measurement heights. The Bowen ratio method has shown statistically to be more reliable for providing data to cross reference LAS H measurement on the deficit irrigated field only due to the fact that the differences in height between the the two point source for the air temperature and vapor pressure gradient were significant large to minimize the sensors resolution issue.

Eddy covariance and LAS H measurements were expected to be statistically the same since both systems integrate sensible heat fux measurements over an area rather than being point source determination. Although, their respective footprints are not the same since the LAS system typically has a wider footprint compared to EC. Another fact that corroborates with that result is the calculation of friction velocity from both systems. As figure 4.9 indicates, the plot LAS u* vs. EC U* shows good agreement ($R^2 = 0.91$) between both data. The main difference to the validation of EC measurements is the post-processing corrections steps that must take place to adjust the initial H values measured by the network of sensors.

**Table 4.14:** Dunn's test statistic results for the deficit irrigated field in 2017.

| Measured H | AERO | BR | Variable |
|---|---|---|---|
| BR | -2.527 | - | Test-Statistic |
| | 0.0171* | - | p-value |
| LAS | -3.0078 | -0.4801 | Test-Statistic |
| | 0.0039* | 0.6794 | p-value |

**Table 4.15:** Dunn's test statistic results for the fully irrigated field in 2017.

| Measured H | AERO | BR | $EC_s$ | $EC_c$ | Variable |
|---|---|---|---|---|---|
| BR | -0.3051 | - | - | - | Test-Statistic |
| | 0.9916 | - | - | - | p-value |
| $EC_s$ | -3.2591 | -2.9540 | - | - | Test-Statistic |
| | 0.0056* | 0.0156* | - | - | p-value |
| $EC_c$ | -1.4991 | -1.1940 | 1.7600 | - | Test-Statistic |
| | 0.4998 | 0.7094 | 0.3296 | - | p-value |
| LAS | -3.2061 | -2.9009 | 0.0531 | -1.7070 | Test-Statistic |
| | 0.0067* | 0.0184* | 0.9985 | 0.3618 | p-value |

**Table 4.16:** Dunn's test statistic results for the deficit irrigated field in 2018.

| Measured H | AERO | BR | Variable |
|---|---|---|---|
| BR | -2.5970 | - | Test-Statistic |
| | 0.0140* | - | p-value |
| LAS | -3.7443 | -1.1473 | Test-Statistic |
| | 0.0003* | 0.3315 | p-value |

**Table 4.17:** Dunn's test statistic results for the fully irrigated field in 2018.

| Measured H | AERO | BR | Variable |
|---|---|---|---|
| BR | 5.8455 | - | Test-Statistic |
| | 0.0000* | - | p-value |
| LAS | 3.4944 | -2.3511 | Test-Statistic |
| | 0.0007* | 0.0278 | p-value |

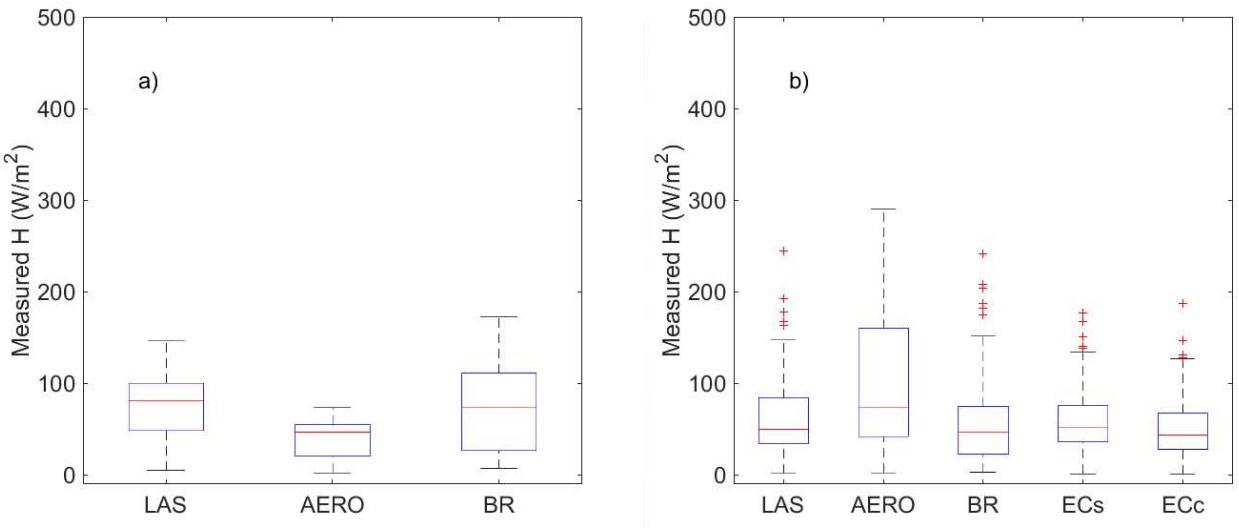


**Figure 4.7:** Graphs 4.7(a) and 4.7(b) show, respectively, the boxplots for the deficit and fully irrigated treatment in 2017.

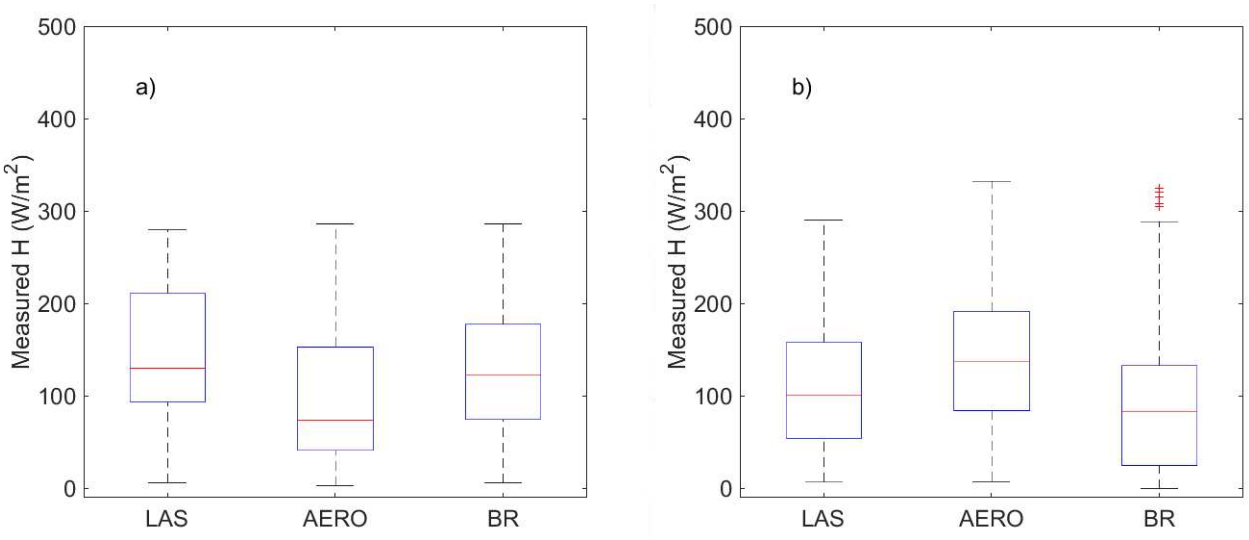


**Figure 4.8:** Graphs 4.8(a) and 4.8(b) show, respectively, the boxplots for the deficit and fully irrigated treatment in 2018.

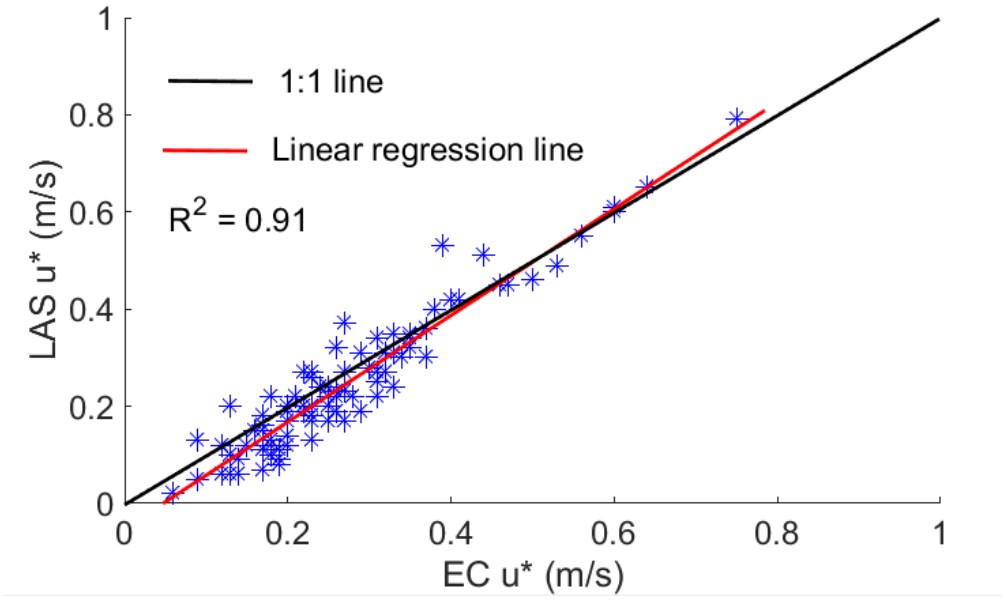


**Figure 4.9:** EC u* vs. LAS u* for fully irrigated field at LIRF in 2017.

## 4.3 $T_o$ Model Results for LIRF

The following $T_o$ empirical models are the result of fitting the data collected over both LIRF fields during the years of 2017 and 2018 as indicated on section 3.4 of this thesis.

### 4.3.1 General Linear Model for $T_o$

Equation 4.1 ($R^2 = 0.96$) shows the general linear model for $T_o$ based on all data available for 0.85 < LAI < 5.00.

$$T_o = 1.025 \cdot f_c + 0.407 \cdot T_a + 0.631 \cdot T_s + 0.498 \cdot r_p \tag{4.1}$$

Tables 4.18 and 4.19 show, respectively, the statistics of the multiple linear regression analysis for the general linear $T_o$ model and model quality assessment. Figure 4.10 shows the Inverted LAS $T_o$ vs. Estimated $T_o$ plot regarding data used to fit the model indicated by equation 4.1. Table 4.20 presents the model performance under difference scenarios of VPD and wind speed.

It seems that the general linear $T_o$ model had better agreement in 2018 than 2017 based on $d_r$. The performance of the model in 2017 is subject to uncertainties on the determination of LAS sensible heat flux, since the determination of the Bowen ratio for the iterative process of calculating H based on the scintillometers is highly dependant on the accuracy of measured $R_n$ and $G$. As indicated earlier, the measurements of net radiation and soil heat flux at two different location within each fields seemed to present more variability in 2017 than 2018, which it might have added some bias on the LAS H calculation, and, consequently, the Inverted $T_o$ values obtained from the LAS sensible heat flux.

When combining the data from 2017 and 2018, equation 4.1 seemed to perform similarly for both irrigation treatment conditions based on the refined index of agreement being of the same magnitude ($0.90 \approx 0.91$). Similar $d_r$ values would have been expected based on the fact that em-

pirical model was derived from the same data set in which the model assessment has taken place. Another reason to support the findings relies on the fact that the general linear model coefficients are a byproduct of the main different biomass conditions and wind patterns above the surface.

The statistics indicated by table 4.19 show that the empirical coefficients on equation 4.1 have p-values less 0.05. Figure 4.10 indicates that there's more variability on the prediction of $T_o$ at larger values in 2017 on both irrigation treatments. That could be related to bias added from measured $R_n$ and G on Bowen ratio estimates.

The effect of VPD and wind speed magnitude seem to have an influence in the general linear $T_o$ model performance. For low values of VPD (VPD $<$ 2.5 kPa), the model seems to perform similarly regardless of the wind speed range on both fields. That is evident based on $d_r$ values to present small variability, even though the RMSE for are smaller for wind speed conditions greater than 2 m/s. That could be caused by differences on the sample size for the analysis.

When atmospheric conditions demanded more energy for evapotranspiration based on large VPD values (VPD $>$ 2.5 kPa), the effects on the model performance were similar regardless the water management practice selected. For the deficit and fully irrigated fields, the conditions of dry atmosphere and high wind speed provide better model agreement than when wind conditions are slightly less turbulent based on smaller refined index of agreement for the latter condition (0.81 $<$ 0.87 and 0.70 $<$ 0.82 for, respectively, deficit and fully irrigated treatment fields). When the atmosphere is dry and wind conditions provide enough air mixing and turbulence, the crop will attempt to minimize the internal temperature changes by decreasing the canopy temperature through transpiration. More turbulence conditions have an effect on how easily the transfers of heat and vapor will occur, which is indicated by smaller aerodynamic resistance to heat transfer between the surface and the atmosphere.

**Table 4.18:** Regression statistics of general linear $T_o$ model (equation 4.1).

| Coefficient | Variable | Estimate | SE | Test Statistic | p-value |
|---|---|---|---|---|---|
| $a_1$ | $f_c$ | 1.025 | 0.2847 | 3.6019 | $3.5419 \cdot 10^{-4}$ |
| $a_2$ | $T_a$ | 0.407 | 0.0247 | 16.4970 | $2.2238 \cdot 10^{-47}$ |
| $a_3$ | $T_s$ | 0.631 | 0.0200 | 31.5520 | $2.611 \cdot 10^{-112}$ |
| $a_4$ | $r_p$ | 0.498 | 0.2423 | 2.0548 | 0.0405 |

**Table 4.19:** Statistics model quality assessment of the general linear $T_o$ model (equation 4.1).

| Treatment Plot | Year | n | MBE | RMSE | Pearson's R | $d_r$ |
|---|---|---|---|---|---|---|
| [-] | [-] | [-] | [°C] | [°C] | [-] | [-] |
| Deficit Irrigated | 2017 | 33 | -0.49 | 1.50 | 0.95 | 0.83 |
| | 2018 | 135 | -0.34 | 1.02 | 0.99 | 0.93 |
| | 2017 and 2018 | 168 | -0.37 | 1.13 | 0.99 | 0.91 |
| Fully Irrigated | 2017 | 107 | 0.18 | 1.35 | 0.96 | 0.85 |
| | 2018 | 144 | 0.15 | 0.93 | 0.99 | 0.92 |
| | 2017 and 2018 | 251 | 0.16 | 1.13 | 0.98 | 0.90 |

**Table 4.20:** Model quality assessment of the general linear $T_o$ model (equation 4.1) regarding different VPD and wind speed conditions for LIRF 2017-2018 combined data.

| Treatment site | VPD range | Wind speed range | n | MBE | RMSE | Pearson's R | $d_r$ |
|---|---|---|---|---|---|---|---|
| [-] | [kPa] | [m/s] | [-] | [°C] | [°C] | [-] | [-] |
| Deficit Irrigated Field | VPD $< 2.5$ | u $< 2$ | 84 | -0.60 | 1.23 | 0.98 | 0.90 |
| | | u $> 2$ | 36 | -0.35 | 0.99 | 0.99 | 0.89 |
| | VPD $> 2.5$ | u $< 2$ | 34 | -0.13 | 1.06 | 0.93 | 0.81 |
| | | u $> 2$ | 14 | 0.40 | 1.08 | 0.96 | 0.87 |
| Fully Irrigated Field | VPD $< 2.5$ | u $< 2$ | 108 | -0.03 | 0.85 | 0.99 | 0.91 |
| | | u $> 2$ | 53 | 0.17 | 0.83 | 0.97 | 0.89 |
| | VPD $> 2.5$ | u $< 2$ | 64 | 0.54 | 1.69 | 0.85 | 0.70 |
| | | u $> 2$ | 26 | 0.03 | 0.87 | 0.90 | 0.82 |

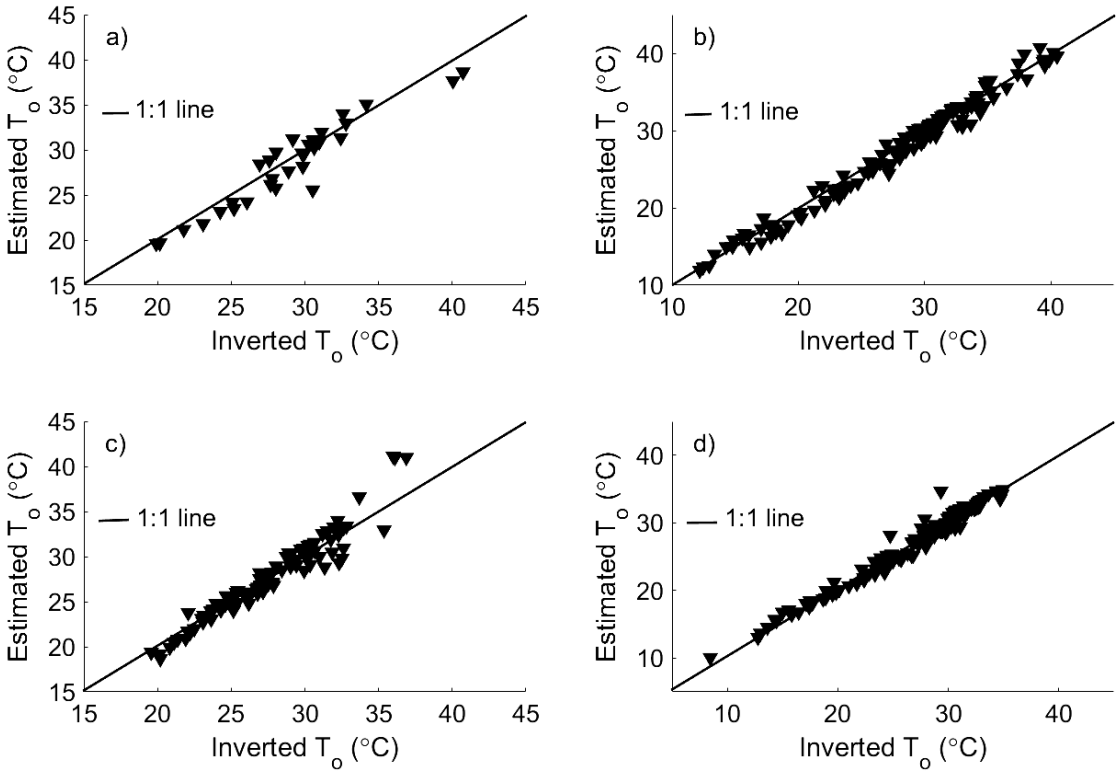


**Figure 4.10:** Inverted LAS $T_o$ vs. Estimated $T_o$ for different treatment sites in 2017 and 2018 regarding general linear model for $T_o$ (equation 4.1). Graphs 4.10(a) and 4.10(b) show $T_o$ plots of the deficit irrigated field for, respectively, 2017 and 2018. Graphs 4.10(c) and 4.10(d) show $T_o$ plots of the fully irrigated field for, respectively, 2017 and 2018.

### 4.3.2 General Non-Linear Model for $T_o$

Equation 4.2 ($R^2 = 0.93$) shows the general non-linear model for $T_o$ based on all data available for 0.85 < LAI < 5.00.

$$T_o = T_a + 0.990 \cdot ln|T_s - T_a| + 0.171 \cdot \frac{r_p}{f_c} + 2.643 \tag{4.2}$$

Tables 4.21 and 4.22 show, respectively, the statistics of the multiple non-linear regression analysis for the general non-linear $T_o$ model and model quality assessment. Figure 4.11 shows the Inverted LAS $T_o$ vs. Estimated $T_o$ plot using the general non-linear model developed. Table 4.23 presents the model performance under difference scenarios of VPD and wind speed.

The general non-linear $T_o$ model seems to have better agreement under 2018 data set than 2017. That is susceptible to be related to the same reasons that caused the general linear model to have better results in 2018. When compared with the general linear $T_o$ model, the general non-linear equation does not perform similarly by having large absolute value of MBE and higher RMSE. The refined index of agreement for the given model is also less than all the case scenarios for the general linear $T_o$ model. That is an indication that the non-linear approach has limitations when estimating $T_o$ that might be related to the nature of the absolute value of temperature gradient $(T_s - T_a)$ incorporated as a natural logarithm term and the relationship between $r_p$ and $f_c$. The regression statistical analysis indicate that the p-value for the term $\frac{r_p}{f_c}$ is larger than 0.05, which indicates that there is not statistical evidence to infer to validate the respective empirical coefficient $p_2$ on the general non-linear $T_o$ model.

The general non-linear $T_o$ model seems to have a similar performance under multiple VPD and wind speed scenarios to the general linear $T_o$ model. For VPD $<$ 2.5 kPa and high wind speed conditions, the model seems to perform slightly better under the fully irrigated treatment. When the evapotranspiration conditions are increased due to large VPD and wind speed ranges, the model performs better under the deficit irrigated field by having a larger $d_r$ and smaller RMSE. That could be explained based on the fact that the water stressed field has overall less healthy biomass exposed to the soil-canopy-atmosphere interaction and shorter canopy height when compared to the non-water stressed field.

**Table 4.21:** Regression statistics of general non-linear $T_o$ model (equation 4.2).

| Coefficient | Estimate | SE | Test Statistic | p-value |
|---|---|---|---|---|
| $p_1$ | 0.990 | 0.0583 | 16.979 | $1.6750 \cdot 10^{-49}$ |
| $p_2$ | 0.171 | 0.2099 | 0.8170 | 0.4144 |
| $p_3$ | 2.643 | 0.1132 | 23.3600 | $1.0392 \cdot 10^{-77}$ |

**Table 4.22:** Statistics model quality assessment of the general non-linear $T_o$ model (equation 4.2).

| Treatment Plot | Year | n | MBE | RMSE | Pearson's R | $d_r$ |
|---|---|---|---|---|---|---|
| [-] | [-] | [-] | [°C] | [°C] | [-] | [-] |
| Deficit Irrigated | 2017 | 33 | -0.87 | 2.16 | 0.90 | 0.79 |
| | 2018 | 135 | -0.53 | 1.31 | 0.99 | 0.90 |
| | 2017 and 2018 | 168 | -0.60 | 1.51 | 0.98 | 0.89 |
| Fully Irrigated | 2017 | 107 | 0.51 | 1.68 | 0.96 | 0.77 |
| | 2018 | 144 | 0.32 | 1.26 | 0.98 | 0.89 |
| | 2017 and 2018 | 251 | 0.40 | 1.46 | 0.97 | 0.85 |

**Table 4.23:** Model quality assessment of the general non-linear $T_o$ model (equation 4.2) regarding different VPD and wind speed conditions for LIRF 201-2018 combined data.

| Treatment site | VPD range | Wind speed range | n | MBE | RMSE | Pearson's R | $d_r$ |
|---|---|---|---|---|---|---|---|
| [-] | [kPa] | [m/s] | [-] | [°C] | [°C] | [-] | [-] |
| Deficit Irrigated Field | VPD $< 2.5$ | u $< 2$ | 84 | -0.49 | 1.34 | 0.98 | 0.89 |
| | | u $> 2$ | 36 | -0.56 | 1.38 | 0.97 | 0.86 |
| | VPD $> 2.5$ | u $< 2$ | 34 | -0.18 | 0.92 | 0.95 | 0.83 |
| | | u $> 2$ | 14 | 0.40 | 1.08 | 0.96 | 0.87 |
| Fully Irrigated Field | VPD $< 2.5$ | u $< 2$ | 108 | -0.06 | 1.34 | 0.96 | 0.86 |
| | | u $> 2$ | 53 | -0.05 | 0.94 | 0.96 | 0.87 |
| | VPD $> 2.5$ | u $< 2$ | 64 | 1.26 | 1.87 | 0.86 | 0.56 |
| | | u $> 2$ | 26 | 1.12 | 1.59 | 0.86 | 0.59 |

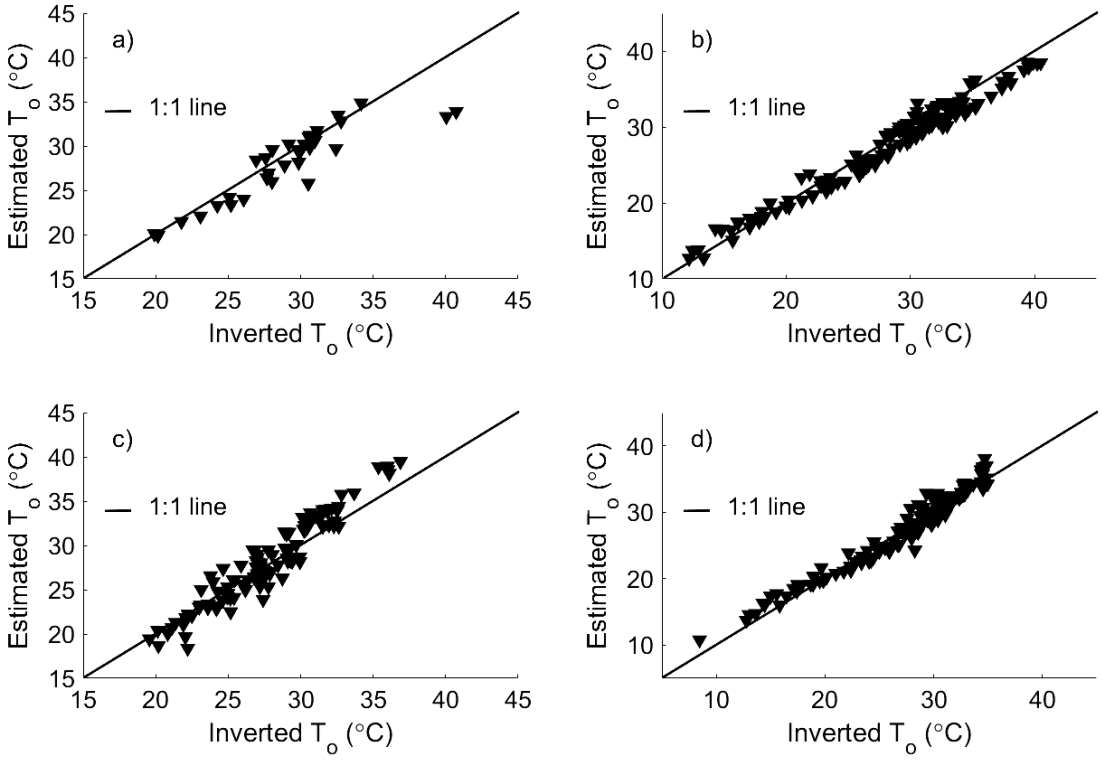


**Figure 4.11:** Inverted LAS $T_o$ vs. Estimated $T_o$ for different treatment sites in 2017 and 2018 regarding general non-linear $T_o$ model (equation 4.2). Graphs 4.11(a) and 4.11(b) show $T_o$ plots of the deficit irrigated field for, respectively, 2017 and 2018. Graphs 4.11(c) and 4.11(d) show $T_o$ plots in 2018 of the fully irrigated field, respectively, 2017 and 2018.

### 4.3.3 Linear Models for $T_o$ based on LAI range

Equation 4.3 show the family of linear models for $T_o$ based, respectively, on the following range of LAI values.

$$T_o = \begin{cases} -8.742 \cdot f_c + 0.571 \cdot T_a + 0.529 \cdot T_s + 0.806 \cdot r_p + 3.295, \;\; 0.85 \leq LAI \leq 1.50 \\ -9.168 \cdot f_c + 0.485 \cdot T_a + 0.575 \cdot T_s - 0.160 \cdot r_p + 6.491, \;\; 1.50 < LAI \leq 2.50 \\ 4.708 \cdot f_c + 0.350 \cdot T_a + 0.580 \cdot T_s + 0.086 \cdot r_p, \;\; 2.50 < LAI \leq 3.50 \\ -1.912 \cdot f_c + 0.443 \cdot T_a + 0.509 \cdot T_s + 0.115 \cdot r_p + 5.014, 3.50 < LAI \leq 5.00 \end{cases} \tag{4.3}$$

Tables 4.24 and 4.25 show, respectively, the statistics of the multiple linear regression analysis for each $T_o$ model and the model quality assessment. Figure 4.12 shows the Inverted LAS $T_o$ vs. Estimated $T_o$ plot using the linear models developed based on LAI range of values. Table 4.26 presents the model performance under difference scenarios of VPD and wind speed.

The linear models for $T_o$ based on different ranges of LAI values seem to have better agreement of under water stress conditions when the combined 2017-2018 data are considered. Better overall estimated $T_o$ values are also highlighted in figure 4.12 in which it is possible to identify approximation between the plotted points to the 1:1 line on graphs 4.12(a) and 4.12(b). That could be explained due to the fact that the models based on LAI range tend to assimilate better the conditions of when the surface biomass is under water stress conditions. As the water content within the root zone decreases below management allowed depletion (MAD), the corn leaves adapt themselves to minimize the LAI surface area exposed to radiation, in which it decreases the amount of biomass that potentially would be interacting with the air flowing above the surface, which it seems to be better represented when the models are incorporating those differences based on LAI range.

The regression statistics show that as the range of LAI increases, the goodness of fit of the linear models slightly decreases as the $R^2$ values progressively get smaller. However, regarding

RMSE values, the sub-equations for LAI range 1.50 to 2.50 and 3.50 to 5.00 seemed to have less spread of error (RMSE values less than 1 °C) than the other LAI ranges sub-equations. That is due to the fact that different growth stages and biomass development affect the processes that derive the occurrence of $T_o$ by changing the aerodynamic height. Regarding the $r_p$ variable, the p-values on all 4 linear $T_o$ models indicate that there is no strong statistical evidence that the respective estimated coefficients are a good representation of the relationship between $T_o$ and $r_p$.

The linear $T_o$ models based on LAI range seems to perform better on deficit irrigated field when different scenarios of VPD and wind speed are considered as indicated by high values of $dr_r$. For the deficit irrigated treatment, conditions of low VPD and high wind speed and high VPD and low wind speed provided RMSE less than 1 °C. For the fully irrigated field, the model seems to provide better agreement under more humid atmospheric conditions (VPD $<$ 2.5 kPa) by having significant larger $d_r$ than the scenarios in which the nearby atmosphere gets drier in a similar behavior when the general linear $T_o$ model was assessed.

**Table 4.24:** Multiple linear regression statistics of linear $T_o$ models based on LAI range (equation 4.3).

| LAI Range | $R^2$ | MBE (°C) | RMSE (°C) | Coefficient | Variable | Estimate | SE | Test Statistic | p-value |
|---|---|---|---|---|---|---|---|---|---|
| 0.85 to 1.50 | 0.99 | 0.01 | 1.03 | $a_1$ | $f_c$ | -8.7422 | 4.364 | -2.0032 | 0.051793 |
| | | | | $a_2$ | $T_a$ | 0.57085 | 0.086635 | 6.5891 | $6.2888 \cdot 10^{-8}$ |
| | | | | $a_3$ | $T_s$ | 0.52863 | 0.063353 | 8.3443 | $2.2416 \cdot 10^{-10}$ |
| | | | | $a_4$ | $r_p$ | 0.80612 | 0.88774 | 0.90806 | 0.36915 |
| | | | | $a_5$ | - | 3.2946 | 1.08 | 3.0505 | 0.0039941 |
| 1.50 to 2.50 | 0.99 | -0.02 | 0.66 | $a_1$ | $f_c$ | -9.1683 | 4.3393 | -2.1128 | 0.037655 |
| | | | | $a_2$ | $T_a$ | 0.48528 | 0.037041 | 13.101 | $8.3096 \cdot 10^{-22}$ |
| | | | | $a_3$ | $T_s$ | 0.57538 | 0.039012 | 14.749 | $8.7844 \cdot 10^{-25}$ |
| | | | | $a_4$ | $r_p$ | -0.15973 | 0.41079 | -0.38884 | 0.6984 |
| | | | | $a_5$ | - | 6.4914 | 2.7504 | 2.3602 | 0.020641 |
| 2.50 to 3.50 | 0.96 | 0.02 | 1.32 | $a_1$ | $f_c$ | 4.708 | 0.81461 | 5.7794 | $6.529 \cdot 10^{-8}$ |
| | | | | $a_2$ | $T_a$ | 0.34974 | 0.055751 | 6.2733 | $6.419 \cdot 10^{-9}$ |
| | | | | $a_3$ | $T_s$ | 0.57979 | 0.047636 | 12.171 | $2.0971 \cdot 10^{-22}$ |
| | | | | $a_4$ | $r_p$ | 0.086269 | 0.66474 | 0.12978 | 0.89697 |
| 3.50 to 5.00 | 0.94 | 0.00 | 0.93 | $a_1$ | $f_c$ | -1.9117 | 1.3196 | -1.4487 | 0.14896 |
| | | | | $a_2$ | $T_a$ | 0.44261 | 0.033622 | 13.164 | $5.5297 \cdot 10^{-29}$ |
| | | | | $a_3$ | $T_s$ | 0.50921 | 0.035171 | 14.478 | $4.6854 \cdot 10^{-33}$ |
| | | | | $a_4$ | $r_p$ | 0.1151 | 0.26465 | 0.43493 | 0.66408 |
| | | | | $a_5$ | - | 5.0144 | 1.3288 | 3.7737 | 0.00021138 |

**Table 4.25:** Statistics model quality assessment of the linear $T_o$ models based on LAI range (equation 4.3).

| Treatment Plot | Year | n | MBE | RMSE | Pearson's R | $d_r$ |
|---|---|---|---|---|---|---|
| [-] | [-] | [-] | [°C] | [°C] | [-] | [-] |
| Deficit Irrigated | 2017 | 33 | -0.54 | 1.37 | 0.96 | 0.85 |
| | 2018 | 135 | 0.04 | 0.94 | 0.99 | 0.93 |
| | 2017 and 2018 | 168 | -0.07 | 1.04 | 0.99 | 0.92 |
| Fully Irrigated | 2017 | 107 | 0.13 | 1.11 | 0.96 | 0.87 |
| | 2018 | 144 | 0.05 | 1.10 | 0.98 | 0.90 |
| | 2017 and 2018 | 251 | 0.08 | 1.10 | 0.98 | 0.89 |

**Table 4.26:** Model quality assessment of the linear $T_o$ models based on LAI range (equation 4.3) regarding different VPD and wind speed conditions for LIRF 201-2018 combined data.

| Treatment site | VPD range | Wind speed range | n | MBE | RMSE | Pearson's R | $d_r$ |
|---|---|---|---|---|---|---|---|
| [-] | [kPa] | [m/s] | [-] | [°C] | [°C] | [-] | [-] |
| Deficit Irrigated Field | VPD $< 2.5$ | u $< 2$ | 84 | 0.26 | 1.20 | 0.98 | 0.91 |
| | | u $> 2$ | 36 | -0.24 | 0.78 | 0.99 | 0.92 |
| | VPD $> 2.5$ | u $< 2$ | 34 | 0.07 | 0.76 | 0.97 | 0.85 |
| | | u $> 2$ | 14 | 0.69 | 1.19 | 0.96 | 0.85 |
| Fully Irrigated Field | VPD $< 2.5$ | u $< 2$ | 108 | 0.11 | 1.00 | 0.98 | 0.90 |
| | | u $> 2$ | 53 | 0.30 | 0.83 | 0.97 | 0.88 |
| | VPD $> 2.5$ | u $< 2$ | 64 | 0.06 | 1.46 | 0.84 | 0.70 |
| | | u $> 2$ | 26 | -0.41 | 1.00 | 0.87 | 0.76 |

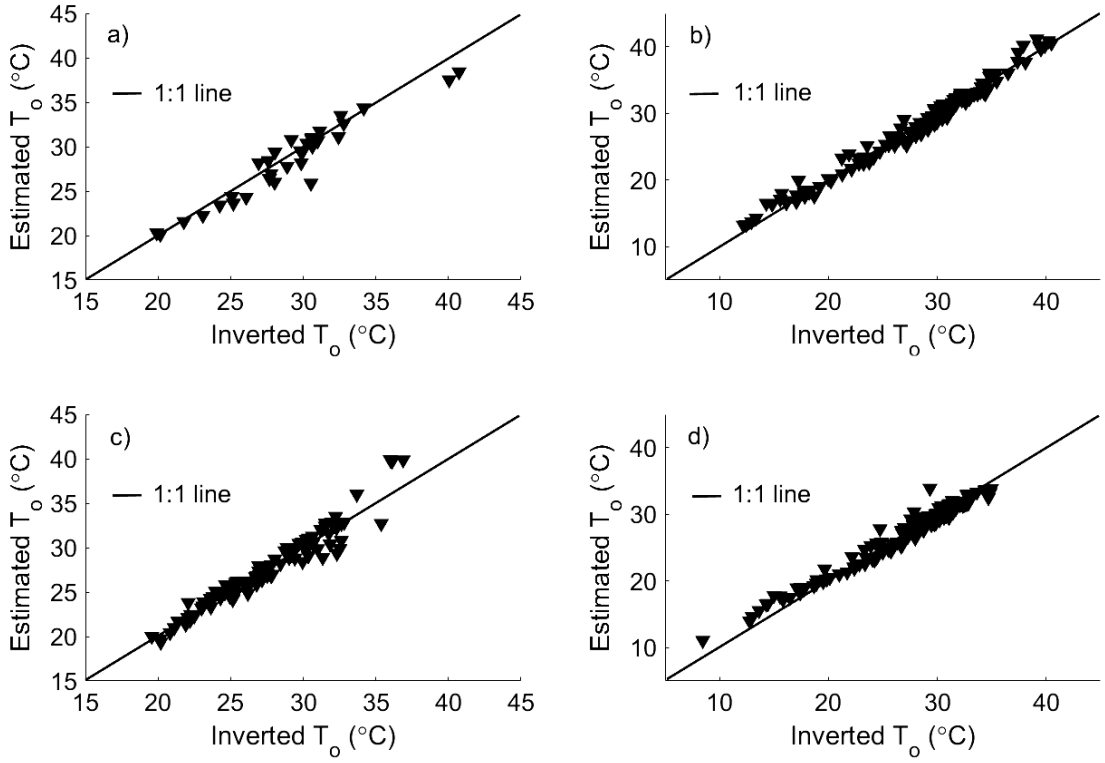


**Figure 4.12:** Inverted LAS $T_o$ vs. Estimated $T_o$ for different treatment sites in 2017 and 2018 regarding the linear $T_o$ models based on LAI range (equation 4.3). Graphs 4.12(a) and 4.12(b) show $T_o$ plots of the deficit irrigated field for, respectively, 2017 and 2018. Graphs 4.12(c) and 4.12(d) show $T_o$ plots of the fully irrigated field for, respectively, 2017 and 2018.

### 4.3.4 Non-Linear Models for $T_o$ based on LAI range

Equation 4.4 shows the non-linear models for $T_o$ based on the following range of LAI values.

$$T_o = \begin{cases} T_a + 1.928 \cdot ln|T_s - T_a| + 0.188 \cdot \dfrac{r_p}{f_c} + 2.835, \;\; 0.85 \leq LAI \leq 1.50 \\ \\ T_a + 1.059 \cdot ln|T_s - T_a| - 0.455 \cdot \dfrac{r_p}{f_c} + 2.415, \;\; 1.50 < LAI \leq 2.50 \\ \\ T_a + 1.231 \cdot ln|T_s - T_a| + 1.107 \cdot \dfrac{r_p}{f_c} + 2.065, \;\; 2.50 < LAI \leq 3.50 \\ \\ T_a + 0.618 \cdot ln|T_s - T_a| - 0.130 \cdot \dfrac{r_p}{f_c} + 2.624, 3.50 < LAI \leq 5.00 \end{cases} \tag{4.4}$$

Tables 4.27 and 4.28 show, respectively, the statistics of the non-linear regression analysis for each non-linear $T_o$ model and the model quality assessment. Figure 4.13 shows the Inverted LAS $T_o$ vs. Estimated $T_o$ plot using the non-linear models developed based on LAI range of values. Table 4.29 presents the model performance under difference scenarios of VPD and wind speed.

The non-linear $T_o$ models based on LAI range of values follow the trend of performing better under water stressed conditions when the analysis is done by combining all data from 2017 and 2018. That reassures the same observation based on the linear $T_o$ models for different LAI conditions. However, when compared with the linear $T_o$ models, the non-linear approach does not perform the same, which it might be related to the same reasons as why the general non-linear model performed worse than its counterpart linear model.

Regarding the scenarios of VPD and wind speed range, the non-linear $T_o$ models performed better under more humid atmospheric conditions regardless of wind speed range on the fully irrigated field. When there is induced water stress, the models had a better agreement with the inverted LAS $T_o$ for conditions when wind speed is less than 2 m/s, regardless the VPD conditions of the atmosphere.

**Table 4.27:** Non-linear regression statistics of $T_o$ models based on LAI range (equation 4.4).

| LAI Range | $R^2$ | Coefficient | Estimate | SE | Test Statistic | p-value |
|---|---|---|---|---|---|---|
| 0.85 to 1.50 | 0.98 | $p_1$ | 1.928 | 0.2012 | 9.5816 | $3.1078 \cdot 10^{-12}$ |
| | | $p_2$ | 0.188 | 0.3529 | 0.5328 | 0.5969 |
| | | $p_3$ | 2.835 | 0.4588 | 6.1777 | $2.0164 \cdot 10^{-7}$ |
| 1.50 to 2.50 | 0.98 | $p_1$ | 1.059 | 0.1335 | 7.931 | $8.3346 \cdot 10^{-12}$ |
| | | $p_2$ | -0.455 | 0.3743 | -1.2156 | 0.2276 |
| | | $p_3$ | 2.415 | 0.2074 | 11.643 | $3.2763 \cdot 10^{-19}$ |
| 2.50 to 3.50 | 0.94 | $p_1$ | 1.231 | 0.1564 | 7.8719 | $1.9357 \cdot 10^{-11}$ |
| | | $p_2$ | 1.107 | 0.6744 | 1.6415 | 0.1048 |
| | | $p_3$ | 2.065 | 0.3470 | 5.9526 | $7.6207 \cdot 10^{-8}$ |
| 3.50 to 5.00 | 0.86 | $p_1$ | 0.618 | 0.0714 | 8.6680 | $1.3655 \cdot 10^{-15}$ |
| | | $p_2$ | -0.130 | 0.3405 | -0.3829 | 0.7022 |
| | | $p_3$ | 2.624 | 0.1503 | 17.465 | $2.2415 \cdot 10^{-42}$ |

**Table 4.28:** Statistics model quality assessment of the non-linear $T_o$ models based on LAI range (equation 4.4).

| Treatment Plot | Year | n | MBE | RMSE | Pearson's R | $d_r$ |
|---|---|---|---|---|---|---|
| [-] | [-] | [-] | [°C] | [°C] | [-] | [-] |
| Deficit Irrigated | 2017 | 33 | -0.83 | 1.73 | 0.94 | 0.81 |
| | 2018 | 135 | -0.26 | 1.13 | 0.99 | 0.92 |
| | 2017 and 2018 | 168 | -0.37 | 1.27 | 0.98 | 0.91 |
| Fully Irrigated | 2017 | 107 | 0.54 | 1.43 | 0.97 | 0.81 |
| | 2018 | 144 | 0.03 | 1.18 | 0.98 | 0.89 |
| | 2017 and 2018 | 251 | 0.25 | 1.30 | 0.97 | 0.86 |

**Table 4.29:** Model quality assessment of the non-linear $T_o$ models based on LAI range (equation 4.4) regarding different VPD and wind speed conditions for LIRF 201-2018 combined data.

| Treatment site | VPD range | Wind speed range | n | MBE | RMSE | Pearson's R | $d_r$ |
|---|---|---|---|---|---|---|---|
| [-] | [kPa] | [m/s] | [-] | [°C] | [°C] | [-] | [-] |
| Deficit Irrigated Field | VPD $< 2.5$ | u $< 2$ | 84 | -0.49 | 1.34 | 0.98 | 0.89 |
| | | u $> 2$ | 36 | -0.56 | 1.38 | 0.97 | 0.86 |
| | VPD $> 2.5$ | u $< 2$ | 34 | -0.18 | 0.92 | 0.95 | 0.83 |
| | | u $> 2$ | 14 | 0.32 | 1.33 | 0.86 | 0.61 |
| Fully Irrigated Field | VPD $< 2.5$ | u $< 2$ | 108 | -0.22 | 1.19 | 0.97 | 0.87 |
| | | u $> 2$ | 53 | -0.11 | 0.89 | 0.97 | 0.87 |
| | VPD $> 2.5$ | u $< 2$ | 64 | 1.02 | 1.68 | 0.86 | 0.61 |
| | | u $> 2$ | 26 | 1.00 | 1.34 | 0.90 | 0.66 |

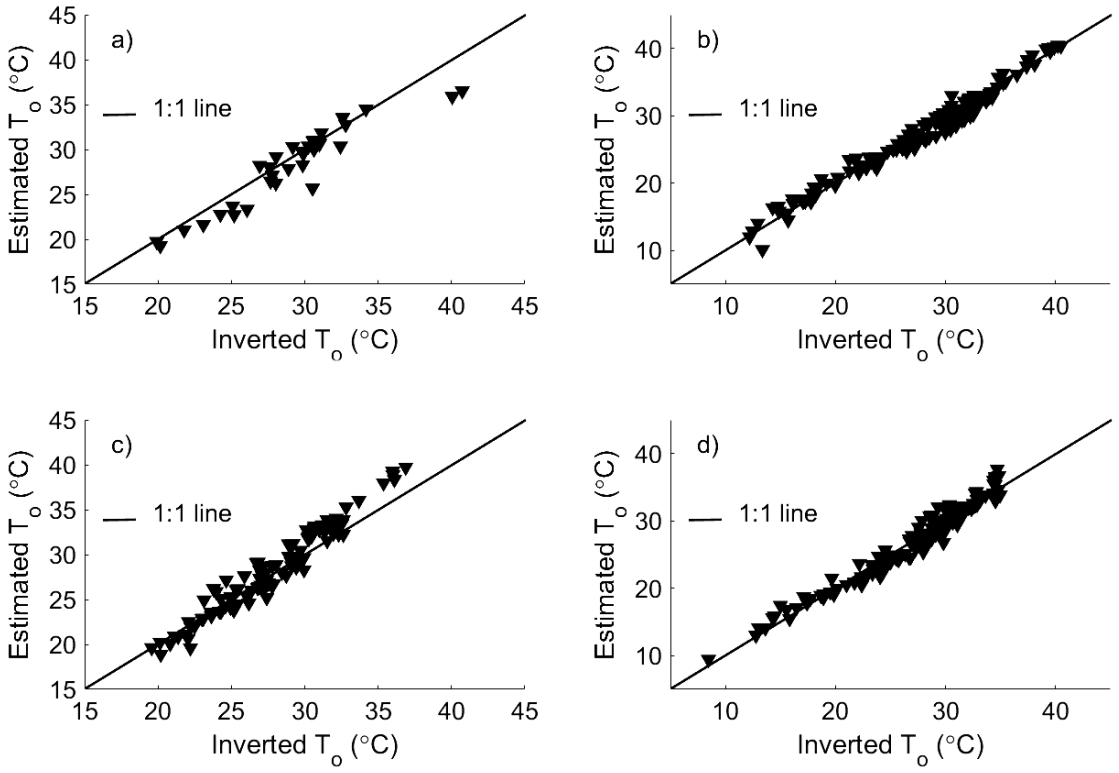


**Figure 4.13:** Inverted LAS $T_o$ vs. Estimated $T_o$ for different treatment sites in 2017 and 2018 regarding non-linear $T_o$ models based on LAI range (equation 4.4). Graphs 4.13(a) and 4.13(b) show $T_o$ plots of the deficit irrigated field for, respectively, 2017 and 2018. Graphs 4.13(c) and 4.13(d) show $T_o$ plots of the fully irrigated field for, respectively, 2017 and 2018.

### 4.3.5 $T_o$ Models Analysis Regarding Corn Row Layout at LIRF

Tables 4.30 and 4.31 show, respectively, the analysis of $T_o$ model performance regarding crop row layout and wind direction using the linear $T_o$ models based on LAI range and general linear $T_o$ model.

Tables 4.32 and 4.33 show, respectively, the analysis of $T_o$ model performance regarding crop row layout and wind direction using the non-linear $T_o$ models based on LAI range and general non-linear $T_o$ model.

It is possible to infer from all the model analysis that when the wind speed direction is almost parallel to the corn row layout, the model for $T_o$ perform sightly better than when the wind is

crossing the field and interacting with more canopy elements within a given angle. That is true when the combined 2017-2018 data of both fields are analyzed based on the $d_r$ values being larger for $0 < \tau < 0.25$. That is in agreement with the idea that there is more resistance to heat transfer and as the wind crosses the field on directions that allow more biomass elements to increase the mixing of air within the top canopy layer. That is valid due to the fact that when the wind direction is near parallel conditions to the corn row, the $r_p$ term tends to zero indicating the the air flowing above the surface has less interference on its trajectory due to the canopy elements and that the aerodynamic surface temperature is predominantly influenced by the kinetic energy stage of the wind as it interacts with surface.

**Table 4.30:** Model quality assessment of the group of linear $T_o$ models based on LAI range (equation 4.3) regarding crop layout and wind direction.

| Treatment Plot | $\tau$ range of values | n | MBE | RMSE | Pearson's R | $d_r$ |
|---|---|---|---|---|---|---|
| [-] | [-] | [-] | [°C] | [°C] | [-] | [-] |
| Deficit Irrigated | $0.00 < \tau < 0.25$ | 63 | 0.01 | 0.93 | 0.99 | 0.94 |
| | $0.25 < \tau < 0.50$ | 90 | -0.18 | 1.11 | 0.98 | 0.91 |
| | $0.50 < \tau < 0.75$ | 15 | 0.20 | 1.06 | 0.98 | 0.90 |
| Fully Irrigated | $0.00 < \tau < 0.25$ | 82 | 0.12 | 1.13 | 0.98 | 0.90 |
| | $0.25 < \tau < 0.50$ | 128 | 0.02 | 1.12 | 0.97 | 0.88 |
| | $0.50 < \tau < 0.75$ | 41 | 0.21 | 1.05 | 0.97 | 0.87 |

**Table 4.31:** Model quality assessment of the general linear $T_o$ model (equation 4.1) regarding crop layout and wind direction.

| Treatment Plot | $\tau$ range of values | n | MBE | RMSE | Pearson's R | $d_r$ |
|---|---|---|---|---|---|---|
| [-] | [-] | [-] | [°C] | [°C] | [-] | [-] |
| Deficit Irrigated | $0.00 < \tau < 0.25$ | 63 | -0.32 | 0.99 | 0.99 | 0.93 |
| | $0.25 < \tau < 0.50$ | 90 | -0.48 | 1.20 | 0.98 | 0.91 |
| | $0.50 < \tau < 0.75$ | 15 | 0.05 | 1.24 | 0.97 | 0.88 |
| Fully Irrigated | $0.00 < \tau < 0.25$ | 82 | 0.06 | 1.08 | 0.98 | 0.91 |
| | $0.25 < \tau < 0.50$ | 128 | 0.18 | 1.16 | 0.97 | 0.89 |
| | $0.50 < \tau < 0.75$ | 41 | 0.38 | 1.17 | 0.97 | 0.86 |

**Table 4.32:** Model quality assessment of the group of non-linear $T_o$ models based on LAI range (equation 4.4) regarding crop layout and wind direction.

| Treatment Plot | $\tau$ range of values | n | MBE | RMSE | Pearson's R | $d_r$ |
|---|---|---|---|---|---|---|
| [-] | [-] | [-] | [°C] | [°C] | [-] | [-] |
| Deficit Irrigated | $0.00 < \tau < 0.25$ | 63 | -0.25 | 1.13 | 0.99 | 0.93 |
| | $0.25 < \tau < 0.50$ | 90 | -0.49 | 1.38 | 0.98 | 0.89 |
| | $0.50 < \tau < 0.75$ | 15 | -0.13 | 1.15 | 0.98 | 0.89 |
| Fully Irrigated | $0.00 < \tau < 0.25$ | 82 | 0.20 | 1.21 | 0.98 | 0.89 |
| | $0.25 < \tau < 0.50$ | 128 | 0.21 | 1.31 | 0.97 | 0.85 |
| | $0.50 < \tau < 0.75$ | 41 | 0.52 | 1.46 | 0.96 | 0.78 |

**Table 4.33:** Model quality assessment of the general non-linear $T_o$ model (equation 4.2) regarding crop layout and wind direction.

| Treatment Plot | $\tau$ range of values | n | MBE | RMSE | Pearson's R | $d_r$ |
|---|---|---|---|---|---|---|
| [-] | [-] | [-] | [°C] | [°C] | [-] | [-] |
| Deficit Irrigated | $0.00 < \tau < 0.25$ | 63 | -0.55 | 1.46 | 0.98 | 0.90 |
| | $0.25 < \tau < 0.50$ | 90 | -0.72 | 1.60 | 0.97 | 0.87 |
| | $0.50 < \tau < 0.75$ | 15 | -0.11 | 1.17 | 0.98 | 0.89 |
| Fully Irrigated | $0.00 < \tau < 0.25$ | 82 | 0.34 | 1.37 | 0.97 | 0.88 |
| | $0.25 < \tau < 0.50$ | 128 | 0.37 | 1.46 | 0.96 | 0.84 |
| | $0.50 < \tau < 0.75$ | 41 | 0.71 | 1.66 | 0.95 | 0.75 |

### 4.3.6 Quality Assessment of $T_o$ Results Regarding Proposed and Some Published Models using SMEX02 IOWA Data

Tables 4.34 and 4.35 show, respectively, the statistical analysis of the $T_o$ model quality assessment for energy balance closure and non-closure conditions, among the proposed models for $T_o$ and the ones provided by Chavez et al. (2005) and Chehbouni et al. (1996).

Figures 4.14 and 4.15 show, respectively, the plots of Estimated $T_o$ vs. Inverted EC $T_o$ for the evaluation of the six $T_o$ models types presented under energy balance non-closure and closure conditions.

When comparing all 6 $T_o$ models evaluated, the proposed linear $T_o$ models based on LAI range seem to perform better than all other models tested based on small RMSE and high $d_r$ when both surface energy balance closure and non-closure conditions were evaluated. However, the MBE value is larger than for the analysis using LIRF data. That overestimation is potentially due to differences in biomass development incorporate through LAI values, corn species, soil water deficit

and climate conditions between Iowa and LIRF fields.

The proposed non-linear approaches do not perform well when compared with all other models tested due to having the lowest $d_r$ values. That would be expected since the performance of the models using LIRF data also did not excel the performance of the linear models proposed. It seems that both general linear $T_o$ model and the ones based on a given LAI range had satisfactory performances even under different climate conditions. That could be explained based on the direct linear statistical association between $T_o$, $T_a$, and $T_s$, expressed by the significant p-values obtained when deriving the fitter coefficients on the respective empirical models for $T_o$. The published models did not performed better than the proposed linear model types based on differences on how the approaches where derived and the conditions of their applicability. The model by Chehbouni et al. (1996) was initially developed for heterogeneous surface types that are more associated to bushes and similar desert vegetation. Chavez et al. (2005) model used airborne based surface reflectance and temperature data and was developed for corn. However, the goodness of fit of the model ($R^2 = 0.77$) was lower than the proposed linear $T_o$ model types, which indicates that the performance would be passive of introducing more variability into the comparison between estimated $T_o$ and inverted $T_o$.

**Table 4.34:** Model quality assessment of $T_o$ models under eddy covariance energy balance non-closure conditions using SMEX02 IOWA data.

| $T_o$ Model | Category | n | MBE | RMSE | Pearson's R | $d_r$ |
|---|---|---|---|---|---|---|
| [-] | [-] | [-] | [°C] | [°C] | [-] | [-] |
| Linear $T_o$ models for given LAI range | Proposed Model | 235 | 0.68 | 1.13 | 0.95 | 0.78 |
| General linear $T_o$ model | Proposed Model | 235 | 0.99 | 1.33 | 0.96 | 0.74 |
| Non-linear $T_o$ models for given LAI range | Proposed Model | 235 | 1.24 | 2.16 | 0.78 | 0.55 |
| General non-linear $T_o$ model | Proposed Model | 235 | -1.74 | 2.21 | 0.85 | 0.52 |
| Chehbouni et al. (1996) | Published Model | 235 | 0.37 | 2.25 | 0.65 | 0.63 |
| Chavez et al. (2005) | Published Model | 235 | -1.66 | 1.81 | 0.96 | 0.59 |

**Table 4.35:** Model quality assessment of $T_o$ models under eddy covariance energy balance closure conditions using SMEX02 IOWA data.

| $T_o$ Model | Category | n | MBE | RMSE | Pearson's R | $d_r$ |
|---|---|---|---|---|---|---|
| [-] | [-] | [-] | [°C] | [°C] | [-] | [-] |
| Linear $T_o$ models for given LAI range | Proposed Model | 253 | 0.71 | 1.15 | 0.96 | 0.80 |
| General linear $T_o$ model | Proposed Model | 253 | 1.03 | 1.32 | 0.97 | 0.77 |
| Non-linear $T_o$ models for given LAI range | Proposed Model | 253 | 1.65 | 2.39 | 0.82 | 0.57 |
| General non-linear $T_o$ model | Proposed Model | 253 | -1.94 | 2.45 | 0.87 | 0.55 |
| Chehbouni et al. (1996) | Published Model | 253 | 0.70 | 2.53 | 0.66 | 0.64 |
| Chavez et al. (2005) | Published Model | 253 | -1.60 | 1.76 | 0.97 | 0.66 |

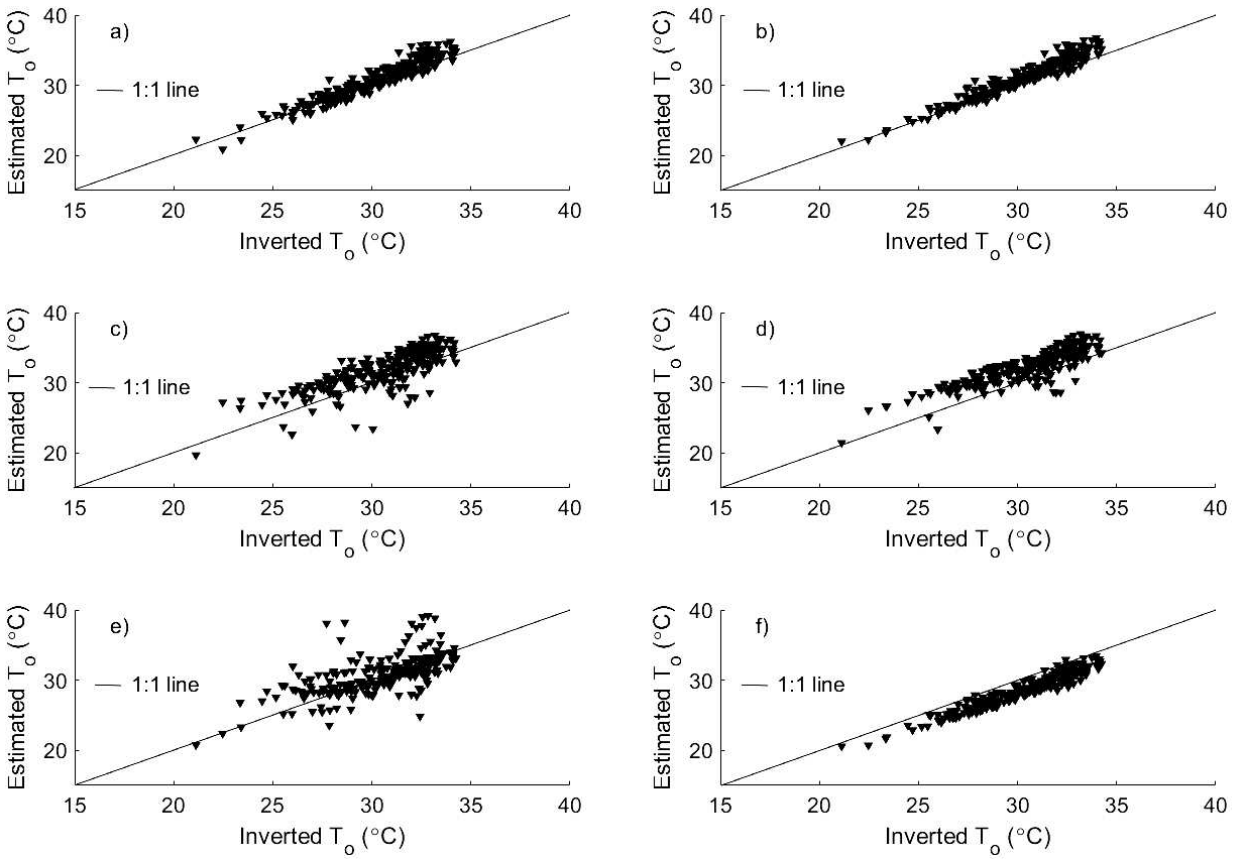


**Figure 4.14:** Inverted EC $T_o$ vs. Estimated $T_o$ for SMEX02 IOWA data set proposed and some published models under surface energy balance non-closure conditions. Graphs 4.14(a) and 4.14(b) show $T_o$ plots for, respectively, the linear $T_o$ models for a given LAI range (equation 4.3) and general linear $T_o$ model (equation 4.1). Graphs 4.14(c) and 4.14(d) show $T_o$ plots for, respectively, the non-linear $T_o$ models for a given LAI range (equation 4.4) and general non-linear $T_o$ model (equation 4.2). Graphs 4.14(e) and 4.14(f) show $T_o$ plots for, respectively, the models developed by Chehbouni et al. (1996) and Chavez et al. (2005). All plots are for the Inverted EC $T_o$ under surface energy balance non-closure conditions.

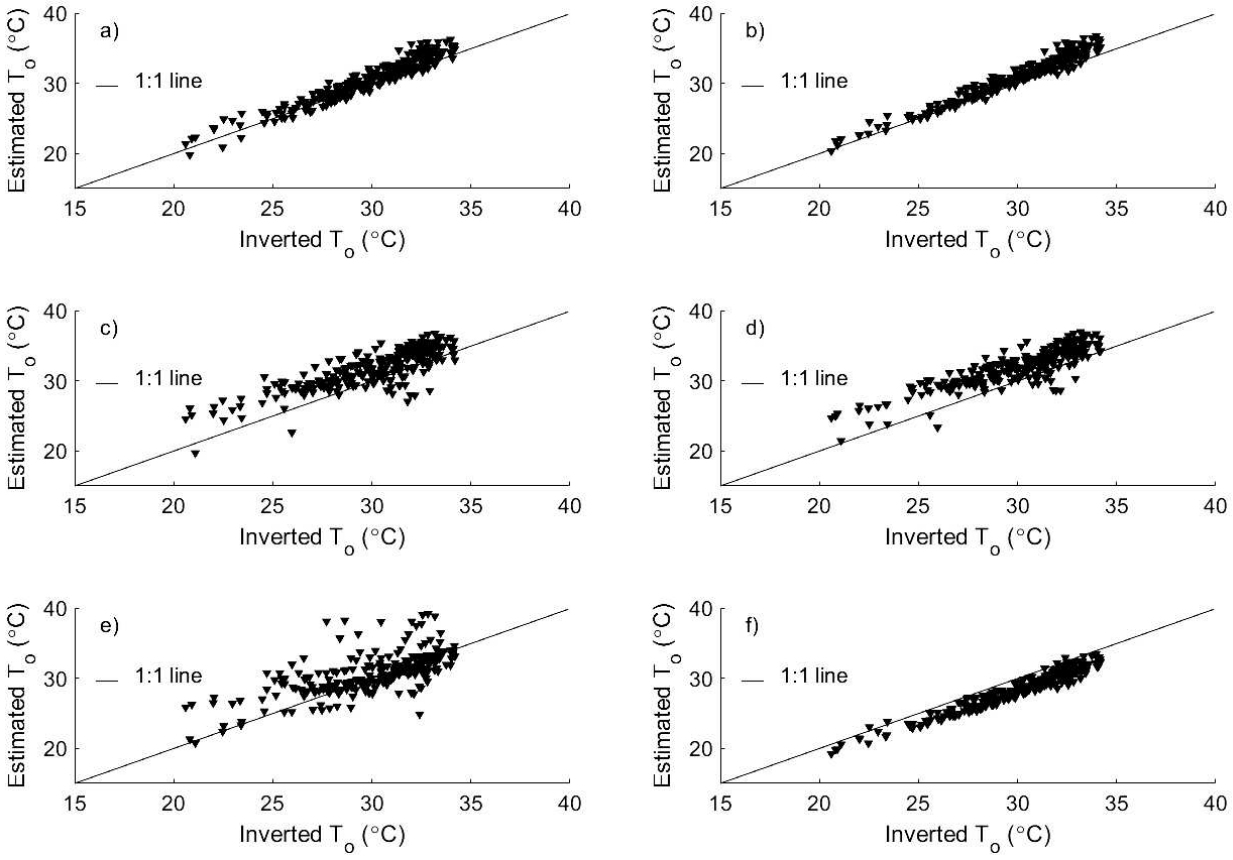


**Figure 4.15:** Inverted EC $T_o$ vs. Estimated $T_o$ for SMEX02 IOWA data set proposed and some published models under surface energy balance non-closure conditions. Graphs 4.15(a) and 4.15(b) show $T_o$ plots for, respectively, the linear $T_o$ models for a given LAI range (equation 4.3) and general linear $T_o$ model (equation 4.1). Graphs 4.15(c) and 4.15(d) show $T_o$ plots for, respectively, the non-linear $T_o$ models for a given LAI range (equation 4.4) and general non-linear $T_o$ model (equation 4.2). Graphs 4.15(e) and 4.15(f) show $T_o$ plots for, respectively, the models developed by Chehbouni et al. (1996) and Chavez et al. (2005). All plots are for the Inverted EC $T_o$ under surface energy balance closure conditions.

### 4.3.7 Quality Assessment of $T_o$ Results Regarding Proposed and Some Published Models using CSU AVRC Data

Table 4.36 shows the statistical analysis of the $T_o$ model quality assessment for the proposed models for $T_o$ and the ones developed by Chavez et al. (2005) and Chehbouni et al. (1996). Figure 4.16 shows the plots of Estimated $T_o$ vs. Inverted $T_o$ for the evaluation of the six $T_o$ models types.

The general linear $T_o$ model performs better when tested using the Rocky Ford, CO data set. That is indicated by highest $d_r$ value. The proposed non-linear approaches provided better results than when tested using the SMEX02 Iowa data set. That could be due to the fact that Rocky Ford has a similar climate conditions to Greeley, which allows the models to have better performance under similar atmospheric conditions of the original data used to develop the $T_o$ models. The published models by Chehbouni et al. (1996) and Chavez et al. (2005) had significant underestimation of $T_o$ values as well as low values of $d_r$.

The data set from CSU ARVC has some limitations on the analysis due to the fact that the measured sensible heat flux was obtained from solving the energy balance equation for H. That is as effective and accurate when all measured terms ($R_n$, G, and LE) are well determined. From the data given, the soil heat flux might be introducing bias since it was assumed that the heat storage at the top soil is approximately equal to the soil heat flux plate readings, which limits the analysis for determining both sensible heat flux and, consequently, inverted $T_o$.

From all the analysis of $T_o$, the linear model types for the aerodynamic surface temperature are performing better in all data sets than the non-linear proposed approaches and the published models. Among the general linear $T_o$ model and linear $T_o$ models for given LAI range, the latter has been more reliable for conditions of no water stress treatments. The breakdown of different linear equations according different stages of crop biomass growth seems to be effective when the surface suffers more severe modifications throughout the growing season.

**Table 4.36:** Model quality assessment of $T_o$ models using CSU ARVC data.

| $T_o$ Model | Category | n | MBE | RMSE | Pearson's R | $d_r$ |
|---|---|---|---|---|---|---|
| [-] | [-] | [-] | [°C] | [°C] | [-] | [-] |
| Linear $T_o$ models for given LAI range | Proposed Model | 19 | -0.19 | 1.48 | 0.96 | 0.84 |
| General linear $T_o$ model | Proposed Model | 19 | -0.23 | 1.34 | 0.96 | 0.86 |
| Non-linear $T_o$ models for given LAI range | Proposed Model | 19 | -0.27 | 1.57 | 0.96 | 0.84 |
| General non-linear $T_o$ model | Proposed Model | 19 | -0.20 | 1.56 | 0.96 | 0.83 |
| Chehbouni et al. (1996) | Published Model | 19 | -2.23 | 4.04 | 0.87 | 0.61 |
| Chavez et al. (2005) | Published Model | 19 | -2.00 | 2.51 | 0.96 | 0.74 |

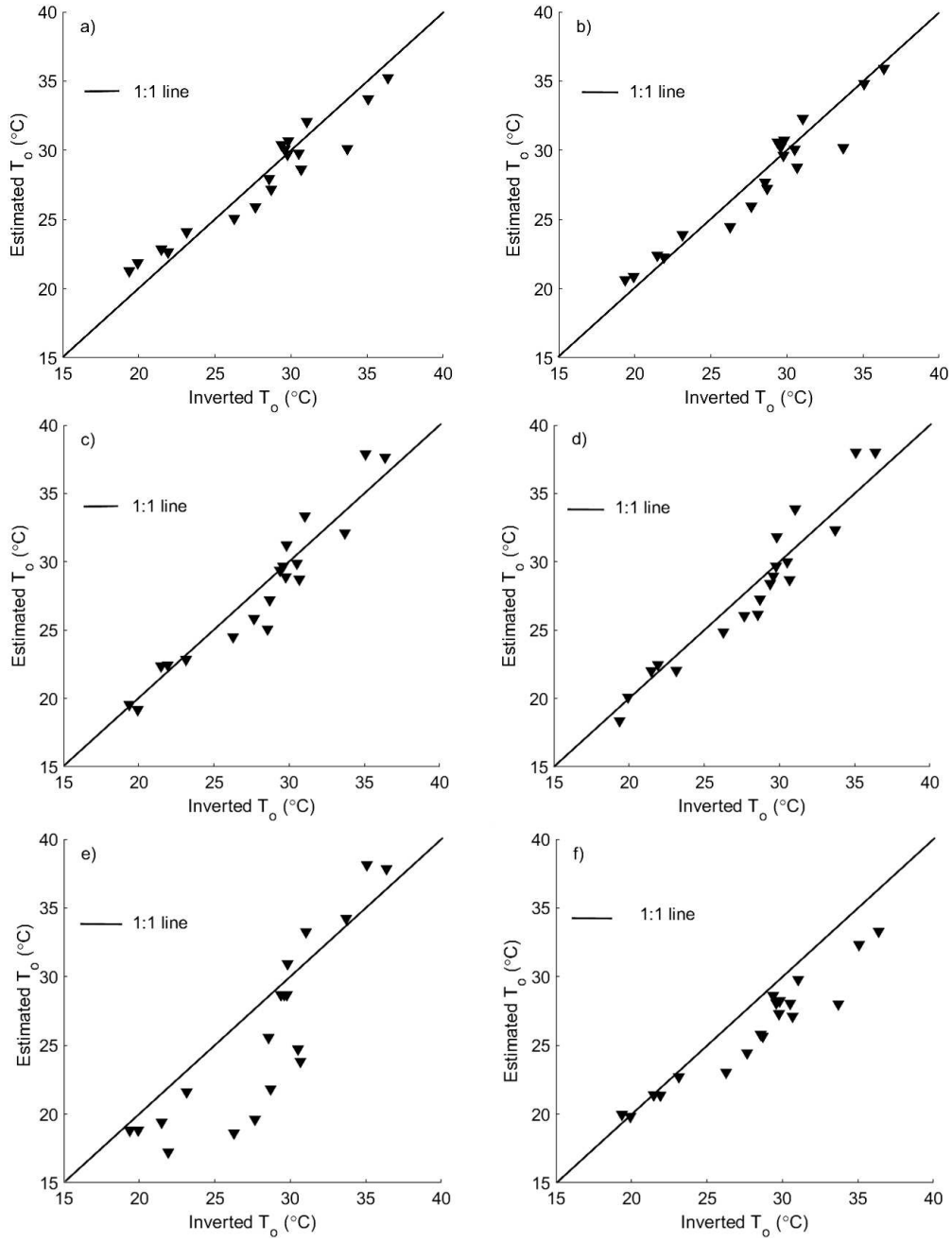


**Figure 4.16:** Graphs 4.16(a) and 4.16(b) show $T_o$ plots for, respectively, the linear $T_o$ models for a given LAI range (equation 4.3) and general linear $T_o$ model (equation 4.1). Graphs 4.16(c) and 4.16(d) show $T_o$ plots for, respectively, the non-linear $T_o$ models for a given LAI range (equation 4.4) and general non-linear $T_o$ model (equation 4.2). Graphs 4.16(e) and 4.16(f) show $T_o$ plots for, respectively, the models developed by Chehbouni et al. (1996) and Chavez et al. (2005).

## 4.4 Sensible Heat Model Results

### 4.4.1 Sensible Heat Model using general linear $T_o$ Model at LIRF

Tables 4.37 and 4.38 show, respectively, the statistical analysis of the H model quality assessment based on the general linear $T_o$ model for the deficit and fully irrigated fields. Figures 4.17 and 4.18 represent, respectively, the plots of Estimated H vs. Measured H for the given model approach for both treatment fields regarding LAS and BR measured H methods.

The H model using the general linear $T_o$ model performs better under fully irrigated conditions in which water stress is minimized or nonexistent. For the deficit treatment plot, the MBE indicates similar underestimation from both LAS and Bowen ratio methods, but with different RMSE values, for the combined 2017-2018 data. The fully irrigated treatment plot had better modeling results from the LAS than the other measured H methods. The Bowen ratio method had some limitations due to sensors resolution capability that might be source of errors on the measurements. From figures 4.17 and 4.18, the data points seem to be closer to the 1:1 line for conditions of no water stress, which indicates that the general linear $T_o$ model provides better results when water stress is not allowed or when adequate irrigation water management is well implemented. Li et al. (2017) has indicated that the uncertainties around sensible heat flux based on the scintillometers approach might be, on average, 0.75 $W/m^2$. Therefore, the uncertainties around the estimated H based on equation 4.1 model is 0.75 $W/m^2 \pm$ 46.4 $W/m^2$.

When comparing 2017 and 2018 for the fully irrigated field, the 2018 year data seems to have better agreement than 2017 on all the measured sensible heat flux methods. Regarding LAS measurements, the year of 2017 may have had bias introduced through the determination of the Bowen ratio as input to calculation of H based on the scintillation theory since $\beta_o$ was determined using measured net radiation and soil heat flux. More variability between the stations of measurements for $R_n$ in 2017 than 2018 may have added more bias on the measured H from LAS.

**Table 4.37:** Model quality assessment of sensible heat flux for deficit irrigated field at LIRF regarding general linear $T_o$ model (equation 4.1).

| Measured H | Year | n | MBE | RMSE | Pearson's R | $d_r$ |
|---|---|---|---|---|---|---|
| [-] | [-] | [-] | $[W/m^2]$ | $[W/m^2]$ | [-] | [-] |
| LAS | 2017 | 7 | 17.9 | 33.8 | 1.00 | 0.87 |
| | 2018 | 55 | -20.7 | 47.7 | 0.85 | 0.74 |
| | 2017-2018 | 62 | -16.4 | 46.4 | 0.88 | 0.77 |
| BR | 2017 | 4 | -20.0 | 22.2 | 0.96 | 0.61 |
| | 2018 | 29 | -12.8 | 64.0 | 0.81 | 0.68 |
| | 2017-2018 | 33 | -13.7 | 66.2 | 0.82 | 0.69 |

**Table 4.38:** Model quality assessment of sensible heat flux for fully irrigated field at LIRF regarding general linear $T_o$ model (equation 4.1).

| Measured H | Year | n | MBE | RMSE | Pearson's R | $d_r$ |
|---|---|---|---|---|---|---|
| [-] | [-] | [-] | $[W/m^2]$ | $[W/m^2]$ | [-] | [-] |
| LAS | 2017 | 41 | 18.0 | 34.8 | 0.80 | 0.60 |
| | 2018 | 79 | -2.1 | 25.6 | 0.93 | 0.83 |
| | 2017-2018 | 120 | 4.8 | 29.1 | 0.90 | 0.80 |
| $EC_s$ | 2017 | 35 | 25.1 | 37.9 | 0.81 | 0.56 |
| $EC_c$ | 2017 | 27 | 31.6 | 45.3 | 0.81 | 0.39 |
| BR | 2018 | 52 | 24.1 | 41.1 | 0.88 | 0.68 |

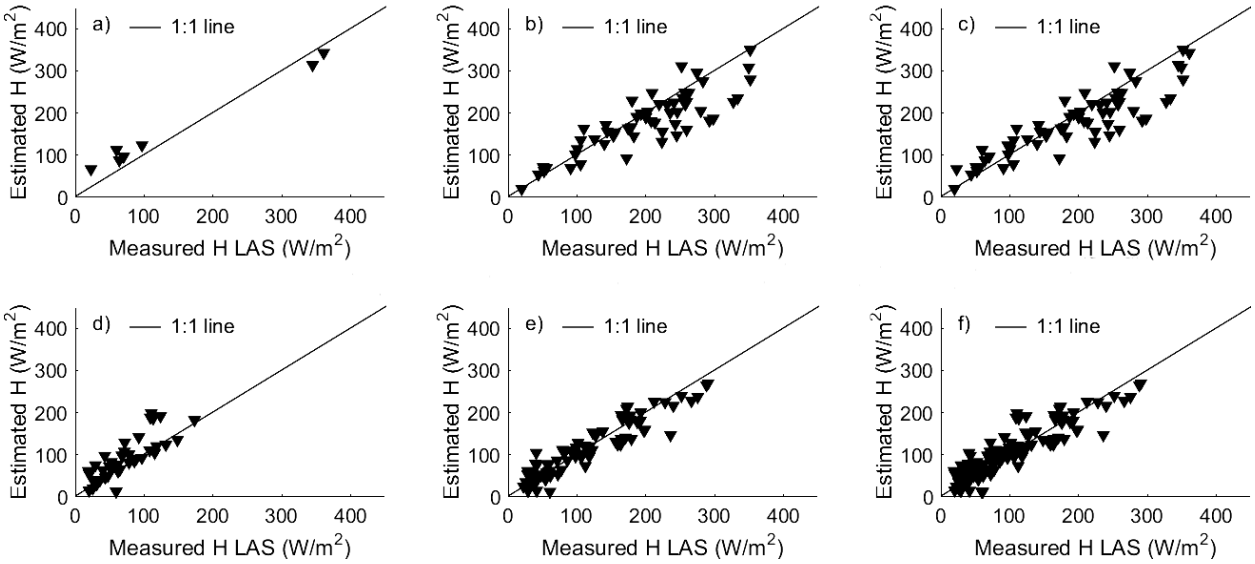


**Figure 4.17:** Measured H vs. Estimated H for deficit and fully irrigated fields at LIRF in 2017 and 2018 based on the general linear $T_o$ model regarding LAS measured sensible heat flux. Graphs 4.17(a), 4.17(b), and 4.17(c) represent, respectively, the Measured LAS H vs. Estimated H for deficit irrigated field in 2017, 2018, and 2017-2018 combined data. Graphs 4.17(d), 4.17(e), and 4.17(f) represent, respectively, the Measured LAS H vs. Estimated H for fully irrigated field in 2017, 2018, and 2017-2018 combined data at LIRF.

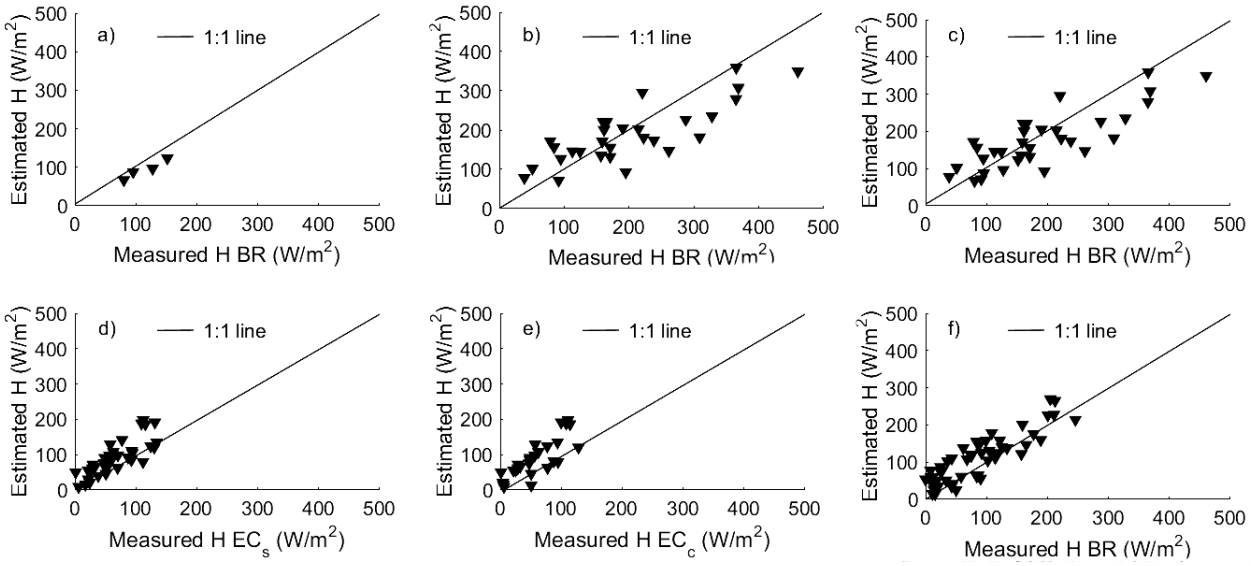


**Figure 4.18:** Measured H vs. Estimated H for deficit and fully irrigated fields at LIRF in 2017 and 2018 based on the general linear $T_o$ model regarding BR and EC measured sensible heat flux. Graphs 4.18(a), 4.18(b), and 4.18(c) represent, respectively, Measured H vs. Estimated H for deficit irrigated field in 2017, 2018, and 2017-2018 combined data regarding Bowen ratio measured H. Graphs 4.18(d) and 4.18(e) indicate Measured H vs. Estimated H for fully irrigated field in 2017 regarding EC measurements. Graph 4.18(f) shows the model comparison for fully irrigated field in 2018 regarding Bowen ratio measured sensible heat flux at LIRF.

### 4.4.2 Sensible Heat Model Assessment using linear $T_o$ Models based on LAI range at LIRF

Tables 4.39 and 4.40 show, respectively, the statistical analysis of the H model quality assessment based on the linear $T_o$ models for the deficit and fully irrigated fields. Figures 4.19 and 4.20 represent, respectively, the plots of Estimated H vs. Measured H for the given model approach for both treatment fields regarding LAS and BR measured H methods.

The estimation of sensible heat flux using equation 4.3 has better agreement with measured data for water stress conditions rather than for the fully irrigated treatment plot. That is based on the capability of the referred $T_o$ model to provide better estimation of the aerodynamic surface temperature when the surface is changing regularly to adapt to stressed conditions of the crop due to soil water content depletion beyond MAD levels. Having models to characterize different biomass

scenarios seem to minimize the MBE and increase models performance on the deficit when analyzing the statistical results using the Bowen ratio sensible heat flux method. The uncertainties around the estimated H based on equation 4.3 $T_o$ model is 0.75 $W/m^2 \pm$ 35.3 $W/m^2$.

From figures 4.19 and 4.20, it is possible to identify that the distribution of point are more aligned to the 1:1 line for the deficit irrigation treatment conditions. The magnitude of both estimated and measured sensible heat fluxes are within expected range of values since the deficit irrigated field provide less biomass and water availability that indicates less transpiration from the canopy and evaporation from the top soil layer. That occurrence of sensible heat flux under those circumstances happens to be at higher values than when the canopy is not under a water stress scenario. That is also evident by analyzing the graphical spread of the points. For the deficit irrigated field, the data seems to be well spread for ranges of H varying from 0 to 450 $W/m^2$ while the fully irrigated field graphs show the points concentrated on the lower section from 0 to 300 $W/m^2$.

**Table 4.39:** Model quality assessment of sensible heat flux for deficit irrigated field at LIRF regarding linear $T_o$ models based on LAI range (equation 4.3).

| Measured H | Year | n | MBE | RMSE | Pearson's R | $d_r$ |
|---|---|---|---|---|---|---|
| [-] | [-] | [-] | [$W/m^2$] | [$W/m^2$] | [-] | [-] |
| LAS | 2017 | 7 | 10.3 | 29.7 | 1.00 | 0.88 |
| | 2018 | 55 | -13.1 | 36.0 | 0.91 | 0.77 |
| | 2017-2018 | 62 | -10.5 | 35.3 | 0.93 | 0.80 |
| BR | 2017 | 4 | 23.0 | 23.4 | 1.00 | 0.43 |
| | 2018 | 29 | 0.7 | 38.1 | 0.94 | 0.81 |
| | 2017-2018 | 33 | 1.1 | 39.3 | 0.95 | 0.82 |

**Table 4.40:** Model quality assessment of sensible heat flux for fully irrigated field at LIRF regarding linear $T_o$ models based on LAI range (equation 4.3).

| Measured H | Year | n | MBE | RMSE | Pearson's R | $d_r$ |
|---|---|---|---|---|---|---|
| [-] | [-] | [-] | $[W/m^2]$ | $[W/m^2]$ | [-] | [-] |
| LAS | 2017 | 41 | 19.0 | 33.7 | 0.83 | 0.59 |
| | 2018 | 79 | -8.7 | 36.9 | 0.87 | 0.76 |
| | 2017-2018 | 120 | 0.8 | 35.9 | 0.85 | 0.74 |
| $EC_s$ | 2017 | 35 | 24.9 | 36.1 | 0.83 | 0.57 |
| $EC_c$ | 2017 | 27 | 28.6 | 47.1 | 0.81 | 0.44 |
| BR | 2018 | 52 | 12.4 | 47.3 | 0.78 | 0.62 |

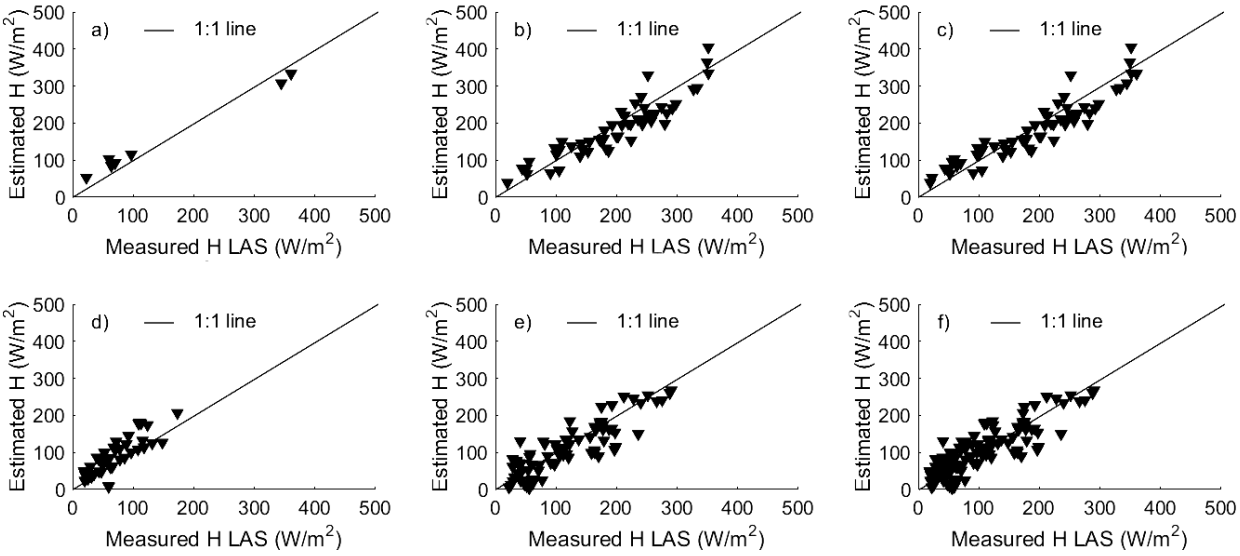


**Figure 4.19:** Measured H vs. Estimated H for deficit and fully irrigated fields at LIRF in 2017 and 2018 regarding the linear $T_o$ models based on LAI range for LAS measured sensible heat flux. Graphs 4.19(a), 4.19(b), and 4.19(c) represent, respectively, the Measured LAS H vs. Estimated H for deficit irrigated field in 2017, 2018, and 2017-2018 combined data. Graphs 4.19(d), 4.19(e), and 4.19(f) represent, respectively, the Measured LAS H vs. Estimated H for fully irrigated field in 2017, 2018, and 2017-2018 combined data at LIRF.

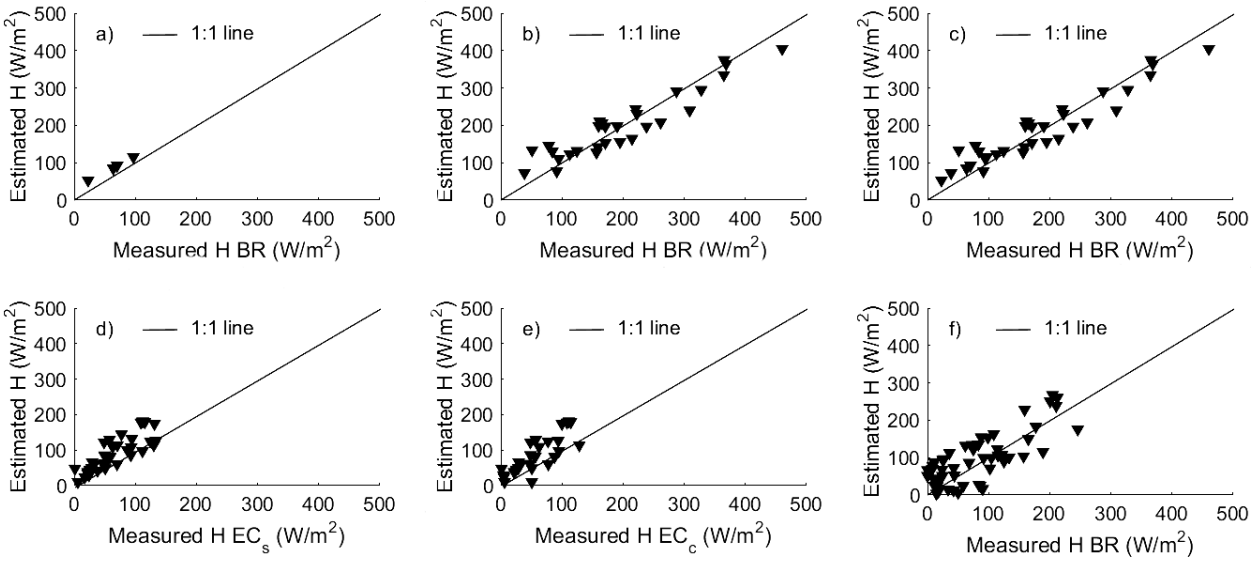


**Figure 4.20:** Measured H vs. Estimated H for deficit and fully irrigated fields at LIRF in 2017 and 2018 regarding the linear $T_o$ models based on LAI range for BR and EC measured sensible heat flux. Graphs 4.20(a), 4.20(b), and 4.20(c) represent, respectively, Measured H vs. Estimated H for deficit irrigated field in 2017, 2018, and 2017-2018 combined data regarding Bowen ratio measured H. Graphs 4.20(d) and 4.20(e) indicate Measured H vs. Estimated H for fully irrigated field in 2017 regarding EC measurements. Graph 4.20(f) shows the model comparison for fully irrigated field in 2018 regarding Bowen ratio measured sensible heat flux at LIRF.

### 4.4.3 Sensible Heat Model Assessment Using General Non-Linear $T_o$ Model at LIRF

Tables 4.41 and 4.42 show, respectively, the statistical analysis of the H model quality assessment based on the general non-linear $T_o$ model for the deficit and fully irrigated fields. Figures 4.21 and 4.22 represent, respectively, the plots of Estimated H vs. Measured H for the given model approach for both treatment fields regarding LAS and BR measured H methods.

Modeling sensible heat flux using the general non-linear $T_o$ model seems to be less effective to provide better results than when the linear model types were tested. There is a strong statistical underestimation of H for the deficit irrigated treatment for LAS and Bowen ratio data set. The RMSE and refined index of agreement were, respectively, higher and lower than the statistical analysis of sensible heat flux modeling based on the linear aerodynamic temperature model types.

For the fully irrigated treatment field, there is a trend of overestimation of estimated H for all measurement methods. The uncertainties around the estimated H based on equation 4.2 model is 0.75 $W/m^2 \pm$ 71.5 $W/m^2$.

The graphical visualization of the results indicate larger variability on the comparison between estimated and measured sensible heat flux. The fact that the points seem to drift apart from the 1:1 line is a good indicator that the non-linear approach may not be addressing an adequate estimation of $T_o$, and affecting the accuracy of modeling sensible heat flux.

**Table 4.41:** Model quality assessment of sensible heat flux for deficit irrigated field at LIRF regarding general non-linear $T_o$ model (equation 4.2).

| Measured H | Year | n | MBE | RMSE | Pearson's R | $d_r$ |
|---|---|---|---|---|---|---|
| [-] | [-] | [-] | $[W/m^2]$ | $[W/m^2]$ | [-] | [-] |
| LAS | 2017 | 7 | -36.2 | 107.0 | 0.93 | 0.68 |
| | 2018 | 55 | -37.5 | 65.7 | 0.80 | 0.59 |
| | 2017-2018 | 62 | -37.4 | 71.5 | 0.79 | 0.62 |
| BR | 2017 | 4 | -27.0 | 30.2 | 0.88 | 0.48 |
| | 2018 | 29 | -31.2 | 83.2 | 0.75 | 0.62 |
| | 2017-2018 | 33 | -31.6 | 85.9 | 0.75 | 0.64 |

**Table 4.42:** Model quality assessment of sensible heat flux for fully irrigated field at LIRF regarding general non-linear $T_o$ model (equation 4.2).

| Measured H | Year | n | MBE | RMSE | Pearson's R | $d_r$ |
|---|---|---|---|---|---|---|
| [-] | [-] | [-] | $[W/m^2]$ | $[W/m^2]$ | [-] | [-] |
| LAS | 2017 | 41 | 43.9 | 78.3 | 0.08 | -0.04 |
| | 2018 | 79 | 8.2 | 43.9 | 0.80 | 0.71 |
| | 2017-2018 | 120 | 20.4 | 58.0 | 0.63 | 0.59 |
| $EC_s$ | 2017 | 35 | 48.6 | 79.5 | 0.02 | 0.05 |
| $EC_c$ | 2017 | 27 | 64.6 | 92.8 | -0.07 | -0.22 |
| BR | 2018 | 52 | 43.9 | 63.7 | 0.72 | 0.51 |

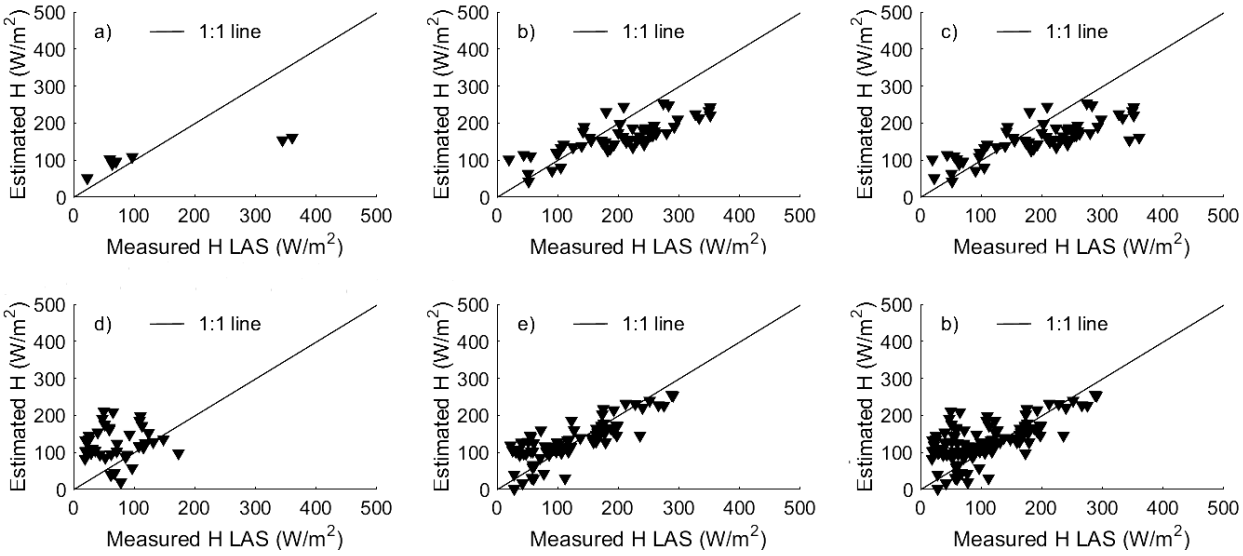


**Figure 4.21:** Measured H vs. Estimated H for deficit and fully irrigated fields at LIRF in 2017 and 2018 based on the general linear $T_o$ model regarding LAS measured sensible heat flux. Graphs 4.21(a), 4.21(b), and 4.21(c) represent, respectively, the Measured LAS H vs. Estimated H for deficit irrigated field in 2017, 2018, and 2017-2018 combined data. Graphs 4.21(d), 4.21(e), and 4.21(f) represent, respectively, the Measured LAS H vs. Estimated H for fully irrigated field in 2017, 2018, and 2017-2018 combined data at LIRF.

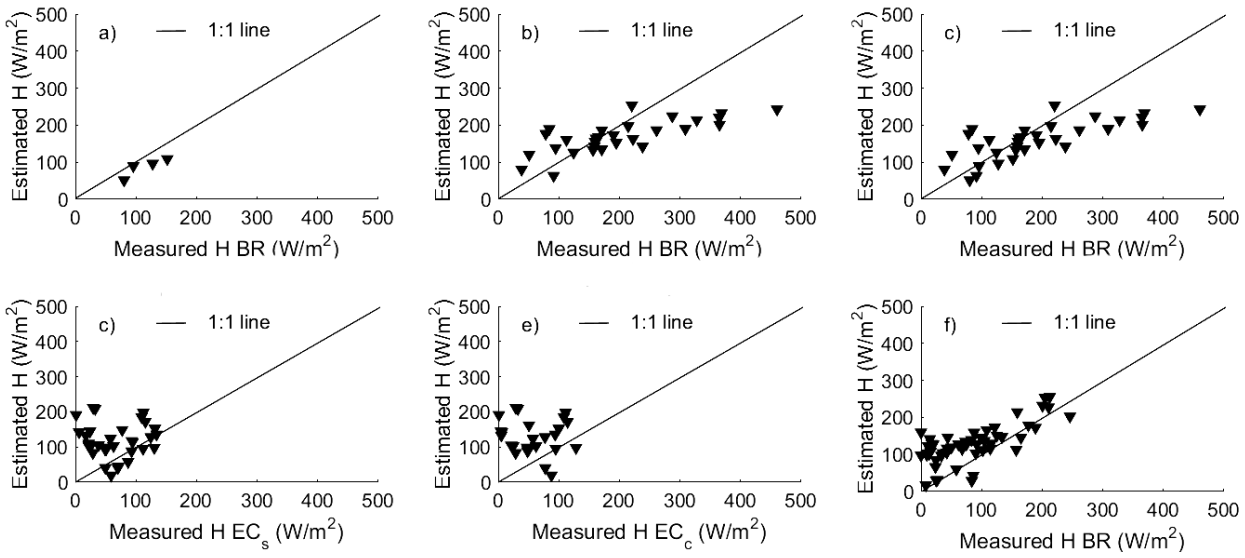


**Figure 4.22:** Measured H vs. Estimated H for deficit and fully irrigated fields at LIRF in 2017 and 2018 based on the general linear $T_o$ model regarding BR and EC measured sensible heat flux. Graphs 4.22(a), 4.22(b), and 4.22(c) represent, respectively, Measured H vs. Estimated H for deficit irrigated field in 2017, 2018, and 2017-2018 combined data regarding Bowen ratio measured H. Graphs 4.22(d) and 4.22(e) indicate Measured H vs. Estimated H for fully irrigated field in 2017 regarding EC measurements. Graph 4.22(f) shows the model comparison for fully irrigated field in 2018 regarding Bowen ratio measured sensible heat flux at LIRF.

### 4.4.4 Sensible Heat Model Assessment Using Non-Linear $T_o$ Models based on LAI range at LIRF

Tables 4.43 and 4.44 show, respectively, the statistical analysis of the H model quality assessment based on the non-linear $T_o$ models for the deficit and fully irrigated fields. Figures 4.23 and 4.24 represent, respectively, the plots of Estimated H vs. Measured H for the given model approach for both treatment fields regarding LAS and BR measured H methods.

The non-linear $T_o$ models based on LAI range seem to perform better than the general non-linear approach for the deficit irrigated field, but it is less accurate than the when the linear approach based on LAI range was applied. The approach of having different models based on the biomass development of the canopy seems to benefit the estimation of sensible heat on the deficit irrigated water management practice for both non-linear and linear model types. 2018 data results

are in better agreement with the measured data than in the year of 2017. The uncertainties around the estimated H based on equation 4.4 model is 0.75 $W/m^2 \pm 53.7\ W/m^2$.

**Table 4.43:** Model quality assessment of sensible heat flux for deficit irrigated field at LIRF regarding non-linear $T_o$ models based on LAI range (equation 4.4).

| Measured H | Year | n | MBE | RMSE | Pearson's R | $d_r$ |
|---|---|---|---|---|---|---|
| [-] | [-] | [-] | $[W/m^2]$ | $[W/m^2]$ | [-] | [-] |
| LAS | 2017 | 7 | -8.2 | 59.4 | 0.99 | 0.79 |
| | 2018 | 55 | -18.6 | 52.9 | 0.82 | 0.71 |
| | 2017-2018 | 62 | -17.4 | 53.7 | 0.83 | 0.74 |
| BR | 2017 | 4 | -26.7 | 28.5 | 0.94 | 0.48 |
| | 2018 | 29 | -0.2 | 44.0 | 0.91 | 0.79 |
| | 2017-2018 | 33 | 3.8 | 43.2 | 0.92 | 0.80 |

**Table 4.44:** Model quality assessment of sensible heat flux for fully irrigated field at LIRF regarding non-linear $T_o$ models based on LAI range (equation 4.4).

| Measured H | Year | n | MBE | RMSE | Pearson's R | $d_r$ |
|---|---|---|---|---|---|---|
| [-] | [-] | [-] | $[W/m^2]$ | $[W/m^2]$ | [-] | [-] |
| LAS | 2017 | 41 | 45.2 | 67.7 | 0.22 | 0.12 |
| | 2018 | 79 | -2.1 | 43.4 | 0.80 | 0.70 |
| | 2017-2018 | 120 | 14.1 | 53.0 | 0.65 | 0.61 |
| $EC_s$ | 2017 | 35 | 48.8 | 71.7 | 0.12 | 0.16 |
| $EC_c$ | 2017 | 27 | 62.7 | 83.1 | 0.07 | 0.12 |
| BR | 2018 | 52 | 34.5 | 57.7 | 0.70 | 0.56 |

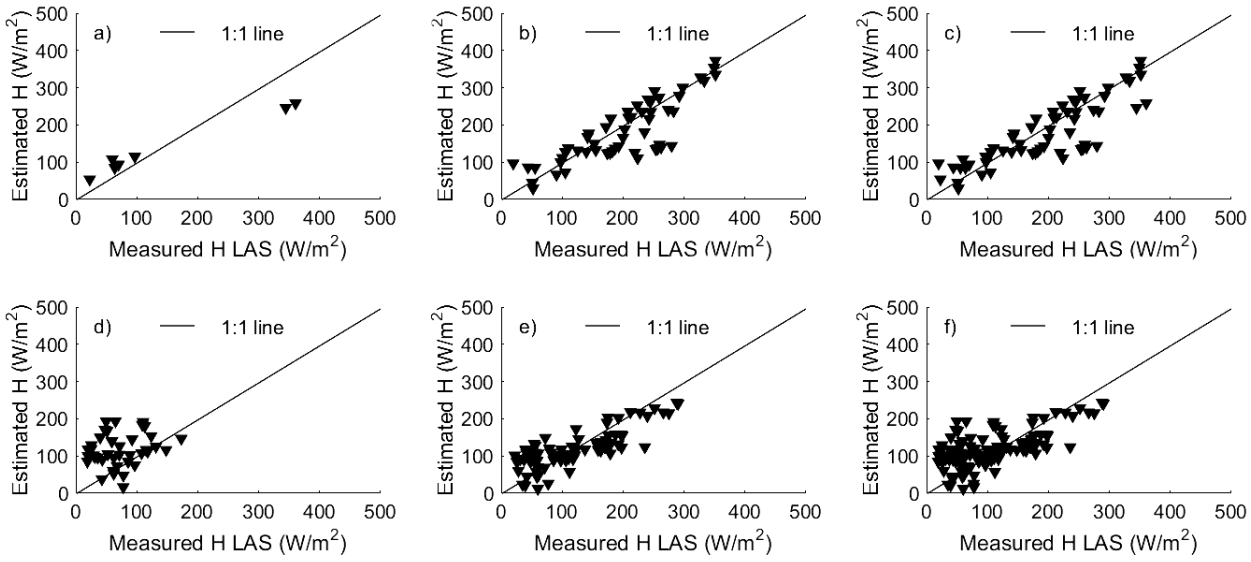


**Figure 4.23:** Measured H vs. Estimated H for deficit and fully irrigated fields at LIRF in 2017 and 2018 regarding the non-linear $T_o$ models based on LAI range for LAS measured sensible heat flux. Graphs 4.23(a), 4.23(b), and 4.23(c) represent, respectively, the Measured LAS H vs. Estimated H for deficit irrigated field in 2017, 2018, and 2017-2018 combined data. Graphs 4.23(d), 4.23(e), and 4.23(f) represent, respectively, the Measured LAS H vs. Estimated H for fully irrigated field in 2017, 2018, and 2017-2018 combined data at LIRF.

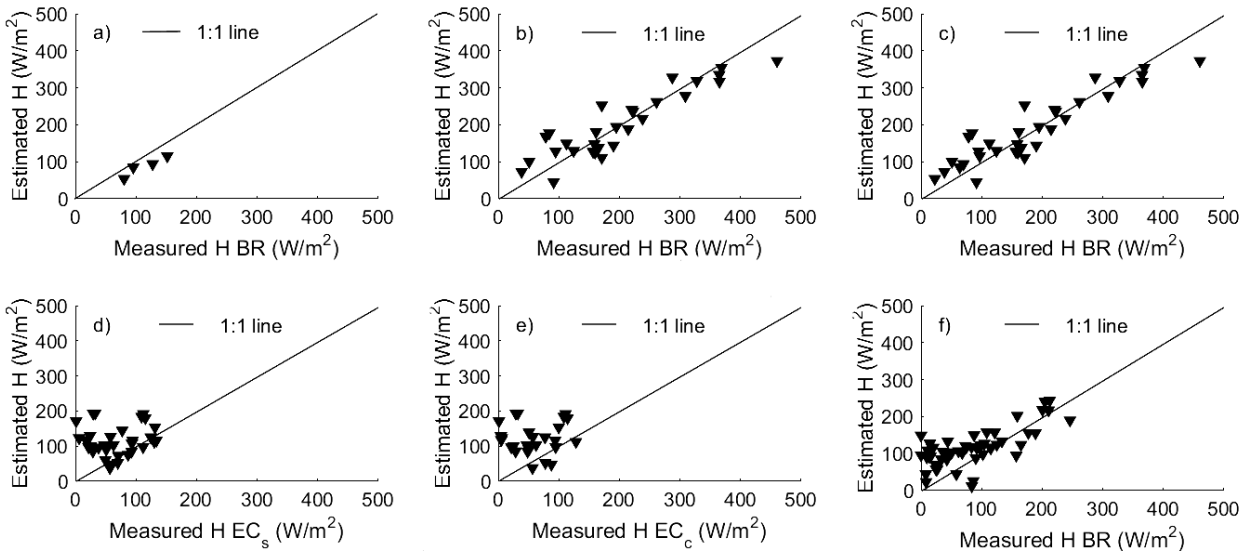


**Figure 4.24:** Measured H vs. Estimated H for deficit and fully irrigated fields at LIRF in 2017 and 2018 regarding the non-linear $T_o$ models based on LAI range for BR and EC measured sensible heat flux. Graphs 4.24(a), 4.24(b), and 4.24(c) represent, respectively, Measured H vs. Estimated H for deficit irrigated field in 2017, 2018, and 2017-2018 combined data regarding Bowen ratio measured H. Graphs 4.24(d) and 4.24(e) indicate Measured H vs. Estimated H for fully irrigated field in 2017 regarding EC measurements. Graph 4.24(f) shows the model comparison for fully irrigated field in 2018 regarding Bowen ratio measured sensible heat flux at LIRF.

### 4.4.5 H Model Quality Assessment Regarding SMEX02 Iowa Data

Tables 4.45 and 4.46 show, respectively, the statistical analysis of sensible heat flux model quality assessment for energy balance closure and non-closure conditions, among the proposed models for $T_o$.

Figures 4.25 and 4.26 show, respectively, the plots of Measured H vs. Estimated H for the evaluation of the developed $T_o$ models for energy balance non-closure and closure conditions.

The sensible heat model based on the linear $T_o$ models for a given LAI range has the best performance among all models proposed, with a RMSE of 17.8 $W/m^2$ and refined index of agreement of 0.54. The root mean square error value is smaller than the ones obtained when analyzing the LIRF data. That is subject to the differences in magnitude of measured and estimated sensible heat

flux at Iowa, as it might be evident on figures 4.25 and 4.26. The sensible heat flux measured at Iowa during daytime and unstable atmospheric conditions range from 0 $W/m^2$ to 100 $W/m^2$. The differences in climate between in Colorado and Iowa support those measured values. As a more humid area, the weather conditions in Iowa offer more local water availability in the soil-plant-atmosphere continuum to be converted to water vapor. That means the amount of energy to break the water molecules bondage to allow vapor to be exchange with the atmosphere is larger due to the an overall more humid area. Thus, the magnitude of sensible heat flux is expected to the smaller than a drier area like Colorado.

The fact that the sensible heat flux model based on the general linear $T_o$ model performed worse than the model regarding the group of $T_o$ models based on LAI range of values seems to agree with the fact that some of the fields at the SMEX02 experiment and used on the analysis were allowed to undergo water stress conditions. The family of linear $T_o$ models based on LAI range was proven to have better performance under the conditions of water stressed fields, which it seems to clearly be direct related to the performance of sensible heat flux modeling as well.

The sensible heat flux models based on the non-linear $T_o$ model types do not have relevant performance using the data from Iowa by having large RMSE and model overestimation of H. That is expected based on the fact that the statistical analysis of the referred $T_o$ models indicated RMSE greater than 2 °C and absolute MBE value above 1 °C. That is also an indication that the modeling of surface aerodynamic temperature has an impact on providing bias on the estimation of sensible heat flux.

When surface energy balance closure conditions were applied, the sensible heat flux model based on the linear $T_o$ model types had a slight increase in performance, which it is evident based on a larger $d_r$ values when compared to the index of agreement from the conditions of non-closure. That could be explained by the fact that the closure method aims to reallocate the residual amount

of flux density that is not captured by the EC measurement system into sensible and latent heat fluxes. However, the RMSE values are similar to the condition of non-closure.

**Table 4.45:** Model quality assessment of sensible heat flux model under energy balance non-closure conditions using SMEX02 IOWA data.

| $T_o$ Model | n | MBE | RMSE | Pearson's R | $d_r$ |
|---|---|---|---|---|---|
| [-] | [-] | $[W/m^2]$ | $[W/m^2]$ | [-] | [-] |
| Linear $T_o$ models for given LAI range | 70 | 1.5 | 17.8 | 0.63 | 0.54 |
| General linear $T_o$ model | 70 | 12.1 | 22.3 | 0.64 | 0.47 |
| Non-linear $T_o$ models for given LAI range | 70 | 77.5 | 103.7 | -0.43 | -0.62 |
| General non-linear $T_o$ model | 70 | 93.7 | 115.4 | -0.41 | -0.67 |

**Table 4.46:** Model quality assessment of sensible heat flux model under energy balance closure conditions using SMEX02 IOWA data.

| $T_o$ Model | n | MBE | RMSE | Pearson's R | $d_r$ |
|---|---|---|---|---|---|
| [-] | [-] | $[W/m^2]$ | $[W/m^2]$ | [-] | [-] |
| Linear $T_o$ models for given LAI range | 72 | 1.1 | 19.0 | 0.65 | 0.58 |
| General linear $T_o$ model | 72 | 9.65 | 21.5 | 0.64 | 0.54 |
| Non-linear $T_o$ models for given LAI range | 72 | 70.0 | 97.6 | -0.40 | -0.51 |
| General non-linear $T_o$ model | 72 | -78.7 | 105.2 | -0.54 | -0.35 |

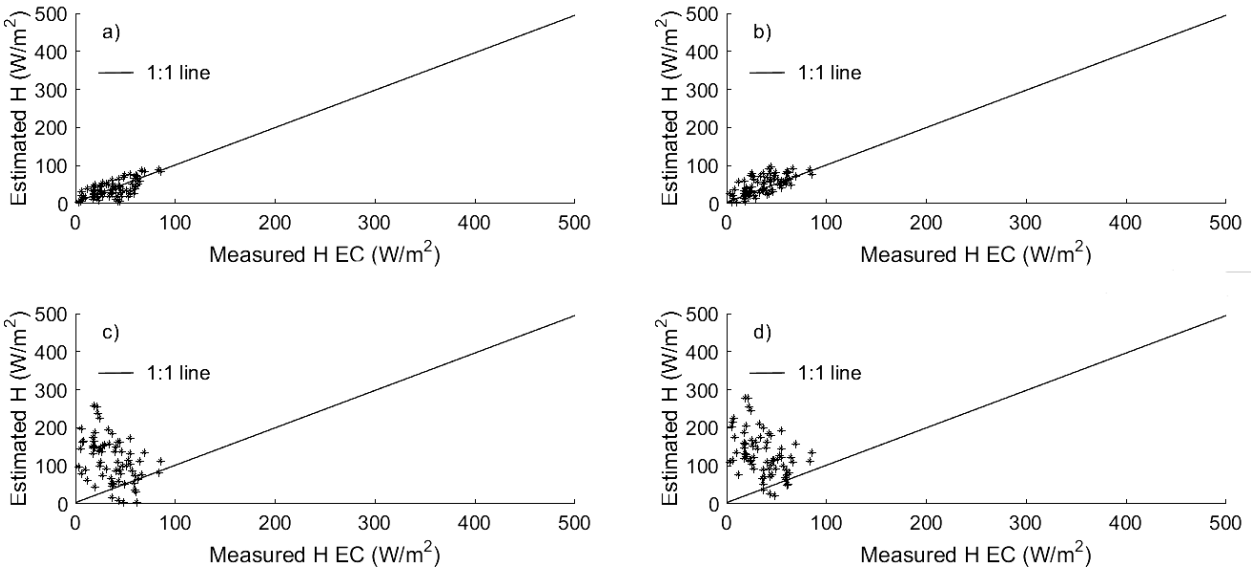


**Figure 4.25:** Measured H vs. Estimated H for SMEX02 IOWA data set under surface energy balance non-closure conditions. Graphs 4.25(a) and 4.25(b) show sensible heat flux plots regarding, respectively, the linear $T_o$ models for a given LAI range and general linear $T_o$ model. Graphs 4.25(c) and 4.25(d) show H plots regarding, respectively, the non-linear $T_o$ models for a given LAI range and general non-linear $T_o$ model. All graphs are for surface energy balance non-closure conditions.

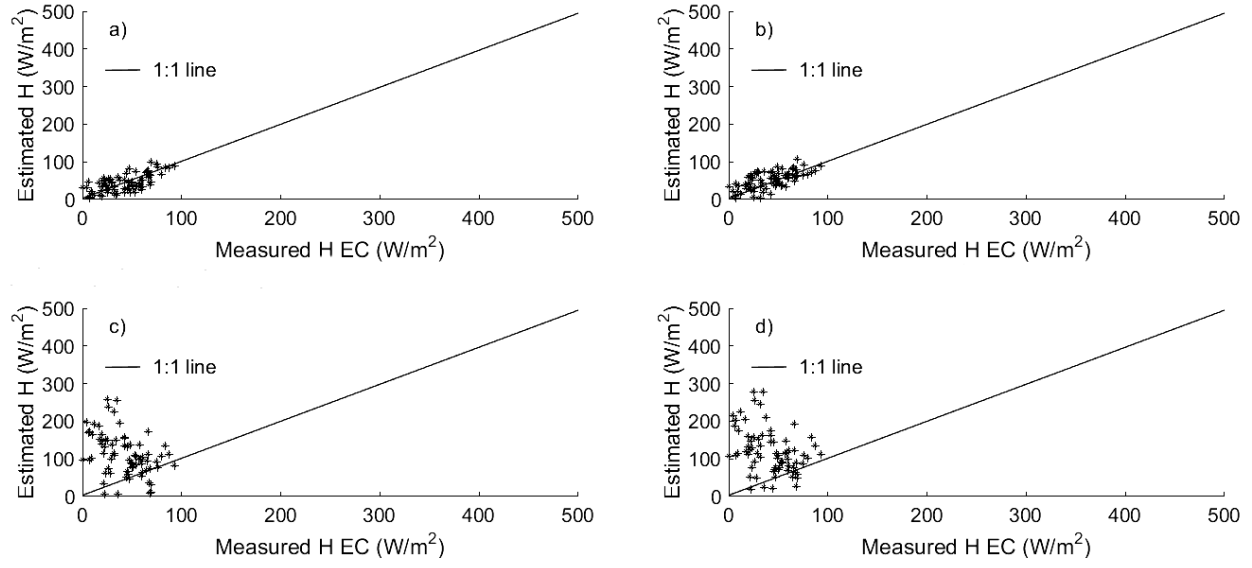


**Figure 4.26:** Measured H vs. Estimated H for SMEX02 IOWA data set under surface energy balance closure conditions. Graphs 4.26(a) and 4.26(b) show sensible heat flux plots regarding, respectively, the linear $T_o$ models for a given LAI range and general linear $T_o$ model. Graphs 4.26(c) and 4.26(d) show H plots regarding, respectively, the non-linear $T_o$ models for a given LAI range and general non-linear $T_o$ model. All graphs are for surface energy balance closure conditions.

### 4.4.6 H Model Quality Assessment Regarding CSU AVRC Data

Table 4.47 shows the statistical analysis of sensible heat flux model quality assessment for the proposed models for $T_o$. Figure 4.27 shows the plots of Measured H vs. Estimated H for the evaluation of the proposed $T_o$ models.

The sensible heat model based on the general linear $T_o$ model performed better than all other models by having a RMSE of 31.8 $W/m^2$ and $d_r$ of 0.60. Both H models based on linear $T_o$ model types provided overestimation of sensible heat flux while underestimation of H was identified when non-linear aerodynamic temperature model types were applied to calculate sensible heat flux. The limited data for evaluating H is due to the uncertainties introduced on the measured soil heat flux estimation. Once again, the linear $T_o$ models have proven to be a better alternative to estimate sensible heat flux with more accurate results than the non-linear approaches. The RMSE magnitude seems to be similar to the ones at LIRF. That is expected based on the fact that both Rocky Ford and Greeley have similar climate conditions, which makes the models to have errors of the same magnitude. However, the refined index of agreement of the sensible heat analysis at CSU ARVC is lower than the $d_r$ values for the model at LIRF. That is overall due to the fact that the models were developed based on LIRF data and running the empirical models and comparing with the measurements that originated the equations will provide higher agreements than the scenario in which data set from different locations are used to evaluate model's performance.

**Table 4.47:** Model quality assessment of sensible heat model using CSU ARVC data.

| $T_o$ Model | n | MBE | RMSE | Pearson's R | $d_r$ |
|---|---|---|---|---|---|
| [-] | [-] | $[W/m^2]$ | $[W/m^2]$ | [-] | [-] |
| Linear $T_o$ models for given LAI range | 13 | 9.5 | 41.8 | 0.41 | 0.46 |
| General linear $T_o$ model | 13 | 6.3 | 31.8 | 0.62 | 0.60 |
| Non-linear $T_o$ models for given LAI range | 13 | -5.9 | 62.1 | -0.14 | 0.36 |
| General non-linear $T_o$ model | 13 | -2.8 | 61.2 | 0.08 | 0.31 |

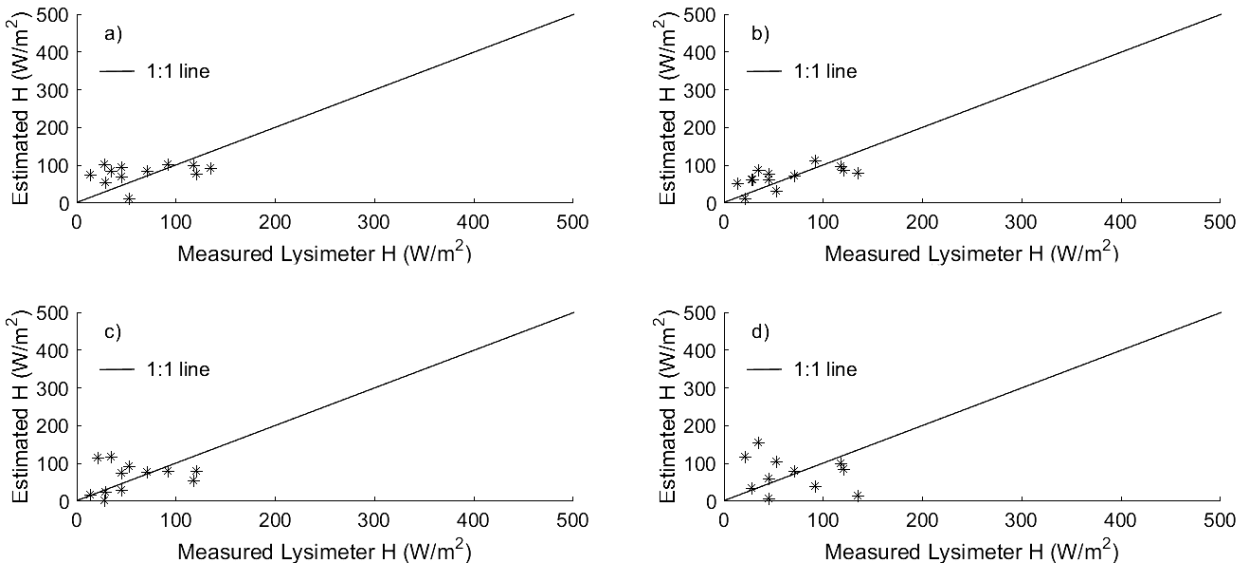


**Figure 4.27:** Measured H vs. Estimated H plots for CSU ARVC data set. Graphs 4.27(a) and 4.27(b) show sensible heat flux plots regarding, respectively, the linear $T_o$ models for a given LAI range and general linear $T_o$ model. Graphs 4.27(c) and 4.27(d) show H plots regarding, respectively, the non-linear $T_o$ models for a given LAI range and general non-linear $T_o$ model.

## 4.5 Aerodynamic Resistance Model Results

Tables 4.48 and 4.49 show, respectively, the statistical analysis of the aerodynamic resistance model quality assessment regarding the canopy roughness elements model based on remote sensing data and the standard approaches as a function of crop height for deficit and fully irrigated fields at LIRF. Figure 4.28 shows the plots of LAS $r_{ah}$ vs. Estimated $r_{ah}$ for the evaluation of the performance of remote sensing based roughness elements models.

The remote sensing approaches to estimate zero-displacement height and roughness length for momentum have different performances depending of the water management practice chosen. When combined data from 2017 and 2018 are analyzed, the deficit irrigated field has better agreement between estimated aerodynamic resistance based on remote sensing and LAS $r_{ah}$ than the fully irrigated field. That is evident based on $d_r$ value for the deficit irrigated data being larger than for the field without water stress conditions ($0.76 > 0.68$).

When comparing the remote sensing approaches to the one based on only crop height, there is not much difference in $r_{ah}$ model performance between the two methods under water stressed conditions as the RMSE are, respectively, 4.4 and 4.6 s/m. However, when the fully irrigated field data is assessed, the results indicate that there is an advancement when applying the approaches developed by Choudhury and Monteith (1988) based on LAI for calculating the canopy roughness length and, consequently, the aerodynamic resistance.

**Table 4.48:** Model quality assessment of aerodynamic resistance using LIRF data for deficit irrigated field.

| Roughness element's Model | Category | Year | n | MBE | RMSE | Pearson's R | $d_r$ |
|---|---|---|---|---|---|---|---|
| [-] | [-] | [-] | [-] | [s/m] | [s/m] | [-] | [-] |
| Choudhury and Monteith (1988) | Remote sensing LAI based models | 2017 | 7 | -7.1 | 7.5 | 0.97 | 0.53 |
| | | 2018 | 55 | 2.1 | 3.8 | 0.90 | 0.74 |
| | | 2017-2018 | 62 | 1.0 | 4.4 | 0.83 | 0.76 |
| Brutsaert (1982) | Non-remote sensing based models | 2017 | 7 | -10.0 | 10.9 | 0.88 | 0.33 |
| | | 2018 | 55 | 0.4 | 3.0 | 0.88 | 0.81 |
| | | 2017-2018 | 62 | -0.8 | 4.6 | 0.80 | 0.78 |

**Table 4.49:** Model quality assessment of aerodynamic resistance using LIRF data for fully irrigated field.

| Roughness element's Model | Category | Year | n | MBE | RMSE | Pearson's R | $d_r$ |
|---|---|---|---|---|---|---|---|
| [-] | [-] | [-] | [-] | [s/m] | [s/m] | [-] | [-] |
| Choudhury and Monteith (1988) | Remote sensing LAI based models | 2017 | 41 | -5.0 | 5.4 | 0.98 | 0.62 |
| | | 2018 | 79 | 1.7 | 2.8 | 0.92 | 0.69 |
| | | 2017-2018 | 120 | -0.6 | 3.9 | 0.79 | 0.68 |
| Brutsaert (1982) | Non-remote sensing based models | 2017 | 41 | -9.0 | 9.5 | 0.96 | 0.30 |
| | | 2018 | 79 | -1.6 | 2.8 | 0.87 | 0.64 |
| | | 2017-2018 | 120 | -4.1 | 6.0 | 0.71 | 0.51 |

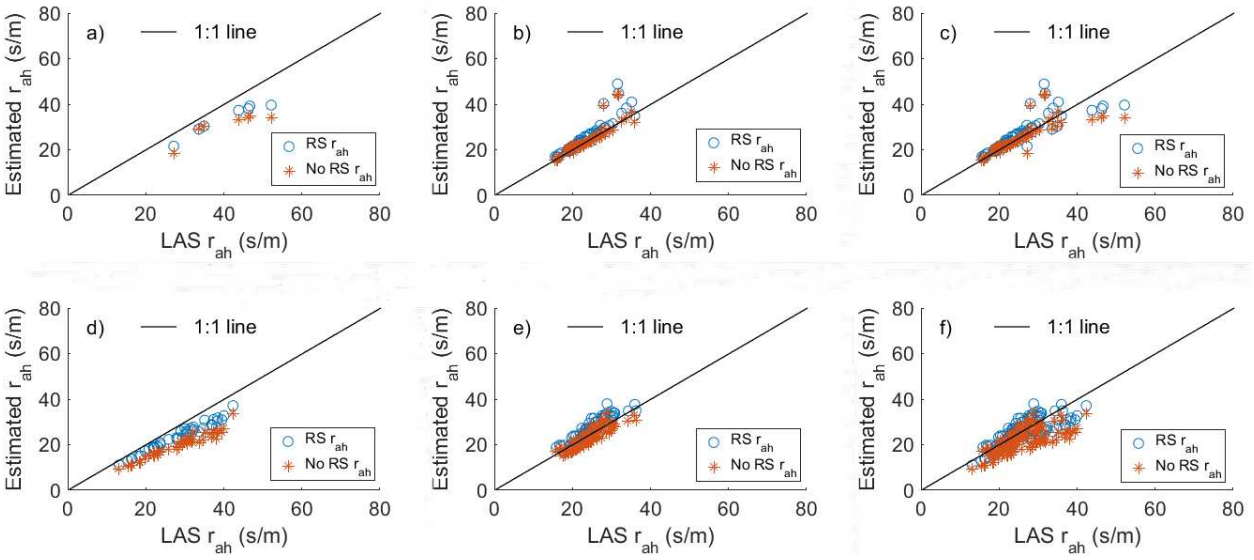


**Figure 4.28:** LAS $r_{ah}$ vs. Estimated $r_{ah}$ plots for LIRF data set. Graphs 4.28(a), 4.28(b), and 4.28(c) show aerodynamic resistance plots regarding, respectively, the years of 2017, 2018, and 2017-2018 combined data for the deficit irrigated field at LIRF. Graphs 4.28(d), 4.28(e), and 4.28(f) show aerodynamic resistance plots regarding, respectively, the years of 2017, 2018, and 2017-2018 combined data for the fully irrigated field at LIRF.

# Chapter 5

# Conclusions and Discussion

The introduction of fractional percent cover and the wind speed direction variables into the aerodynamic temperature model indicates a further step into improving the estimations of sensible heat flux for corn. The linear model types developed have provided less error than the proposed non-linear $T_o$ model types and the proposed models that were subject to evaluation. The general linear model for $T_o$ has performed better under fully irrigated conditions, while the linear $T_o$ models based on LAI range have provided better model agreement under a water stress scenario. That validates the improved $T_o$ modeling perspective to account for different canopy biomass conditions to assess better models to represent the surface when the healthiness of the crop suffers external environmental factors that cause changes on the development of the vegetation.

The analysis regarding the crop layout on the field and its influence on the accuracy of the model has indicated that when the wind is near parallel trajectory to the crop row above the surface, the models have better performance. Corroboration with one of the research hypothesis that the layout of the rows influence the modeling for $T_o$, regardless of the model type developed.

The sensible heat modeling based on the proposed aerodynamic surface temperature have indicated better agreement under the linear approach than the non-linear model type. The sensible heat measurements provided reliable information to assess the performance of the modeling of H, being the Bowen ratio and the eddy covariance methods the ones that were statistically similar in magnitude in regards to the LAS measurements.

The linear proposed models for $T_o$ seemed to enhance the modeling for H since the magnitude of improvement in comparison to the published models evaluated, on average, were 33 $\%$ for the deficit irrigated field and 28 $\%$ for the fully irrigated field in 2018 at LIRF, respectively. The pub-

lished models were developed under different water management practices and climate conditions, which might have an effect on the published models results for H. When it comes on improvements on ET estimation based on the the surface energy balance approach, the linear proposed models for $T_o$ seemed to enhance the modeling for ET since the magnitude of improvement, on average were, respectively, 45.5 $\%$ for the deficit irrigated field and 31.3 $\%$ for the fully irrigated field in 2018 at LIRF.

The introduction of remote sensing based approaches to estimate the roughness canopy elements has been proven to perform slightly better than the overall approach as a function of only crop height when no water stress conditions are predominant.

Future directions and recommendations would lean towards the development of a physical model for $T_o$ that may provide non-empirical insight on the occurrence of the aerodynamic height within the canopy to adequately assess the model and improve the estimation of sensible heat flux. Empirical models such as those developed are subject of posterior calibration for different vegetated surface types and climate conditions and demand data and resources that are not always available. The future advancements towards understanding the occurrence of the aerodynamic height and the dynamics of heat and momentum transfer within the soil-plant-atmosphere continuum are an extra attempt to develop a model that might overcome the limitations of empirical models to have similar performance under different crop types and climate conditions.

# Bibliography

Allen, R.G., Tasumi, M., and Morse, A. (2005). Satellite-based evapotranspiration by METRIC and Landsat for western states water management. Presented at the US Bureau of Reclamation Evapotranspiration Workshop, Ft. Collins, CO, USA, 8-10.

Amatya, D.M., Irmak, S., Gowda, P., Sun, G., Nettles, J.E., and Douglas-Mankin, K.R. (2016). Ecosystem evapotranspiration: Challenges in measurements, estimates, and modeling. Transactions of the ASABE 59, no. 2: 555-60.

Arya, S.P. (2001). Introduction to micrometeorology. San Diego: Academic Press.

ASCE-EWRI, 2005. The ASCE Standardized Reference Evapotranspiration Equation. Report 0-7844-0805-X, ASCE Task Committee on Standardization of Reference Evapotranspiration. Reston, Va., American Soc. Civil Engineers.

Bastiaanssen, W.G.M., Menenti, M., Feddes, R.A., and Holtslag, A.A.M. (1998). A remote sensing surface energy balance algorithm for land (SEBAL). 1. Formulation. Journal of Hydrology 212-213: 198-212.

Boulet, G., Olioso, A., Ceschia, E., Marloie, O., Coudert, B., Rivalland, V., Chirouze, J., and Chehbouni, G. (2012). An empirical expression to relate aerodynamic and surface temperatures for use within single-source energy balance models. Agricultural and Forest Meteorology 161: 148-55.

Brutsaert, W. (1982). Evaporation into the Atmosphere. D. Reidel Publication, 299 pp.

Buttar, N.A., Yongguang, H., Shabbir, A., Lakhiar, I. A., Ullah, I., Ali, A., Aleem, M., and Yasin, M.A. (2018). Estimation of evapotranspiration using Bowen ratio method. IFAC PapersOnLine, 51-17, 807-810.

Campbell G.S. and Norman J.M. (1998). Wind. In: An Introduction to Environmental Biophysics. Springer, New York, NY. 306 pp.

Carrasco-Benevides, M., Ortega-Farias, S., Morales-Salinas, L., Poblete-Echeverria, C., and Chavez, J. L. (2017). Calibration and validation of an aerodynamic method to estimate the spatial variability of sensible and latent heat fluxes over a drip-irrigated Merlot vineyard. International Journal of Remote Sensing 38, no. 24: 7473-496.

Chavez, J. L., Neale, C.M.U., Hipps, L.E., Prueger, J.H., and Kustas, W.P. (2005). Comparing aircraft-based remotely sensed energy balance fluxes with eddy covariance tower data using heat flux source area functions. Journal of Hydrometeorology 6, no. 6: 923-40.

Chavez, J.L., Gowda, P.H., and Howell, T.A. (2009). Modeling surface aerodynamic temperature in a semi-arid advective environment. Reno, Nevada, June 21 - June 24.

Chavez, J.L. and Lopez-Urrea, R. (2009). One-step approach for estimating maize actual water use: Part I. Modeling a variable surface resistance. Irrigation Science.

Chai, T. and Draxler, R.R. (2014). Root mean square error (RMSE) or mean absolute error (MAE)? Arguments against avoiding RMSE in the literature. Geosci. Model Dev., 7, 1247-1250.

Chehbouni, A., Lo Seen, D., Lhomme, J.P., Monteny, B.M., and Kerr, Y.H. (1995). Relationship between Radiative and Aerodynamic surface temperature over sparsely vegetated surfaces:

Estimation of sensible heat flux. Geoscience and Remote Sensing Symposium, 739-41.

Chehbouni, A., Lo Seen, D., Njoku, E.G., and Monteny, B.M. (1996). Examination of the difference between radiative and aerodynamic surface temperatures over sparsely vegetated surfaces. Remote Sensing of Environment 58, no. 2: 177-86.

Choudhury, B.J., Reginato, R.J., and Idso, S.B. (1986). An analysis of infrared temperature observations over wheat and calculation of latent heat flux. Agricultural and Forest Meteorology 37, no. 1: 75-88.

Colaizzi, P.D., Evett, S.R., and Howell, T.A. (2004). Comparison of aerodynamic and radiometric surface temperature using precision weighing lysimeters. Remote Sensing and Modeling of Ecosystems for Sustainability 55.

Comunian, L., Giudici, M., Landoni, L., and Pugnaghi, S. (2018). Improving Bowen-ratio estimates of evaporation using a rejection criterion and multiple-point statistics. Journal of Hydrology 563, 43-50.

De Bruin, H.A.R., Kohsiek, W., and Van den Hurk, B.J.J.M. (1993). A verification of some methods to determine the fluxes of momentum, sensible heat and water vapour using standard deviation and structure parameter of scalar meteorological quantities. Boundary-Layer Meteorol. 63, 231-257.

Dunn, O.J. (1964). Multiple comparisons using rank sums. Technometrics. 6, 241-252.

Garcia, L.A., Elhaddad, A., Altenhofen, J., Hattendorf, M. (2013). Developing corn regional crop coefficients using a satellite-based energy balance model (ReSET-RASTER) in the south platte river basin of Colorado. Journal of Irrigation and Drainage Engineering. 139, no. 10: 821-832.

Gowda, P.H., Chavez, J.L., Colaizzi, P.D., Evett, S.R., Howell, T. A., and Tolk, J. A. (2007). Remote sensing based energy balance algorithm for mapping ET: Current status and future challenges. Transactions of the ASABE 59, no. 5, 1639-644.

Grigg, N. Natural water systems. Chap. 7 in Water manager handbook. Fort Collins: Aquamedia Publishing, 2005.

Hanks, R.J. and Ashcroft, G.L. (1980). Applied soil physics: Soil water and temperature application. Spring-Verlarg, 159 pp.

Hoekstra, A.Y. and Chapagain, A.K. (2006). Water footprints of nations: Water use by people as a function of their consumption pattern. Water Resources Management 21, no. 1: 35-48.

Johnson, L.F. and Trout, T.J. (2012). Satellite NDVI assisted monitoring of vegetable crop evapotranspiration in California's San Joaquin Valley. Remote Sensing 4, no. 2: 439-55.

Kaimal J. C. and Finnigan, J. J. (1994). Atmospheric boundary layer flows. New York: Oxford University Press, 289 p.

Kruskal, W.H. and Wallis, A. (1952). Use of ranks in one-criterion variance analysis. Journal of the American Statistical Association. 47, 583-621.

Legates, D.R. and McCabe Jr., G.J. (1999). Evaluating the use of "Goodness-of-Fit" measures in hydrologic and hydroclimatic model validation. Water Resour. Res., 35(1), 233-241

Li, X., Gao, Z., Li, Z., and Tong, B. (2017). Comparison of sensible heat fluxes measured by a large aperture scintillometer and eddy covariance system over a heterogeneous farmland in east China. Atmosphere, 8 no. 101: 1-20.

Liou, Y.A. and Kar, S. (2014). Evapotranspiration estimation with remote sensing and various surface energy balance algorithms- A Review. Energies 7, no. 12: 2821-849.

Maki, T. (1975). Interrelationships between zero-plane displacement, aerodynamic roughness length and plant canopy height. J. Agricultural Meteorology 3 1 :6 1-70. (Japanese text, English summary and figure legends.)

McInnes, K.J., Heilman, J.L., and Lascano, R.J. (1995). Aerodynamic conductances at the soil surface in a vineyard. Agricultural and Forest Meteorology, no. 79: 29-37.

McIntosh, D. H. and Thom, A. S. (1968). Essentials of Meteorology. Wykeham Publications, London, UK, 239 pp.

Menenti, M. and Choudhury, B.J. (1993). Parameterization of land surface evaporation by means of location dependent potential evaporation and surface temperature range. IAHS Publication, no. 212: 561-68.

Monteith, J.L. and Unsworth, M.H. (2007). Principles of Environmental Physics: Plants, Animals, and the Atmosphere. 3rd ed. Amsterdam: Elsevier/Academic Press.

Norman, J.M., Kustas, W.P., and Humes, K.S. (1995). Source approach for estimating soil and vegetation energy fluxes in observations of directional radiometric surface temperature. Agricultural and Forest Meteorology 77, no. 3-4: 263-93.

Ochsner, T. E., Sauer, T. J., and Horton, B. (2006). Field tests of the soil heat flux plate method and some alternatives. Agronomy Journal, no. 98: 1005-1014.

Ott R.L. and Longnecker, M. (2001). Multiple Comparisons. Chap. 9 in an introduction to statistical methods and data analysis. Fort Collins: Thomson Learning Inc.

Perez, P.J., Castellvi, F., Ibanez, M., Rosell, J.I. (1999). Assessment of reliability of Bowen ratio method for partitioning fluxes. Agricultural and Forest Meteorology, 141-150.

Prueger, J.H. and Kustas, W.P. (2005). Aerodynamic methods for estimating turbulent fluxes. Publications from USDAARS / UNL Faculty. 1394.

Roerink, G.J., Su, Z., and Menenti, M. (2000). S-SEBI: A simple remote sensing algorithm to estimate the surface energy balance. Physics and Chemistry of the Earth, Part B: Hydrology, Oceans and Atmosphere 25, no. 2: 147-57.

Rondeaux, G., Steven, M., and Baret, F. (1996). Optimisation of soil-adjusted vegetation indices. Remote Sens. Environ. 55, 95-107.

Rosenberg, N.J., Blaine, L.B., and Verma, S.B. Microclimate: the biological environment. New York: Wiley, 1983.

Schmugge, T.J., Kustas, W.P., Ritchie, J.C., Jackson, T.J., and Rango, A. (2002). Remote sensing in hydrology. Advances in Water Resources 25, no. 8-12: 1367-385.

Schultz, G.A. and Engman, E. Physical principles and technical aspects of remote sensing. Chap. 2 in Remote Sensing in Hydrology and Water Management. Engineering Online Library. Berlin; New York: Springer, 2000.

Shaw, R.H. and Pereira, A.R. (1961). Aerodynamic roughness of a plant canopy: a numerical experiment. Agric. Meteorol. 2651-65.

Sidak, Z. (1967). Rectangular confidence regions for the means of multivariate normal distributions. Journal of the American Statistical Association. 62, 626-633.

Su, Z. (2002). The surface energy balance system (SEBS) for estimation of turbulent heat fluxes. Hydrology and Earth System Sciences 6, no. 1: 85-100.

Tanner C. B. and Thurtell, G. (1969). Anemoclinometer measurements of Reynolds stress and heat transport in the atmospheric surface layer. Research and Development Technical Report to US Army Electronic Command, ECOM 66-G22-F. Department of Soil Sciences, University of Wisconsin, 199 p.

Twine, T. E., Kustas, W. E., Norman, J. M., Cook, D. R., Houser, P. R., Meyers, T. P., Prueger, J. H., Starks, P. J., and Wesely, M. L. (2000). Correcting eddy-covariance flux underestimates over a grassland. Agric. For. Meteor., 103, 229-317.

Tian, X.,Li, Z.Y., van der Tol, C., Su, Z., Li, X., He, Q.S., Bao, Y.F., Chen, E.X., and Li, L.H. (2011). Estimating zero-plane displacement height and aerodynamic roughness length using syn-

thesis of LiDAR and SPOT-5 data. Remote Sensing of the Environment 115, 2330-2341.

Thom, A. S. (1972). Momentum, mass and heat exchange of vegetation. Q.J.R. Meteorol. Soc., 98: 124-134.

Varble, J.L. and Chavez, J.L. (2011). Performance evaluation and calibration of soil water content and potential sensors for agricultural soils in eastern Colorado. Agricultural Water Management 101, 93-106.

Webb E. K., Pearman G. I., and Leuning R. (1980). Correlation of flux measurements for density effects due to heat and water vapour transfer. Quart J Roy Meteorol Soc 106:85-100.

Wang, T.I., Ochs, G.R., and Clifford, S.F. (1978). A saturation-resistant optical scintillometer to measure $C_n^2$, J. Opt. Soc. Am. 69, 334-338.

Wenbin, M., Chen, Z., Sun, L., Gao, W., Luo, X., Yang, T., Pu, J., Huang, G., and Yang, X. (2004). A scheme for pixel-scale aerodynamic surface temperature over hilly land. Advances in Atmospheric Sciences 21, no. 1: 125-31.

Willmott, C.J. (1981). On the validation of models. Physical Geography, 2, 184-194.

Willmott, C.J., Robeson, S. M., and Matsuura, K. (2012), A refined index of model performance. Int. J. Climatol., 32: 2088-2094.

Wyngaard, J.C., Izumi, Y., and Collins Jr., S.A. (1971). Behaviour of the refractive index structure parameter near the ground, J. Opt. Soc. Am. 61, 1646-1650.

Yasuda, N. (1988). Turbulent diffusivity and diurnal variations in the atmospheric boundary layer. Boundary-Layer Meteorology.